

SLOW AND FAST ATOMS:
MODELING STRONG FIELD EFFECTS ON YB FOR SLOWING
AND QUANTUM IMAGING OF MAGNETIC FIELDS

A DISSERTATION
SUBMITTED TO THE DEPARTMENT OF PHYSICS
AND THE COMMITTEE ON GRADUATE STUDIES
OF STANFORD UNIVERSITY
IN PARTIAL FULFILLMENT OF THE REQUIREMENTS
FOR THE DEGREE OF
DOCTOR OF PHILOSOPHY

Tanaporn Na Narong
September 2023

Abstract

Known for the ultra-stable clock transition, ytterbium atoms are one of the leading candidates for atomic clocks and qubits for quantum computing. This thesis tells two untold stories of ytterbium atoms, slow and fast.

The first half of the thesis covers an alternative laser slowing method using only the narrow 1S_0 - 3P_1 cooling transition that utilizes amplitude-modulated light to induce a series of stimulated emissions. This slowing method shows promise as a starting point for many cold-atom experiments. I present a numerical model of this process and how it can help engineer optical forces on ytterbium and other alkaline earth-like atoms.

In the second half, I show how a combination of fast ytterbium atoms and a similar laser setup enables visual imaging of magnetic field gradients and contours. Based on Autler-Townes splitting and the Hanle effect, this unique magnetometer can measure both magnitude and direction of the magnetic fields based on understanding of dark striped patterns in the atomic fluorescence. Both aspects of this thesis bring to light the unique features of the narrow 1S_0 - 3P_1 transition in ytterbium with potential to advance quantum sensing.

Lovingly dedicated to Papa, Mama & P'Ton

Acknowledgements

There is a story I tell any time someone asks me what got me interested in physics. Ajarn Pasong was my science teacher in 9th grade. One day in class he made an offer I could not resist: “if you qualify for the first round of the science olympiad, I’ll give you full marks for my midterm science exam.” I took the bait. I went to tutoring sessions on basic calculus and classical mechanics with high schoolers, and then I spent the next few summers in physics olympiad camps solving problems.

I did not have to study for Ajarn Pasong’s science midterm, but the joke’s on me because I ended up doing a lot more studying than my teenage self could have imagined, a PhD included. Physics took me across the world, one ocean at a time, 8,000 miles away from where I was born. On this long journey, I have found and cherished love, relationships, community, and support from so many people. I proudly and gratefully honor some of them here.

To my family, every move I made away from home could not have been easy for you. Papa, thank you for always reminding me to follow my dreams, for insisting on sending me away to pursue them, for always having my back. For calling me every day in high school. Thank you for believing in me even when I don’t. Mama, thank you for holding us all together and taking care of me even when things are hard. My big brother, P’Ton, your kindness and generosity inspire me. Thank you for being there for me from day one.

To my advisor, Leo, thank you for teaching me how to be a kind scientist and a great mentor. You are my role model who inspires me every day. On good days, you remind me how fun and interesting science can be. On bad days, you remind me that I have your support and everything will be okay. I cannot ask for a better mentor:

one who treats everyone with kindness and respect. There were so many days in grad school that I doubted myself and my science, but not even a single day that I doubted if I had chosen the right advisor. I could not have done this without you.

To my amazing collaborators and labmates: Hongquan, Josh, Brian, Lingfang, Michael, our rotation students, summer undergrads, and everyone I mentored, thank you for sharing this journey with me and making hard days at work easier. I enjoyed working and learning with all of you. I also thank Prof. Jason Hogan and Prof. Monika Schleier-Smith for their support and guidance.

To wonderful friendships that stand the test of distance and time, I am so lucky to have y'all: Best, Prae, Tyson, Kawin, Tarnmay, P'Earth, Mae Noey, Kate (not you, Kate Coppess, keep scrolling). To my cohort and others in the Stanford physics community: Ronen, Connie, Megan, Min, our lunches and conversations have been essential to my happiness and sanity. To my special collaborators, Eric and Cindy, our meetings are the only work meetings worth having on the weekends. I also owe my thanks to fellow women and gender minorities in physics and STEM, inside and outside of my WISE group, for constant guidance, support, and solidarity.

To the Johnson-Cruickshank family, Maria, Jeff, Gran, Tom (and honorable members, Rio, Millie, Miss Ella, and Penny Bean), thank you for welcoming me into your beautiful family and taking care of me. Your love and constant support have got me through these past few years when I rarely had a chance to see my family in Thailand. You are my family.

To my partner, John, finding words to sum up what you mean to me and how much you have done for me is one of the hardest parts of writing this thesis. You have been with me through the highest highs and the lowest lows of grad school, in California, in North Carolina, and in New York. Your support and belief in me have given me strength, courage, and confidence to do it all. I love you so much and I feel much of your love every day.

To my chosen family, Roo's crew: Kate, Claire, and Madam Roo herself, you will always be my home. The most important and valuable thing I have earned in grad school is not this thesis, but the beautiful family and home that we have built together.

Acknowledgements (Research)

I acknowledge financial support from the Office of Naval Research (ONR) and NSF Q-SEnSE: Quantum Systems through Entangled Science and Engineering (NSF QLCI Award OMA-2016244). The stimulated slowing project was funded by the Office of Naval Research grant N000141712255. I would like to thank NSF Q-SEnSE for funding the magnetometer project and supporting valuable research collaboration in quantum science across organizations.

Some of the computing for this thesis was performed on the Sherlock cluster. I would like to thank Stanford University and the Stanford Research Computing Center for providing computational resources and support that contributed to this research.

Contents

Abstract	v
Acknowledgements	ix
Acknowledgements (Research)	xi
1 Introduction, context, and outline	1
1.1 Introduction	1
1.1.1 Slow atoms: stimulated slowing of Yb atoms	1
1.1.2 Fast thermal atoms: Yb atomic magnetometer	3
1.2 Context for the research	5
1.3 Thesis outline	6
2 Laser Cooling and Trapping of Yb	9
2.1 Introduction	9
2.2 Atomic ytterbium	10
2.3 Radiative Scattering Force	11
2.4 Dipole Forces	15
2.4.1 Pulsed light	16
2.4.2 Bichromatic Force (BCF)	17
2.4.3 Adiabatic Rapid Passage (ARP)	20
2.5 Summary	22

3 Stimulated Slowing with Bichromatic Force	23
3.1 Introduction	23
3.2 Numerical model	23
3.2.1 Calculating bichromatic force (BCF)	25
3.2.2 Monte Carlo simulation	28
3.3 Chirped BCF	38
3.4 Broadband cooling	43
4 Stimulated Slowing with Polychromatic Forces	48
4.1 Introduction	48
4.2 Square wave amplitude modulation	49
4.2.1 Numerical model	49
4.2.2 Optimizing the force	53
4.2.3 Optimum square PCF profile	56
4.2.4 Estimating the MOT loading rate	57
4.3 Phase modulation	59
4.4 Conclusion	63
5 Yb Atomic Magnetometer	64
5.1 Introduction	64
5.2 Atomic magnetometers	65
5.2.1 Imaging of magnetic fields	67
5.2.2 Vector magnetometers	69
5.3 Autler-Townes splitting	71
5.4 Hanle effect	74
6 Numerical Model	77
6.1 Overview	77
6.2 Constructing the system's Hamiltonian	79
6.2.1 Baseline model (y-polarized light)	80
6.2.2 Arbitrary linear polarization	82
6.2.3 B_x and B_y components	83

6.2.4	Rotating Wave Approximation	83
6.3	Calculating atomic fluorescence	85
6.3.1	Autler-Townes splitting	86
6.3.2	Doppler broadening	88
6.3.3	Adding more fields	89
6.4	Hanle effect: light emitted along y	90
6.5	Summary	92
7	Beyond the 1D model: vector magnetometer	93
7.1	Introduction	93
7.2	Polarization dependence	93
7.3	Non-zero B_x and B_y components	97
7.3.1	Non-zero B_y	97
7.3.2	Non-zero B_x	101
7.4	Experimental data	104
8	Magnetic field sensing in practice	109
8.1	Introduction	109
8.2	Square-wave sidebands	109
8.2.1	Dark-resonance condition	111
8.3	Mapping B-fields from data	112
8.4	Estimating B_x and B_y from data	115
8.4.1	Model implementation - 10% duty square wave	116
8.4.2	Results (2 MHz modulation frequency)	117
8.5	Laser power dependence	119
8.6	Performance estimates	121
8.6.1	B-field uncertainty	122
8.6.2	Sensitivity	122
8.6.3	Dynamic range	124
8.6.4	B_x, B_y uncertainty from forward simulation	125
9	Conclusion	126

A Code: Stimulated Slowing	128
A.1 Instructions	128
A.2 Python libraries used	129
A.3 Descriptions and pseudocodes	130
A.3.1 Main class file (BCF) <code>SSMCSolver_BCF.py</code>	130
A.3.2 Square wave version: <code>SSMCSolver_square.py</code>	135
A.3.3 Simulation script and parameters (BCF)	136
A.3.4 Simulation script and parameters (Square)	139
A.3.5 Generate atom samples <code>GenerateBatchAtoms.py</code>	140
B Code: Magnetometer	141
B.1 Instructions	141
B.2 Python libraries used	142
B.3 Descriptions and pseudocodes	142
B.3.1 Main class file <code>ATSolver.py</code>	143
B.3.2 Simulation script and parameters	145
B.3.3 Job submission guide	149
Bibliography	151

Chapter 1

Introduction, context, and outline

1.1 Introduction

1.1.1 Slow atoms: stimulated slowing of Yb atoms

Ytterbium (Yb) atoms are one of the leading candidates for ultrastable atomic clocks [1] and processing quantum information [2]. To realize the potential of Yb lattice clocks for applications in fundamental physics [3] and geophysics [4] as an extremely precise time and frequency standard outside laboratory settings, where meticulous stabilization and control are required, has motivated the need for a more compact and simpler design for the complex cold atom experiments that use fewer lasers for cooling, repumping, and trapping atoms in an optical lattice. One possible approach is to eliminate one of the lasers for cooling of Yb atoms, which typically uses both a 399 nm laser and a 556 nm laser for cooling on the broad 1S_0 - 1P_1 transition and the narrow 1S_0 - 3P_1 transition, respectively.

The first half of this thesis presents a proposal [5] to use only the 556 nm for slowing and loading Yb atoms into a magneto-optical trap (MOT), replacing a standard Zeeman slower, which requires the 399 nm laser, with a stimulated slowing technique that only uses the 556 nm laser and the narrow triplet-p 1S_0 - 3P_1 transition. Several approaches [6] to produce stimulated optical forces include pulsed light [7], bichromatic force [8, 9, 10] and adiabatic rapid passage (ARP) [11, 12, 13, 14]. Among these

approaches, we were most interested in investigating bichromatic slowing, which has been demonstrated on alkali atoms [8, 9, 10, 15, 16, 17] and molecules [18, 19]. I developed a numerical model and Monte Carlo simulations that can simulate atoms' trajectories under realistic experimental conditions and help optimize an experimental design for this method. With the laser frequency chirp [17] incorporated to extend the slowing velocity range of the stimulated force, the simulations showed that bichromatic slowing using 1 W of optical power can load a 556 nm MOT at the loading rate of 10^8 atoms/s, a comparable loading rate achieved by Guttridge et al. [20] when using a 399 nm Zeeman slower.

Inspired by the four-color stimulated force [21], produced by adding two additional laser frequencies at $\omega_0 \pm 3\delta$ to the bichromatic frequencies $\omega_0 \pm \delta$, where ω_0 is the resonant frequency of the two-level atom and δ is the bichromatic detuning, I extended the model to include additional optical frequencies that correspond to odd harmonics of δ to mimic a square wave modulation. My simulation shows that the square-wave amplitude- or phase-modulated light can produce comparable slowing forces to the bichromatic force method with an extended velocity range. This square-wave force can improve the MOT loading rate by 70% [5], assuming that the modulation has 100% power efficiency.

To realize this stimulated slowing approach in the laboratory in a transverse beam deflection experiment, square-wave amplitude-modulated laser light at 556 nm was set up in the transverse direction to the thermal Yb atomic beam with a camera located above the intersection between the atomic beam and the laser beam to image the fluorescence. This setup led to a coincidental discovery of a dark-striped pattern across the atomic fluorescence that corresponds to contour lines of constant magnetic fields. Our group's research and my PhD thesis then took an interesting, unexpected turn. In the second half of this thesis, the goal is to understand the origin of the dark stripes and develop the first Yb optical atomic magnetometer based on fluorescence imaging of fast, thermal atoms that offers both rapid spatial imaging and vector capabilities.

1.1.2 Fast thermal atoms: Yb atomic magnetometer

Magnetometers are devices designed to measure magnetic fields or magnetic moments. Over the last century and for broad applications ranging from geophysics, aerospace, fundamental physics, and biomedical applications, numerous magnetometer technologies have been developed. Notable examples include fluxgates [22, 23], Hall-effect devices [24], Superconducting Quantum Interference Devices (SQUIDs) [25, 26], diamond nitrogen-vacancy (NV) centers [27], and atomic magnetometers [28, 29, 30, 31, 32, 33].

While many atomic magnetometers measure the magnitude of the magnetic fields from Larmor precession frequency measurements, polarization rotation, or changes in absorbance (CPT) in the magneto-optical interactions between resonant light and alkali atoms in vapor cells (e.g. Cs, Rb, K) [28, 29, 30, 32, 33], our magnetometer utilizes fluorescence imaging of a thermal Yb atomic beam, which provides a fast, powerful method to take 15,000 spatially resolved measurements at a camera frame rate. Magnetic fields' contour lines and gradients can be mapped from a fluorescence image based on the location of dark stripes that are produced by Autler-Townes (AT) splitting [34] and the Hanle effect [35, 36]. These effects combined have enabled both vector and spatial imaging capabilities in our Yb magnetometer.

Autler-Townes splitting, caused by strong-field AC Stark shifts, is a coherent effect in multilevel V-systems that causes a decrease in fluorescence and absorption, producing a series of visible dark stripes in the fluorescence. Other similar well-studied coherent effects include electromagnetically induced transparency (EIT) [37] and coherent population trapping (CPT) [38]. Some atomic magnetometers use EIT [39, 40, 41, 42] and CPT [43, 44, 45, 46, 47] absorption to measure both the magnitude and direction of the magnetic fields. Our Yb magnetometer is the only known system to use Autler-Townes dark resonance for magnetic field measurements. Because EIT, CPT, and AT absorption and fluorescence depend on the relative angle between the laser polarization and the external magnetic field, the measurements of these coherent effects are sensitive to the vector orientation and enable vector magnetometers.

The Hanle effect [35, 36] describes the redistribution of polarized light emitted by atoms in the presence of magnetic fields. The Hanle effect also determines the

spatial distribution of atoms' fluorescence for given laser polarization and magnetic fields and hence enables vector magnetometers [48, 49]. Similar to our system, Jackson and Durfee [49] developed a Sr magnetometer based on fluorescence imaging of thermal Sr atoms, also two-electron atoms, and the spatial Hanle effect. Unlike our system, they used the $^1\text{S}_0$ - $^1\text{P}_1$ transition to mostly measured near-zero fields in their magneto-optical trap and operated in the weak driving field limit, so they did not observe any dark resonances.

Our Yb magnetometer obtains 15,000 spatially resolved magnetic-field measurements at a video frame rate (3 ms camera-limited frame rate, with image dimensions $30 \text{ mm} \times 10 \text{ mm}$), enabling fast mapping of magnetic fields' contour lines and gradients. As mentioned previously, Jackson and Durfee's Sr magnetometer [49] also used fluorescence imaging for magnetic field mapping. Other magnetic field imaging approaches include absorption imaging [42, 50] and imaging of Bose-Einstein Condensates (BECs) [51, 52]. With their ^{87}Rb spinor BECs, Vengalottore et al. [51] achieved good sensitivity on the order of $\text{pT}/\sqrt{\text{Hz}}$, but data collection took 250 ms for $120 \mu\text{m} \times 120 \mu\text{m}$ image size at $\sim 10 \mu\text{m}$ spatial resolution. While methods like ours and Refs. [49, 50] are less competitive in terms of sensitivity because of broader transition linewidths and fewer atoms, data collection is as fast as the camera exposure time, and these methods allow for vector as well as scalar measurements in addition to a large dynamic range.

Following initial observations of the dark stripes in our experiment, the primary goal of my research is to understand the origin of these dark resonances and how they depend on the magnetic fields. Understanding the effects of magnetic fields and multiple driving laser fields on Yb atoms requires modeling the $^1\text{S}_0$ - $^3\text{P}_1$ transition in Yb as a four-level atom with one ground state and three excited states, as the $^3\text{P}_1$ state has the electronic angular momentum $J = 1$. The Zeeman effect makes the three excited states $m_J = -1, 0, 1$ non-degenerate in non-zero magnetic fields. When two strong driving laser fields are simultaneously in resonance with two transitions in this V-system, the strong-field AC Stark effect causes the states to split resulting in a decrease in observed fluorescence and absorption from Autler-Townes splitting [53]. Taking into account Doppler broadening from the atoms' transverse velocities and

the spacial Hanle effect [35, 54] that defines the atoms' dipole radiation pattern, dark resonances from Autler-Townes splitting are consistent with our observations in the lab.

Both the theoretical model and experimental data have allowed fast, direct mapping of the magnetic fields' contours and gradients. The dark-striped pattern in the fluorescence is visible to the eye and on the simple camera. The model and the data also enable vector measurements. This combination of both imaging and vector capabilities makes our Yb magnetometer a unique system to study and realize its potential to advance quantum sensing.

1.2 Context for the research

Both aspects of this thesis, the stimulated slowing method and optical magnetometry, have been much more extensively studied and realized for alkali atoms than any two-electron atoms. The theoretical, computational, and experimental work included in this thesis provides insights into how both stimulated slowing and magnetometry techniques can be understood and developed for Yb and other alkali earth-like atoms. These two-electron atoms have atomic energy level structures with key characteristics that enable new capabilities. Such characteristics include very narrow optical clock transitions, which are forbidden in fermionic isotopes and often used in atomic clocks [1] and quantum computing [2]. In bosonic isotopes, the ground state 1S_0 has zero nuclear spin and hence no hyperfine structure, making the system simpler for various applications including our magnetometer.

Both research projects covered in this thesis highlight the versatility of the narrow 556 nm 1S_0 - 3P_1 transition in Yb. In the common two-stage cooling approach for Yb, this transition is used in the second cooling stage to reduce the atoms' temperature. Its narrow linewidth of $\gamma = 2\pi \times 182$ kHz allows for a low Doppler temperature limit $T_D = 4.4\mu K$. In this thesis, I show that this transition by itself can be utilized in stimulated slowing, which relies on stimulated emission processes to maintain fast, coherent momentum transfer between atoms and photons despite the small γ . Because the 1S_0 - 3P_1 transition is closed, the model of this process treats the Yb atoms as

two-level atoms. With the density matrix model, we can calculate and optimize the stimulated forces on atoms. The model helps deepen our understanding of this process in both the time and velocity domains and informs an experimental design to optimize the loading rate of atoms into the MOT.

While the stimulated slowing project is purely computational and uses numerical results to motivate an experimental design, the model I developed for the magnetometer project is inspired by experimental data and helps us both understand and predict what we observe in the lab. Instead of a two-level model, a four-level model is needed to account for internal effects on the three Zeeman sublevels in the 3P_1 state. Although this new model is also based on the density matrix calculation, the output of interest is the atomic fluorescence due to internal energy levels instead of external physical quantities such as atoms' velocities and trajectories. Being able to compare the data to the theoretical model has also been very valuable in validating our theory and discovering new features in the data that provide useful information about both magnitudes and directions of the magnetic fields.

1.3 Thesis outline

This thesis is organized as follows. Chapters 2-4 cover the stimulated slowing project, which was extracted with modifications from our article first published in “Stimulated slowing of Yb atoms on the narrow ${}^1S_0 \rightarrow {}^3P_1$ transition” *Phys. Rev. A* **104**, 053117 (2021) [5]. Copyright © 2021 by American Physical Society. Chapters 5-8 then cover the magnetometer project before conclusions and appendices.

Chapter 2 covers the relevant background on atomic ytterbium and laser cooling and trapping of Yb atoms. I summarize the basics of radiative scattering force, which is fundamental to traditional Doppler cooling, and several approaches to produce dipole forces that rely on coherent population transfer via stimulated emissions. This section reviews several approaches to generate stimulated optical forces: pulsed light, bichromatic force, and adiabatic rapid passage (ARP). The concepts and previous work in bichromatic force have been an underlying foundation for our work presented in Chapters 3-4.

Next, in Chapter 3, I go over how I developed a numerical model in Python to calculate the bichromatic force on Yb atoms using the 1S_0 - 3P_1 transition and compute the atoms' trajectories under realistic experimental conditions. Numerically calculated force profiles are presented as well as results from Monte Carlo simulations that show how we can choose the parameters to optimize the number of atoms that are slowed to final velocities smaller than the 556 nm MOT's capture velocity.

Chapter 4 then extended the model to calculate polychromatic “square-wave” forces by including additional frequency sidebands that would be generated by a square-wave modulation. Here I show how to characterize and optimize this force in both the velocity and time domains. With Monte Carlo simulations, I also show that the MOT loading rate can be improved by the square-wave force. This chapter concludes the stimulated slowing portion of the thesis.

Chapters 5-8 cover the magnetometer project. Chapter 5 provides some background and a brief summary of other imaging and vector magnetometers as well as the relevant physics of Autler-Townes splitting and the spatial Hanle effect. I then introduce our four-level model of Yb atoms in Chapter 6. This chapter includes the derivation of the time-dependent Hamiltonian used in all of our calculations under different magnetic field and laser polarization settings. I also present numerically calculated fluorescence with Doppler broadening and the spatial Hanle effect incorporated to better simulate fluorescence imaging in our lab.

In Chapter 7, I demonstrate how the model can be used to investigate the vector capabilities of this magnetometer. I show how adding magnetic field components in x - and y -directions and rotating the laser polarization directions affect the fluorescence pattern. I present the intuition behind these findings, which can be useful in analyzing and making predictions from experimental data, and end the section with an analysis of an example fluorescence dataset taken at a range of polarization angles from vertical to horizontal polarization directions.

After focusing on theory and modeling in Chapters 6-7, Chapter 8 focuses on how this magnetometer works in practice for mapping magnetic fields' contour lines and gradients. I explain our decision to use a low-duty-cycle square wave (10%) in our data collection and how it can be incorporated into the model. Using another dataset

as an example, I demonstrate how we can turn fluorescence images into a magnetic field map and infer all three vector components of the magnetic fields via forward simulation from our current model. This analysis shows how well the numerically calculated fluorescence agrees with the data. I also show how the fluorescence pattern depends on the laser power. This chapter concludes with performance estimates of this magnetometer such as the magnetic field uncertainty, sensitivity, dynamic range, and response time.

Chapter 9 provides concluding remarks for this thesis followed by two appendices, which provide more details on the numerical models in Python that I developed for this research and instructions for users of the code. See Appendix A for the stimulated slowing model and Appendix B for the magnetometer model.

Chapter 2

Laser Cooling and Trapping of Yb

2.1 Introduction

This chapter provides essential background on atomic ytterbium (Yb) and its energy level structure as well as an overview of the laser cooling and trapping approaches that have been developed for Yb atoms. I will introduce relevant concepts and previous work on stimulated slowing methods, which have been demonstrated on other atoms and molecules. These stimulated laser cooling methods are the foundation of Chapters 3 and 4 in this thesis. Chapters 2-4 in this thesis were extracted (with modifications and permission) from our publication “Stimulated slowing of Yb atoms on the narrow $^1S_0 \rightarrow ^3P_1$ transition” *Phys. Rev. A* **104**, 053117 (2021) [5]. Copyright © 2021 by American Physical Society.

Optical forces for laser cooling and trapping of atoms (and molecules) are often produced by cycles of absorption followed by either spontaneous emission or stimulated emission of photons. Standard textbooks [55, 56] and Metcalf’s review article [6] discuss in detail the different sources of optical forces that can be used to slow, cool, and trap atoms. Relevant content from those references is summarized here to provide the background needed to understand the concept and motivation for our work.

I will begin by reviewing the radiative force and Doppler cooling basics in Sec.2.2. Sec.2.3 focuses on other optical forces that are produced by stimulated emission instead of spontaneous emission. I will outline key previous work in the bichromatic

force and briefly discuss a similar optical force produced by π -pulses and adiabatic rapid passage (ARP).

2.2 Atomic ytterbium

Ytterbium (Yb) is a rare earth element with an atomic number of 70. Yb has seven stable isotopes with ^{174}Yb being the most abundant at 31.8%. The seven stable isotopes are listed below [57]:

Isotope	% Natural abundance	Nuclear spin	Spin Statistics
168	0.13	0	Boson
170	3.05	0	Boson
171	14.3	1/2	Fermion
172	21.9	0	Boson
173	16.12	5/2	Fermion
174	31.8	0	Boson
176	12.7	0	Boson

Table 2.1: Natural abundance, nuclear spins, and spin statistics of the seven stable isotopes of Yb [57].

Yb has two outer-shell electrons. Like other closed-shell alkaline earth-like atoms (e.g. Ca, Sr), the $^1\text{S}_0$ - $^3\text{P}_0$ “clock” transition is forbidden in fermionic isotopes. ^{171}Yb has a narrow linewidth of only 44 mHz, which makes it one of the major candidates for optical atomic clocks [1]. Two Yb optical lattice clocks at NIST have achieved 10^{-18} systematic uncertainty and 10^{-19} instability [4]. In quantum information science, recent developments [58, 59] turned ^{171}Yb atoms in a tweezer array into scalable computing qubit platforms. In addition to applications in time and frequency reference and quantum information, cold Yb atoms are of current interest for quantum gases [60, 61], quantum measurements [62], and atom interferometry [63].

While many other experiments utilize the forbidden clock transition and hyperfine structure of ^{171}Yb , in this thesis, I will focus on even isotopes of Yb such as ^{174}Yb , which has zero nuclear spin, and hence no hyperfine splitting and a simple ground state with no sub-structure. The partial energy level diagram is shown in Fig. 2.1

with transition linewidths and lifetimes of the key transitions listed. For a more thorough description of the hyperfine structure and selection rules in Yb transitions, see Loftus's thesis [64] and references therein.

As highlighted in Fig. 2.1, the $^1\text{S}_0$ - $^1\text{P}_1$ (399 nm) and $^1\text{S}_0$ - $^3\text{P}_1$ (556 nm) transitions are used for laser cooling and trapping of Yb atoms. In conventional Doppler cooling, the laser fields corresponding to these transitions generate optical forces to both slow and cool the atoms. The concepts of radiative scattering force are reviewed in the following section.

2.3 Radiative Scattering Force

Absorption followed by spontaneous emission of a photon produce on average a recoil force on an atom in the opposite direction to the photon's emission. Mathematically this force is given by the product of the momentum of each photon $\hbar k$ multiplied with the photon scattering rate. On a simple two-level atom, this spontaneous radiative force is

$$F_{sp} = \frac{\hbar k \gamma}{2} \frac{s}{1 + s + (2\Delta/\gamma)^2} \quad (2.1)$$

, where Δ is the laser detuning and s is the ratio of the laser intensity over the atomic transition's saturation intensity I/I_{sat} , where saturation intensity is given by $I_{sat} = \frac{\hbar\omega}{2\tau(3\lambda^2/2\pi)}$. This radiative force saturates at a maximum value $F_{rad} = \hbar k \gamma / 2$ at large intensities, ultimately limited by the natural linewidth γ of the cooling transition. Because the detuning is subject to the Doppler shift $-\vec{k} \cdot \vec{v}$, the scattering force is thus velocity dependent and suitable for decelerating atoms.

A common deceleration method that utilizes this radiative force is a Zeeman slower [65]. Incorporating a magnetic field gradient, which is most often produced by a solenoid magnet, introduces a spatially dependent Zeeman shift in the cooling transition. This means that the laser detuning, and hence the force, now depends on the atom's position as well as the atom's velocity. With an appropriate magnetic field gradient configuration, the laser (detuned to a fixed frequency) can remain in or near resonance with the atoms as they are being slowed. This method effectively

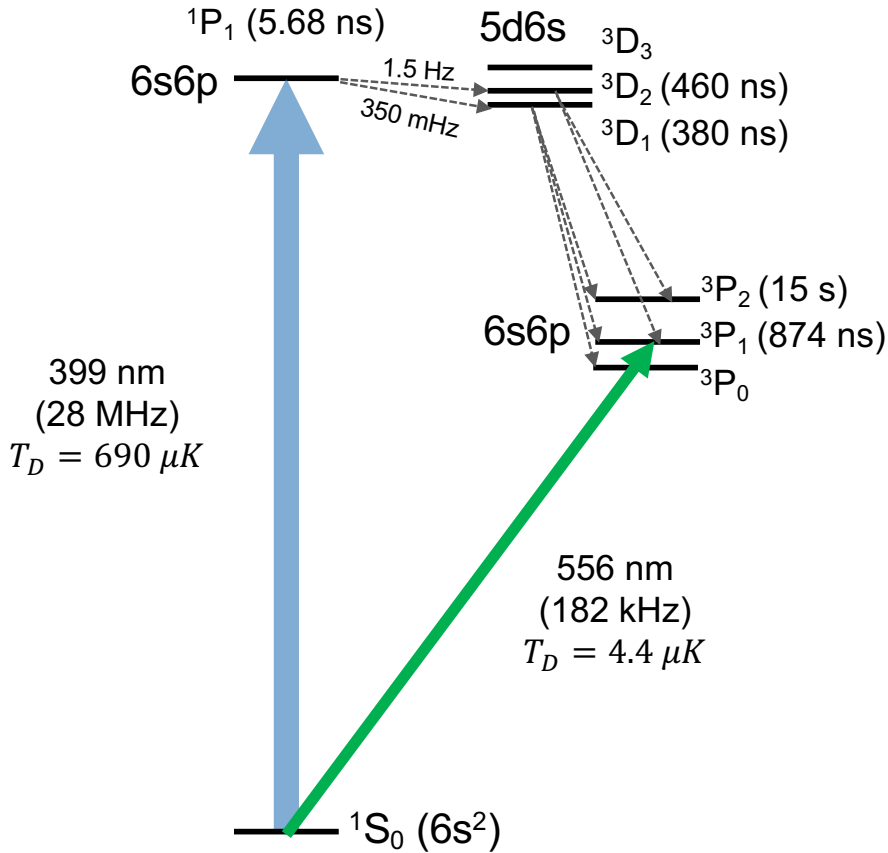


Figure 2.1: Partial energy level diagram of Yb showing two transitions used in two-stage cooling: the $^1S_0 \rightarrow ^1P_1$ (blue) transition for the first stage and the narrower $^1S_0 \rightarrow ^3P_1$ (green) transition for the second stage. Grey dashed arrows show possible decays from 1P_1 to the lower-lying triplet D-states, $^3D_{2,1}$ ($5d6s$), which can lead to further decays to dark $^3P_{2,0}$ states where atoms are lost from the cooling cycles or MOTs unless there is repumping. The lifetimes are extracted from [64] and references therein.

extends the affected velocity range to $\gg \gamma/k$.

Zeeman slowers designed for Yb atoms [64, 66, 67] utilize the $^1\text{S}_0$ - $^1\text{P}_1$ transition at 399 nm for its broad linewidth of $2\pi \times 25$ MHz to achieve a high optical cycling rate and compression of the atoms' velocity distribution. Although much less common than solenoid-based Zeeman slowers, these designs [64, 66, 67] incorporate permanent magnets to produce a strong magnetic field and magnetic field gradient required for effective deceleration of Yb atoms. In Wodey et al.'s design, the magnetic field magnitude on the order of 10 mT was used to produced a maximum deceleration of $-5.3 \times 10^5 \text{ m/s}^2$ [67]. In many experiments, Yb atoms are initially at the typical operating oven temperature of around 450°, at which most atoms are moving at high velocities of at least $\approx 200 \text{ m/s}$, too fast to be captured by magneto-optical traps (MOTs). Pre-slowing with a Zeeman slower can help increase the number of atoms trapped by the MOT, which is often the starting point of cold atom experiments.

Radiative force for cooling and trapping

Beside slowing atoms, the scattering force can be engineered to cool and trap atoms. Because spontaneous emission in random directions is an irreversible process, the scattering force is dissipative in nature and allows for cooling, which requires compression of phase space density. In Doppler cooling, atoms absorb red-detuned photons, receive a momentum recoil, and, on average, lose energy as they undergo spontaneous emission. The radiative force can simultaneously decelerate and cool atoms down to the Doppler temperature limit $T_D = \hbar\gamma/2k_B$, Doppler cooling on the broad $^1\text{S}_0$ - $^3\text{P}_1$ transition alone can bring the atoms' temperature down to $690 \mu\text{K}$ (velocity $v \approx 18 \text{ cm/s}$), which is still relatively high for many cold atom applications.

To overcome this limit on cooling, many Yb experiments introduce an additional cooling stage that utilizes the narrower $^1\text{S}_0$ - $^3\text{P}_1$ transition at 556 nm. This triplet-p transition has a narrow linewidth of 182 kHz, Doppler cooling on this transition can bring the temperature down to temperature in the μK range. This two-stage cooling technique is often used in Magneto-Optical Traps (MOTs). MOTs make up of one or more pairs of counter-propagating laser beams, producing a net velocity-dependent force on atoms in an optical molasses configuration [68] that simultaneously cool and

bring average atoms' velocities down to ~ 1 cm/s. The magnetic field gradient in the MOT, usually generated by a pair of Helmholtz coils, causes spatially dependent Zeeman shifts, which result in a net restoring force that pushes atoms towards the center of the MOT where the magnetic field is zero. In two-color MOTs, the magnetic field gradient needs to be adjusted for each cooling stage [69].

Different MOT designs have been invented for Yb and alkaline earth atoms to optimize the atom number density, temperature, and the loading rate. While some two-color MOTs cool Yb atoms sequentially [69, 70, 71, 72, 73], first with the blue 399 nm light (singlet-p MOT) and then the green 556 nm light (triplet-p MOT), other two-color MOTs apply the two cooling lasers simultaneously [74, 75]. With a Zeeman slower and two-stage MOTs, the atom number of $10^4 \sim 10^7$ atoms and the temperature in the $\sim 40\mu K$ range can be achieved [70, 71, 72, 73]. The final temperature of Yb atoms in the MOT can vary depending on the laser intensity and odd isotopes can reach lower temperatures than even isotopes because of sub-Doppler cooling effects [69, 72].

Besides the low temperature, many experiments need to optimize for the number of atoms for a transfer to optical lattices [70, 71, 73] and other subsequent stages of the experiments. Although a small fraction of atoms in the atomic beam are already slow enough to be directly loaded into a MOT [20], pre-slowing with a Zeeman slower [69, 70, 71, 72, 76, 77], or a 2D MOT [78], or both [67], can increase the MOT loading rate by several orders of magnitude. The loading rate of up to 10^9 atoms/s [67] can be achieved. Despite the higher loading rates, the pre-slowing methods and two-stage cooling approach require additional lasers and make the experimental setup less compact. Another concern when using two-stage cooling is the population loss via decays to dark states, as depicted in Fig. 2.1. Atoms in the 1P_1 state can decay to lower-lying triplet D-states, ${}^3D_{2,1}$ ($5d6s$) and then decay further to long-lived dark ${}^3P_{2,0}$ states.

As an alternative to a two-color MOT, Guttridge et al. directly loaded up to $\approx 10^9$ Yb atoms into a green, triplet-p, MOT [20]. They used high laser intensity of $I = 270I_{sat}$ and a longer loading time of nearly 10 s to circumvent the MOT's small capture velocity $v_c \approx 5$ m/s, which is limited by the 3P_1 transition's narrow linewidth

γ . (For comparison, a typical singlet-p MOT has $v_c \approx 60$ m/s.) With a 399 nm Zeeman slower and high laser intensity, Guttridge et al. achieved a loading rate of 10^8 atoms/s into the triplet-p MOT [20]. On the other hand, without a Zeeman slower and at a lower MOT laser intensity ($I = 160I_{sat}$), Kawasaki et al. reported a much smaller loading rate of 10^4 atoms/s into their green MOT [74]. Both of these results suggest that although it is possible to use only the triplet-p MOT for cooling and trapping, pre-slowing atoms upon loading the MOT is crucial in achieving high MOT loading rate and cold atom numbers. Instead of the radiative scattering forces discussed above, many other slowing methods invented for Yb and alkaline earth atoms rely on dipole forces, which are discussed as follows.

2.4 Dipole Forces

Unlike radiative forces, which are dissipative in nature and rely on the spontaneous emission process, dipole forces are conservative and allow for coherent momentum exchange between atoms and photons via stimulated emissions. For Yb atoms, different techniques employing dipole forces include optical dipole traps [79, 80], optical lattices [70, 71, 73] and Sisyphus cooling [81].

Although strong dipole forces can be produced by a single optical frequency, the sign of the forces alternates on a wavelength scale in the spatial domain such that the forces may average to zero. Introducing an additional light frequency [82, 83] can spatially rectify the sign of the dipole force. Inspired by these proposals [82, 83], later methods including π -pulses, bichromatic slowing, and adiabatic rapid passage utilize multi-frequency and/or swept frequency light to produce even larger forces with extended velocity range. Metcalf's review article [6] and references therein cover all these three approaches. The dipole forces in these methods rely on coherent momentum and energy transfer in stimulated emission processes. Unlike that of spontaneous emission, the rate of stimulated emission is not limited by γ . This allows the stimulated optical forces to be much greater than the spontaneous radiative force when using a narrow transition. In this thesis, we investigate the use of the narrow 1S_0 - 3P_1 transition in Yb (with $\gamma = 2\pi \times 182$ kHz) to produce strong bichromatic

(described below) and polychromatic forces for decelerating atoms [5].

2.4.1 Pulsed light

One approach to realize optical forces larger than F_{rad} [82] is to use two colliding, non-overlapping pulse trains to induce a series of stimulated emissions in atoms. For an atom traveling in a $+z$ direction, starting in the ground state, a pulse of light traveling in the opposite direction can excite the atom, producing a momentum recoil $-\hbar k$. Then the second pulse traveling in the same direction as the atom can induce stimulated emission, transferring another $-\hbar k$. The direction of the decelerating force is maintained as long as the pulse traveling in the $-z$ direction precedes the other direction. In practice, short π pulses (ps pulse trains) from mode-locked lasers can be used [7] to enable fast momentum transfer.

This intuitive π -pulse model was initially adopted to describe stimulated forces produced by bichromatic light fields [10], which consist of superposing CW beams at frequencies $\omega_0 \pm \delta$ traveling in both $\pm z$ directions. Although the bichromatic force (BCF) also relies on counterpropagating light fields to induce a series of stimulated emissions, the π -pulse model described above cannot fully describe the effects of overlapping pulses on the magnitude and velocity range of the force. The bichromatic force (BCF) approach is discussed in Sec. 2.4.2 below.

Beside decelerating atoms, coherent momentum transfer via a series of π and $\pi/2$ pulses finds applications in light-pulse atom interferometry. To enhance the interferometer space-time area and sensitivity, large momentum transfer (LMT) interferometers [84, 85, 86] utilize pulses engineered to maximize the wavefunction separation to achieve two distinct atoms' trajectories. Recently for Sr, momentum separation of over $400\hbar k$ was achieved via Floquet atom optics [87].

In addition to applications of pulses where spontaneous emissions are suppressed, pulse trains can also be used for Doppler cooling of two-level [88] and multi-level atoms [89].

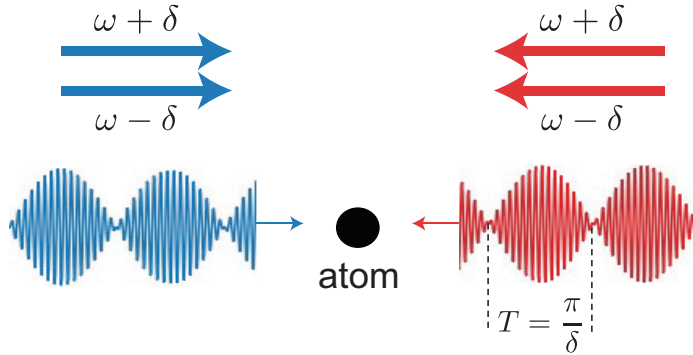


Figure 2.2: Bichromatic light field configuration in an atom’s rest frame (adapted from [10]).

2.4.2 Bichromatic Force (BCF)

Bichromatic force (BCF) can be produced by co- and counter-propagating beams of light that are equally detuned by $\pm\delta$ from atomic resonance (see Fig. 2.2). For a large detuning $\delta \gg \gamma$, and with sufficient optical power, this force can be much stronger than the maximum radiative force $F_{rad} = \hbar k \gamma / 2$ and have a much wider velocity range than $\sim \gamma/k$. Following early stimulated slowing experiments on Na atoms [8, 9], Söding et al. decelerated Cs atoms with a substantial bichromatic force of $\approx 10 F_{rad}$, which has an extended velocity range of $\approx 50\gamma/k$ [10]. They also developed a numerical model of BCF on a two-level system.

In the bichromatic light-field configuration, superposing light at two frequencies (in each direction) produces a net amplitude modulation that maintains a coherent momentum exchange between the atom and incoming photons in both directions; an atom absorbs a photon from one direction and undergoes a stimulated emission when another photon arrives from the opposite direction. The bichromatic light fields traveling in the opposite directions have a phase difference χ that determines the order of and time interval between photon arrivals from alternating directions. Both the Rabi frequency Ω of the light fields and bichromatic detuning δ determine the optical cycling rate due to stimulated emissions. From these parameters, Söding et al. calculated the bichromatic force by solving the optical Bloch equations (OBEs) numerically [10]. Their model and experiment found that the conditions $\chi = \pi/4$ and

$\Omega/\delta = \sqrt{3/2} \approx 1.2$ optimizes the magnitude and velocity range of the force. At the optimal condition, the magnitude of the BCF is

$$F_{BCF} = \frac{\hbar k \delta}{\pi}, \quad (2.2)$$

which can be much larger than the radiative force $F_{rad} = \hbar k \gamma / 2$ for chosen $|\delta| \gg \gamma$. They also observed a significant improvement in the velocity range of the force $\sim \delta/k$ from that of the radiative force $\sim \gamma/k$. Since this force requires that $\Omega/\delta = \sqrt{3/2} \approx 1.2$. The force effectively scales with both δ and $\Omega = \gamma \sqrt{I/2I_{sat}}$, and hence a large force still requires $I \gg I_{sat}$.

To understand the origin of the large force and the increased velocity range, Yatsenko and Metcalf [90] extended the proposed dressed-atom description [91] for a two-level atom in bichromatic light fields. In this picture, the dressed atom is represented by an infinite set of equally spaced energy levels with spacing $\hbar\delta$ between two consecutive levels. A Floquet Hamiltonian describing the system is a function of Rabi frequency Ω , bichromatic detuning δ , and position z . Numerically solving for the eigenenergies as a function of position revealed possible paths for moving atoms to undergo Landau-Zener (LZ) transitions [92, 93] between different eigenenergy manifolds. These transitions require crossings of the eigenstates and are allowed when $\Omega = \sqrt{3/2}\delta (\approx 1.2\delta)$ and the relative spatial phase is $\lambda/8$ (equivalent to $\chi = \pi/4$) [90, 94]. In this picture, they also derived the magnitude of the BCF and argued that for LZ transitions that would not reverse the direction of the force, the velocity range of BCF is at least $\sim \delta/2k \gg \gamma/k$ [90].

Following early experiments on Na and Cs, later bichromatic slowing experiments were demonstrated on other atoms including Rb [15, 16, 17], He* [95, 96, 97], and Ar* [98]. Williams et al.'s early experiment in Rb [15] measured the bichromatic force as a function of atom's velocity and verified the optimal conditions for the force. Their results agreed well with previous theoretical work including the numerical model developed by Söding et al. [10]. While some experiments used the BCF to deflect [95] or collimate [96] an atomic beam, Liebisch et al. implemented the stimulated slowing technique to load Rb atoms into a MOT and improved the loading rate by a

factor of 20 [17] with a relatively small force $\approx 2.2F_{rad}$. Their results have inspired our stimulated slowing proposal to load Yb atoms into a MOT.

Although the velocity range $\sim \delta/2k$ of the bichromatic force is already a significant improvement from that of the spontaneous radiative force $\sim \gamma/k$, it is still challenging to slow light atoms (e.g. He*) for their higher average velocities and broader velocity distributions. Chieda and Eyler investigated two approaches to extend the velocity range of BCF on He* [97]. One intuitive approach is to use the largest possible δ . However, increasing δ would require increasing the Rabi frequency Ω , and hence the laser power, in order to maintain the optimal ratio $\Omega/\delta = \sqrt{3/2}$ for BCF. Even if this condition is satisfied, Chieda and Eyler found that the BCF stopped improving at a detuning δ of $\approx 250\gamma$ for He* (this limit may be different for other atoms). Alternatively, a more promising approach that does not require extremely large δ and Ω is to sweep the Doppler shifts $\pm kv$ such that the force stays in resonance with the atoms as they are being slowed. This laser frequency chirp method has been shown to slow He* atoms by over 300 m/s [97]. In our proposal for Yb, we adopt this laser frequency chirp method for slowing Yb atoms from velocities over 200 m/s down to the MOT capture velocity ≈ 5 m/s, as discussed in Chapter 3.

Following the demonstrations of the bichromatic force on alkali atoms and He*, more recent efforts have extended the concepts [99, 100, 101, 102, 103, 104] and experiments [18, 19] for molecules. Laser cooling of molecules are generally harder to achieve due to their multilevel structure that often has multiple loss channels. Many repumping lasers are often required to retrieve population losses due to spontaneous emissions. The bichromatic slowing method shows promise in decelerating of molecules because faster optical cycling and coherent momentum exchange via stimulated emissions suppress the effects of spontaneous emissions.

Four-Color Force

Another proposal to improve the bichromatic force's magnitude and velocity range is to add the third harmonic of the original bichromatic detuning δ [21]. With their numerical calculations, Galica, Aldridge and Eyler showed that adding the new frequency components increased the magnitude of the force by nearly 50% and extended

the velocity range by a factor of 3, when using about 33% more laser power in total. They argued that the added third harmonics modified the overall pulse shape such that it more closely resembles a π -pulse rather than overlapping pulse trains. Plotting the evolution of two components of the Bloch vector $v(t) = i(\rho_{01} - \rho_{10})$ and $w(t) = \rho_{11} - \rho_{00}$ over time also showed that the four-color force led to faster cycling between the ground and excited state with less wobble [21] around the ground state. More details on this are discussed in Chapter 3, where we show similar Bloch vector trajectory plots produced from our numerical simulations.

Overall, Galica et al.'s improvement to the bichromatic force scheme has inspired us to investigate different types of amplitude modulation of light fields used in stimulated slowing. In particular, Galica et al.'s use of the third harmonic of the bichromatic detuning δ prompted us to investigate the square-wave AM, as described in Chapter 4. We also plotted similar Bloch vector trajectories and found that, similar to the proposed four-color force, the system subject to the square-wave PCF behaves more similar to that driven by π -pulses. The two-level atom undergoes faster cycling between the ground and excited states with less wobble around the ground state (see Fig. 4.4).

2.4.3 Adiabatic Rapid Passage (ARP)

Another approach to produce large optical forces on atoms without spontaneous emission is Adiabatic Rapid Passage (ARP). ARP can produce large optical forces [11, 12, 13, 14] via rapid momentum exchange between light pulses and an atom. Similar to the common π -pulse configuration, ARP requires an alternating sequence of pulses traveling in two opposite directions. The major difference is that the detuning $\delta(t)$ of each arriving pulse is rapidly swept from a large red detuning $-\delta_0$ to a large blue detuning δ_0 (through zero) at a fast sweep rate of ω_m . ω_m also sets the pulse rate, such that each pulse duration is given by π/ω_m .

The fast detuning sweep in ARP is essential for inverting the atom's population. On a Bloch sphere, the Bloch vector $\vec{R} = (u, v, w)$ representing the state of a two-level atom precesses about the light field's torque vector $\vec{\Omega}(t) = (\Omega_r, \Omega_i, \delta(t))$, as described

by

$$\frac{d\vec{R}}{dt} = \vec{\Omega}(t) \times \vec{R} \quad (2.3)$$

, where the light-field vector components Ω_r and Ω_i are real and imaginary parts of the Rabi frequency and δ is the detuning. With the ARP pulses configuration, both the Rabi frequency $\Omega(t)$ and the detuning $\delta(t)$ are changing in time. By rapidly sweeping the detuning from a large red detuning $-\delta_0$ to zero and to δ_0 , the torque vector $\vec{\Omega}$ rotates from the south (ground state) to the north pole (excited state) on the Bloch sphere while the Bloch vector \vec{R} continues to precess around $\vec{\Omega}$, effectively producing a population inversion. See references [6, 14] for illustrations of the Bloch vector trajectory on the Bloch sphere during an ARP cycle.

ARP requires a large torque vector $|\vec{\Omega}|$, a high sweep rate $\omega_m \gg \gamma$ to suppress effects from spontaneous emission, and a broad sweep range δ_0 compared to both Ω_r and Ω_i to ensure that the vector $\vec{\Omega}$ is nearly polar at the beginning and end of one sweep. The detuning sweep in ARP is not to be confused with laser frequency chirp that has been introduced in bichromatic slowing [97] to extend the velocity range of the force. In our BCF simulation (Chapter 3), the laser frequency is swept over a significantly longer timescale (a few ms) compared to how fast the Rabi frequency is changing (≈ 10 ns). In ARP, on the other hand, both the Rabi frequency variation and the detuning sweep occur at the same rate ω_m [14]. Ideally, a large sweep rate $\omega_m \gg \gamma$ results in a large optical force of

$$F_{ARP} = \frac{2\hbar k}{2\pi/\omega_m} = \frac{\hbar k \omega_m}{\pi}, \quad (2.4)$$

which has a similar form to the bichromatic force (2.2). Numerical calculations done by Stack et al. [14] showed that the velocity range of ARP force is at least $\sim \delta_0/4k$, where δ_0 is the detuning sweep range.

Following a deflection experiment in He* [13], more recent work applied adiabatic cooling techniques inspired by ARP on Sr [105], dysprosium [106], and molecules [107]. For Sr, Sawtooth-Wave Adiabatic Passage (SWAP) has been demonstrated [105] on the narrow 7.5 kHz 1S_0 - 3P_1 transition in Sr. Theory work [108, 109] on SWAP cooling

showed a potential application in a 1D MOT [109] and suggested possible generalizations [108] to other 2-electron atoms (alkaline earth or alkaline-earth-like atoms). So far, none of the ARP approaches has been applied on Yb atoms.

2.5 Summary

We have reviewed cooling and slowing techniques, which utilize optical forces from either spontaneous or stimulated emissions, and covered many methods that were demonstrated on Yb and other alkaline-earth-like atoms. In addition to all the approaches discussed above, other slowing and cooling methods applied on alkaline-earth-like atoms include Sisyphus-like deceleration [81], two-photon cooling [110], two-color cooling [75, 111], and quenched narrow-line cooling [80, 112, 113] that takes advantage of the narrower transitions to achieve very low temperatures. Combining several of these techniques can produce an ultracold atom source with higher phase-space densities [114].

Our goal is to develop a stimulated slowing approach for Yb atoms that uses only the narrow $^1S_0 \rightarrow ^3P_1$ transition for both slowing and trapping of Yb atoms while maintaining a high loading rate into the triplet-p MOT. We theoretically demonstrate in chapters 3 and 4 of this thesis that using stimulated methods on the narrow $^1S_0 \rightarrow ^3P_1$ transition in Yb can produce large forces and a high loading rate into the MOT.

Chapter 3

Stimulated Slowing with Bichromatic Force

3.1 Introduction

This chapter details the theory and computer simulation of stimulated slowing of Yb atoms with counter-propagating bichromatic light fields on the narrow $^1S_0 \rightarrow ^3P_1$ transition. The model includes numerical calculation of bichromatic force (BCF) and Monte Carlo simulation to estimate the number of slowed atoms that can be trapped by a 556 nm MOT. The simulation methods, results and the optimization of the MOT loading rate are described. The chapter concludes with a discussion of a broadband cooling method, in which additional bichromatic slowing beams are added to broaden the velocity range of the BCF. Much of this chapter and the next chapter are based on our publication [5].

3.2 Numerical model

Our stimulated slowing proposal for Yb atoms aims to eliminate the need for the first-stage cooling using the 399 nm transition. As shown in Fig. 3.1, the narrow $^1S_0 \rightarrow ^3P_1$ transition is used for both slowing and the MOT. Using only one cooling laser instead of two could enable more compact experimental setups for cold Yb. Removing

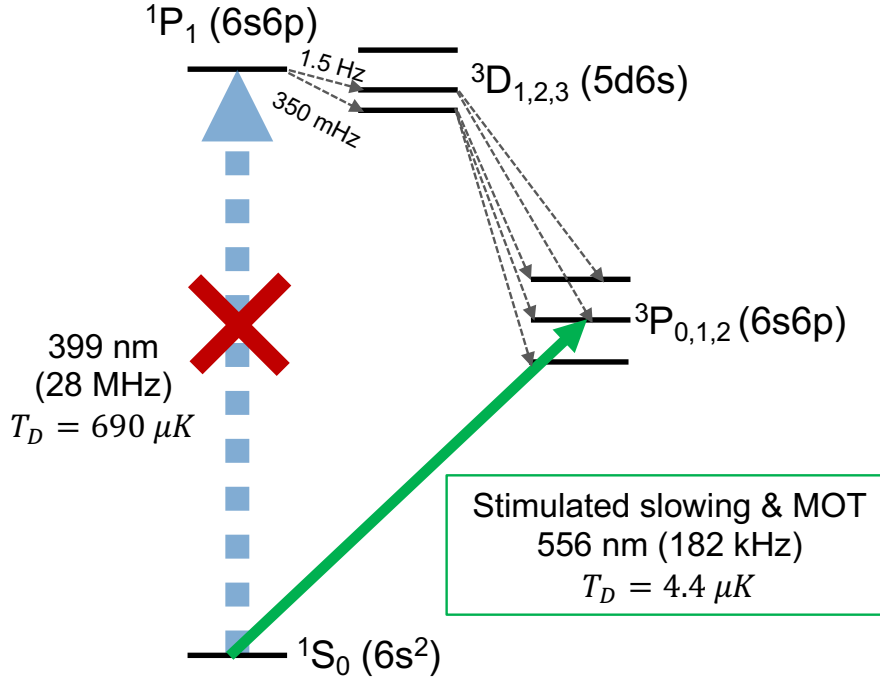


Figure 3.1: Energy level diagram of Yb showing the $^1S_0 \rightarrow ^1P_1$ transition (solid arrow), which is used for both stimulated slowing and magneto-optical trapping. The stimulated slowing method eliminates the need for the traditional first-stage cooling on the 1P_1 transition and helps avoid population loss via decays from 1P_1 to the lower-lying triplet-D states, $^3D_{2,1}$ ($5d6s$), which can lead to further decays to dark $^3P_{2,0}$ states where atoms are lost from the cooling cycles or MOTs without repumping.

the transition to the 1P_1 state also helps avoid population loss when atoms decay to the lower-lying triplet-D states and then to the dark states $^3P_{0,2}$, as shown by the grey dashed arrows in Fig. 3.1.

With our numerical model developed in Python, we investigate stimulated slowing approaches that utilize bichromatic (this chapter) and polychromatic (chapter 4) forces. With a density matrix approach, the model numerically calculates optical forces on atoms and integrates the force to compute the atoms' trajectories as they travel from the oven to the triplet-p MOT region. To evaluate the slowing efficiency, the model incorporates Monte Carlo simulations, which sample atoms' initial velocities and positions from known distributions, to estimate the fraction

of atoms in the atomic beam that can be trapped by the MOT after the slowing process. Different stages and components of the model are described in detail as follows. The Python codes and documentation developed for this project are on GitHub, <https://github.com/tinatn29/Yb-slowing>. Pseudocodes and instructions are also presented in Appendix A.

3.2.1 Calculating bichromatic force (BCF)

We developed our initial model in Python to calculate the bichromatic force (BCF) on two-level atoms. Similar to what was implemented in [10], our initial model assumes a two-level atom traveling in a bichromatic standing wave. The two-level model is well-suited for the 1S_0 - 3P_1 transition, especially for the even isotopes with nuclear spin $I = 0$. Each amplitude-modulated wave consists of two beating frequencies $\omega \pm \delta$, which are detuned to compensate for the Doppler shifts (Fig.3.2a). Other key parameters include the Rabi frequency Ω and relative phase χ between the blue-detuned and red-detuned light fields. We can calculate the BCF on atoms from the time-dependent Hamiltonian $H(t)$ and the density matrix $\rho(t)$, which is obtained by numerically solving the Optical Bloch Equations (OBEs).

Based on the original calculations done by former group members TianMin Liu and Nikhil Raghuram, we first derive the time-dependent Hamiltonian $H(t)$ of the two-level atom interacting with the four CW beams. In order to slow atoms with velocity v_d , we detune the counter-propagating beams by $-kv_d$ and the co-propagating beams by $+kv_d$ from the resonant frequency ω . In the rest frame of an atom moving at an arbitrary longitudinal velocity v (v does not have to be equal to v_d), the frequencies of the counter-propagating fields become $\omega - kv_d \pm \delta + kv = \omega \pm \delta + k(v - v_d)$. Assuming the electric field amplitude E_0 to be identical in all of the four CW beams, the counter-propagating, red-detuned light fields are given by

$$\begin{aligned}\varepsilon_{red} &= E_0 \cos [(\omega + \delta + k(v - v_d))t + kz] + \cos [(\omega - \delta + k(v - v_d))t + kz] \\ &= 2E_0 \cos [(\omega + k(v - v_d))t + kz] \cos (\delta t)\end{aligned}$$

We can write down similar expressions for the co-propagating, blue-detuned fields. In

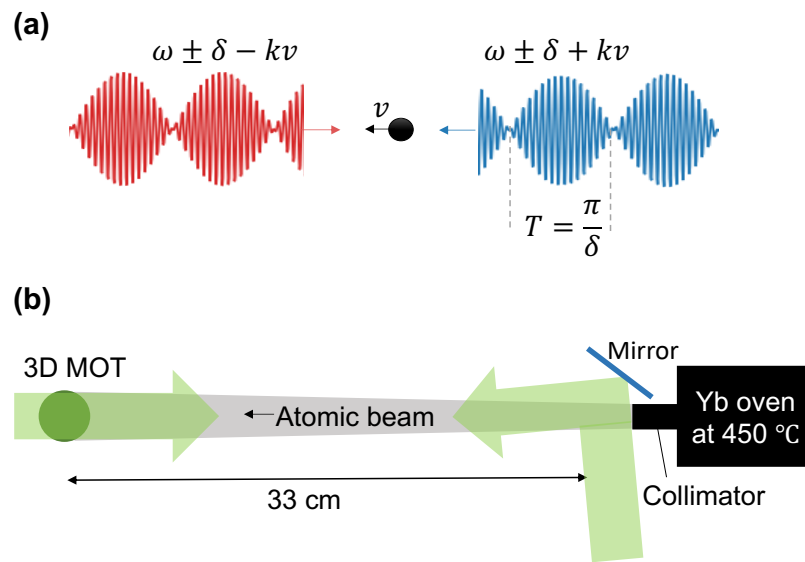


Figure 3.2: (a) An atom traveling in counter-propagating bichromatic light fields with a velocity v . The laser beam frequencies (in the lab frame) are detuned by $+kv$ and $-kv$ to compensate for Doppler shifts. (b) A schematic diagram of our experimental setup showing a Yb atomic beam leaving an oven at 450 °C and two counter-propagating laser beams at 556 nm. The atoms are slowed over a distance of 33 cm before reaching the MOT region. Our current Yb atomic beam is partially collimated by a tubular array nozzle and diverges with a half-angle ≈ 17 mrad.

the same atom's rest frame, the blue-detuned light fields have frequencies $\omega + kv_d \pm \delta - kv = \omega \pm \delta - k(v - v_d)$ and are phase shifted by χ with respect to the red-detuned light fields.

$$\begin{aligned}\varepsilon_{blue} &= E_0 \cos [(\omega + \delta - k(v - v_d))t - kz + \chi] + \cos [(\omega - \delta - k(v - v_d))t - kz - \chi] \\ &= 2E_0 \cos [(\omega - k(v - v_d))t - kz] \cos (\delta t + \chi)\end{aligned}$$

The total electric field in the complex form is given by

$$\begin{aligned}\varepsilon &= \varepsilon_{blue} + \varepsilon_{red} \\ &= \frac{E_0}{2} (e^{i[(\omega - k(v - v_d))t - kz]} + e^{-i[(\omega - k(v - v_d))t - kz]})(e^{i(\delta t + \chi)} + e^{-i(\delta t + \chi)}) \\ &\quad + \frac{E_0}{2} (e^{i[(\omega + k(v - v_d))t + kz]} + e^{-i[(\omega + k(v - v_d))t + kz]})(e^{i\delta t} + e^{-i\delta t})\end{aligned}$$

Using the dipole approximation and letting the Rabi frequency $\Omega = \frac{eE_0}{\hbar} \langle 1 | r | 0 \rangle$, we can write down the interaction Hamiltonian $H_I = -\hat{d} \cdot \vec{\varepsilon}$ from the electric field expression, where \hat{d} is the transition dipole moment. With the rotating wave approximation, we can drop fast-rotating terms because $\omega \gg \delta, kz, k(v - v_d)$. The 2×2 Hamiltonian $H(t)$ becomes

$$H(t) = \begin{bmatrix} 0 & H_{01}(t) \\ H_{10}(t) & 0 \end{bmatrix}$$

where the off-diagonal components $H_{01} = H_{10}^*$ are given by

$$\begin{aligned}H_{01}(t) &= \frac{\Omega}{2} [e^{-i[k(v - v_d)t + kz]} (e^{i(\delta t + \chi)} + e^{-i(\delta t + \chi)}) + e^{i[k(v - v_d)t + kz]} (e^{i\delta t} + e^{-i\delta t})] \\ &= \Omega [e^{-i[k(v - v_d)t + kz]} \cos (\delta t + \chi) + e^{i[k(v - v_d)t + kz]} \cos (\delta t)]\end{aligned} \quad (3.1)$$

Note that for now we have assumed the electric field amplitude E_0 , and hence the Rabi frequency Ω , of each of the slowing beams to be identical. The effects of power imbalance on stimulated forces were discussed in [21], where Galica et al. found that the stimulated forces decreased when the beams were imbalanced.

Having derived the Hamiltonian $H(t)$, we then solve the optical Bloch equations

(OBEs) for the density matrix ρ using a built-in Linblad Master equation solver from the QuTip library [115, 116]. The Linblad master equation is given by

$$\dot{\rho}(t) = -i\hbar[H(t), \rho(t)] + \frac{1}{2}[2C\rho(t)C^\dagger - \rho(t)C^\dagger C - C^\dagger C\rho(t)] \quad (3.2)$$

In Eq.(6.19), spontaneous emissions are included via a collapse operator $C = \sqrt{\gamma}|0\rangle\langle 1|$, where $|0\rangle$ and $|1\rangle$ denote a two-level atom's ground and excited states, respectively. After solving Eq.(6.19) for ρ , the force is computed from $F(t) = \hbar\frac{\partial}{\partial z} \text{Tr}(\rho H)$. We found that setting $\Omega/\delta = \sqrt{3/2}$ and $\chi = \pi/4$ optimized the magnitude and velocity range of the BCF. Our results are consistent with previous numerical work [10, 90, 21]. Figure 3.3 shows the stimulated forces plotted against atomic velocity for three different values of δ and the respective Rabi frequency $\Omega = \sqrt{3/2}\delta$. The force profile is centered at zero velocity as we initially set the velocity detuning $v_d = 0$. At this optimal ratio and phase $\chi = \pi/4$, the magnitude of the bichromatic force is given by

$$F_{BCF} = \frac{\hbar k \delta}{\pi} \quad (3.3)$$

Since we can choose $\delta \gg \gamma$, F_{BCF} can be much larger than the radiative force $F_{rad} = \hbar k \gamma / 2$ and can have a broad velocity range of $\Delta v \sim \delta/2k \gg \gamma/k$ [90]. The red (upper) curve in Fig.3.3 corresponds to $\delta = 150\gamma$ and $\Omega = 184\gamma \approx 2\pi \times 33$ MHz, which produces a BCF with magnitude $\approx 90F_{rad}$. Another key feature of the BCF is sharp Doppler resonances at velocities $v = \pm\delta/(2n+1)k$, $n = 0, 1, 2, \dots$ [117]. However, these sudden increases in the stimulated force were not observed in bichromatic force measurements [15, 16] and do not affect the slowing process significantly.

3.2.2 Monte Carlo simulation

As shown in Fig.3.3, both the magnitude and velocity range of the bichromatic force show promise for stimulated slowing in loading atoms into a MOT [7]. To investigate the effects on the atoms' velocity distribution and inform an experimental design that optimizes the MOT loading efficiency for Yb atoms, we developed Monte Carlo

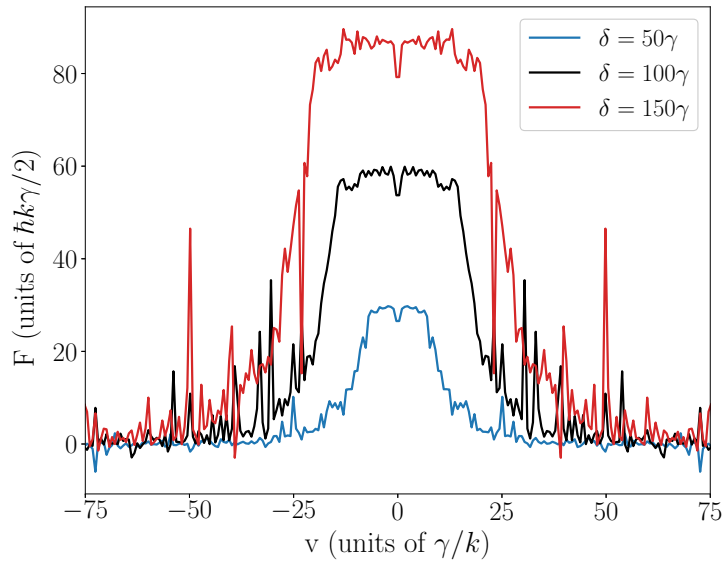


Figure 3.3: Bichromatic force (BCF) as a function of atomic velocity for $\delta = 50\gamma$ (blue, lower line), 100γ (black, middle line), 150γ (red, upper line), Rabi frequency $\Omega = \sqrt{3/2}\delta$, $\chi = \pi/4$. The magnitude and range of the force scale linearly with δ . At $\delta = 150\gamma$ and $\Omega = 184\gamma$ (red, upper line), the maximum stimulated force is near $90F_{rad}$ and acts over the velocity range of $\pm 30\gamma/k \approx 3$ m/s for the $^1S_0 \rightarrow ^3P_1$ transition in Yb. Note that, for optimal performance, large δ requires higher laser power (to keep $\Omega/\delta = \sqrt{3/2}$). Both the force magnitude and velocity width increase with laser power.

simulations to estimate the number of atoms that can be trapped by the MOT after being slowed.

For computational speed and sufficient statistical significance of the results, we choose to include roughly 20,000 atoms in each simulation. For an individual atom with a given velocity and position, we compute the bichromatic force by following the steps described in Sec.3.2.1 and then integrate the force to update the atom's velocity and position at every 10 μs interval. This time interval is approximately the time it takes for an atom's velocity to change by γ/k under the stimulated force. Our simulations account for the atomic beam system's geometry and other realistic experimental conditions including the atoms' velocity distribution, atomic beam divergence, and the Gaussian laser beam profile. We describe below how these different conditions are determined.

Atom's velocity distribution

Our simulations integrate the atomic beam system's geometry as illustrated in Fig.3.2b. Yb atoms leave a 450 °C oven, where the total atomic beam flux from the collimator is 10^{11} atoms/s, and travel in a bichromatic light field, defined by the key parameters δ and Rabi frequency Ω , towards a 3D 556 nm MOT located 33 cm away from the oven aperture, which has a small diameter of 4 mm. The atomic beam is slowly diverging with a 17 mrad half-angle of divergence. In a simulation, before the light fields are “switched on,”, a batch of atoms needs to be generated with the atoms' initial velocities and positions in 3-D. We first describe how we sample each atom's velocity components (v_x, v_y, v_z).

We first consider the speed $v = \sqrt{v_x^2 + v_y^2 + v_z^2}$. The speed of atoms exiting an effusion oven follows the probability distribution function (PDF)

$$f_e(v) = 2 \left(\frac{m}{2k_B T} \right)^2 v^3 \exp \left(-\frac{mv^2}{2k_B T} \right) \quad (3.4)$$

This effusion velocity distribution gives the average speed of $\bar{v} = \frac{3}{4} \sqrt{\frac{2\pi k_B T}{m}} \approx 350$

m/s at the oven temperature of 450 °C. Compared to the Maxwell-Boltzmann distribution with PDF $f_{MB}(v) \propto v^2 \exp(-mv^2/2k_B T)$, having v^3 instead of v^2 in Eq.(3.4) increases the average speed and makes the atoms sampled from the effusion distribution $f_e(v)$ more likely to have greater speeds. Intuitively, the extra factor of v in the effusion distribution reflects on faster atoms being more likely to escape the oven through a small nozzle. While it is straightforward to sample v from the Maxwell-Boltzmann distribution because the velocity components v_x , v_y and v_z follow a normal distribution, sampling v from the effusion distribution requires an additional step. We describe below the acceptance-rejection sampling method [118] we used to prepare the atom samples for the simulation.

The acceptance-rejection sampling method is a Monte Carlo algorithm that samples a random variable x from a target distribution with PDF $f(x)$ by using a proposal distribution with PDF $g(x)$, which we know how to sample from, given that there exists a finite bound $f(x) \leq cg(x)$ for all x and $1 < c < \infty$. In our case the Maxwell-Boltzmann distribution is the proposal distribution. We can sample a speed v from $f_{MB}(v)$ by sampling three velocity components (v_x, v_y, v_z) from a normal distribution with zero mean and variance of $2k_B T/m$, then compute $v = \sqrt{v_x^2 + v_y^2 + v_z^2}$.

The effusion PDF is bounded by a positive multiple of f_{MB} . For example, Fig.3.4 shows that $f_e(v) \leq cf_{MB}(v)$ for an arbitrary $c = 3$. We can apply the acceptance-rejection sampling method by first sampling a speed v_s from the Maxwell-Boltzmann distribution and then uniformly sampling a number between 0 and $cf_{MB}(v_s)$. This is equivalent to randomly picking a value along the vertical line $v = v_s$ that is below the black dashed line in Fig.3.4 and can be done by multiplying $cf_{MB}(v_s)$ with a random uniform number $u \sim U[0, 1]$ between 0 and 1. If the sampled value $ucf_{MB}(v_s)$ is below the desired PDF value $f_e(v_s)$, i.e., the red curve on the graph, then we accept v_s as a sample from the effusion distribution. We reject v_s and re-sample if $ucf_{MB}(v_s) > f_e(v_s)$. We repeat the process until we reach around 20,000 samples. Figure 3.5 shows the histogram of v sampled by this method ($N = 20,000$) along with the PDF $f_e(v)$. in Fig.3.5.

Having devised a method to sample v , we can now look at the velocity components (v_x, v_y, v_z) . In the transverse directions, we can assume v_x and v_y follow the Gaussian

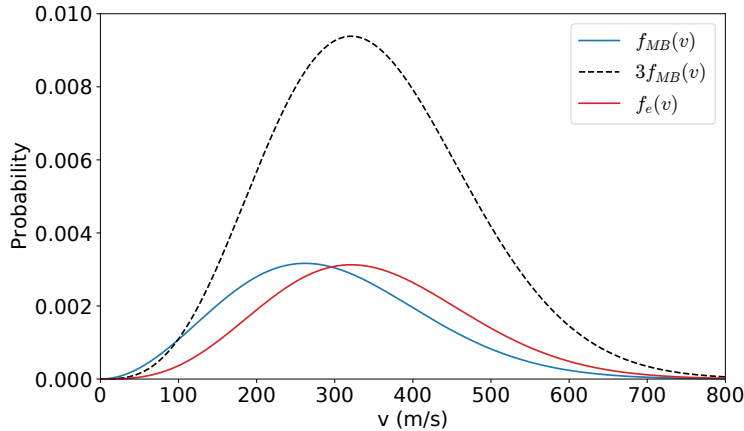


Figure 3.4: Probability density functions for the Maxwell-Boltzmann distribution f_{MB} (blue) and the effusion velocity distribution f_e (red). Note that $f_e(v) \leq 3f_{MB}(v)$ (black dashed line) for all v .

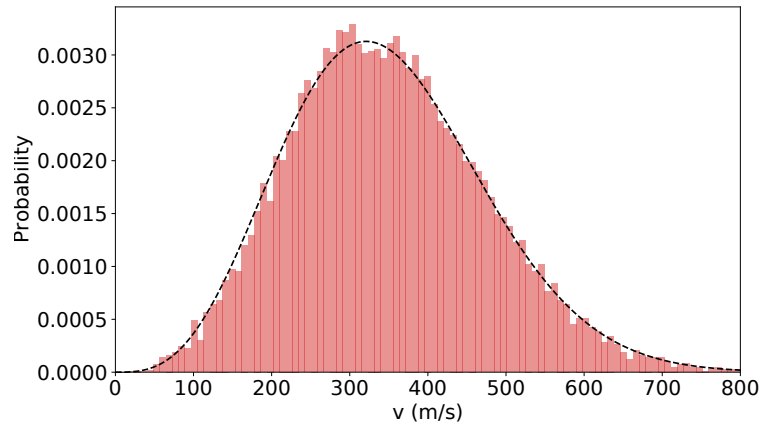


Figure 3.5: Histogram of the sampled speed v from the effusion velocity distribution using the acceptance-rejection sampling method along with the PDF $f_e(v)$.

distribution with zero mean and standard deviation σ_t . To estimate σ_t , we first calculate the standard deviation of the speed v from the effusion PDF. Using $f_e(v)$ from Eq.(3.4) and the variance formula, $\text{Var}(v) = \langle v^2 \rangle - \langle v \rangle^2$, we obtain

$$\sigma_v^2 = \text{Var}(v) = \frac{2k_B T}{m} \left(2 - \frac{9\pi}{16} \right) \approx \frac{k_B T}{2m} \quad (3.5)$$

where $\langle v \rangle = \int_0^\infty v f_e(v) dv$ and $\langle v^2 \rangle = \int_0^\infty v^2 f_e(v) dv$.

Because the atomic beam is directional ($v_z > 0$) and collimated with a small angle of divergence, we assume the distribution of the longitudinal velocity component v_z to be very similar to the effusion distribution. We approximate the longitudinal velocity width σ_{v_z} to be $\sigma_v \approx \sqrt{k_B T / 2m}$. With the half-angle of divergence 17 mrad, we estimate the full velocity width in the transverse direction to be

$$\sigma_t = 2 \times 0.017 \times \sqrt{\frac{k_B T}{2m}} \approx 4.5 \text{ m/s} \quad (3.6)$$

Therefore, v_x and v_y follow the normal distribution with zero mean and standard deviation of ≈ 4.5 m/s. For each atom, we sample the speed v from effusion distribution followed by the transverse velocities v_x and v_y from the normal distribution $N(0, \sigma_t)$ (only accepting cases where $v \geq \sqrt{v_x^2 + v_y^2}$, and then compute the respective $v_z = \sqrt{v^2 - v_x^2 - v_y^2}$.

Atom's starting position

Atoms leave the effusion oven at 450 °C at the rate of 10^{11} atoms/s. By the time the slowing laser beams are switched on at $t = 0$, some atoms have left the oven and are already moving between the nozzle ($z = 0$) and the MOT position ($z = 33$ cm); more atoms are coming out of the oven at $z = 0$ at any time $0 < t < t_s$, where t_s is the total slowing time. We assume the slowing laser beams are switched off at $t = t_s$.

We assume the atomic flux to be uniform across the oven aperture, which has a diameter of 4 mm. The initial position of each atom is $(x_0, y_0, 0)$. To uniformly sample the transverse coordinates (x_0, y_0) from anywhere within the circular oven aperture with radius r_o , we first sample a random angle $\phi \sim U[0, 2\pi]$ from a uniform

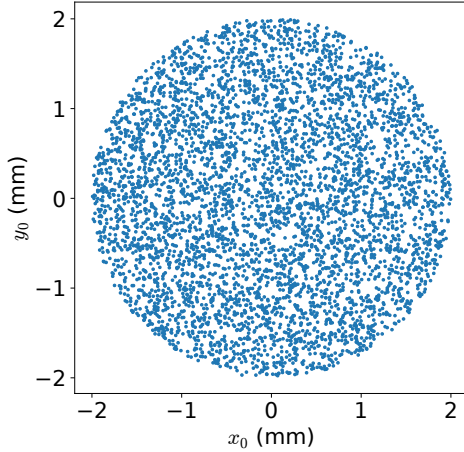


Figure 3.6: Initial transverse positions (x_0, y_0) of 5,000 atoms uniformly spaced within the oven aperture with radius $r_o = 2$ mm.

distribution. To place an atom between $0 \leq r \leq r_o$, we apply the inverse transform sampling method to sample r . For atoms to be uniformly distributed within a circle radius $0 \leq r \leq r_o$, the cumulative distribution function (CDF) is given by the area of the circle divided by the total area πr_o^2 , $F_R(r) = \Pr(R \leq r) = (r/r_o)^2$. This CDF has an inverse and is monotonically increasing, so we can sample R by computing $R = F^{-1}(u) = r_o\sqrt{u}$ where u is a uniform random number $u \sim U[0, 1]$. Hence, the transverse coordinates of each atom become $(x_0, y_0) = R(\cos \phi, \sin \phi) = r_o\sqrt{u}(\cos \phi, \sin \phi)$. Figure 3.6 shows a scatter plot of 5,000 transverse positions (x_0, y_0) , uniformly spaced within a circle of radius $r_o = 2$ mm. Each atom that exits the oven between $0 \leq t < t_s$ (while the slowing beams are on) starts at the initial position $(x_0, y_0, 0)$. We also sample a random exit time from the uniform distribution $\sim U[0, t_s]$ at which the atom starts experiencing the slowing force.

Our simulation also includes those atoms that left the oven before the slowing laser beams were turned on. We describe the sampling procedure here. Since the average speed from the effusion velocity distribution (Eq.(3.4)) is ≈ 350 m/s, faster atoms from the distribution take less than 1 ms to reach the MOT region. Many slow atoms take longer, but according to a sample of 20,000 atoms, over 99.9% of atoms

reach the MOT region ($z = 33$ cm) within ≈ 6 ms. To ensure we include as many relevant atoms as possible, we include all atoms that exit the oven, at $(x_0, y_0, 0)$, at any time between $-10 \text{ ms} < t < 0$ (before the slowing beams are switched on) and compute their final positions (x, y, z) at $t = 0$. We keep all atoms that remain in the slowing region $0 < z < 33$ cm for the stimulated slowing calculation and ignore the rest. The atoms that remain do not experience any slowing force before the slowing laser beams are turned on but are still subject to gravity. However, gravity causes a vertical displacement of only $\approx 10 \mu\text{m}$ over the slowing time of a few ms (assuming initial $\langle v_y \rangle = 0$).

MOT's capture velocity

As the atoms approach the 556 nm MOT, located 33 cm away from the oven aperture, only atoms that are slower than the MOT's capture velocity can be trapped. To estimate the MOT's capture velocity v_c and capture radius R_c , we use the 556 nm MOT parameters from [20]: the MOT detuning $\delta_{MOT} = -4.6 \text{ MHz}$ and the axial magnetic field gradient $\partial B / \partial z = 3.4 \text{ G/cm}$.

The MOT's capture radius R_c is the distance from the center of the MOT, where a stationary atom is in resonance with the MOT laser beams, which are detuned by δ_{MOT} from the atomic resonance. At this distance R_c , the atom at rest is subject to a Zeeman shift $-g\mu_B \partial B / \partial z R_c$ from the resonance. Equating the Zeeman shift to the laser detuning gives an expression for R_c :

$$R_c = \frac{\hbar \delta_{MOT}}{-g\mu_B \frac{\partial B}{\partial z}} \approx 0.65 \text{ cm} \quad (3.7)$$

The maximum capture velocity v_c of a MOT can be estimated from R_c and the spontaneous radiative force F_{sp} . Using a beam intensity of at least $I = 100I_{sat}$ ($I_{sat} = 0.136 \text{ mW/cm}^2$ for this 556 nm transition) in each of the three MOT beams ensures that we saturate the force $F_{sp} \approx \hbar k \gamma / 2$ where $\gamma = 2\pi \times 182 \text{ kHz}$. We assume that an atom with mass m and velocity v_c can be slowed down to zero velocity over

the distance R_c , and we estimate the capture velocity to be

$$v_c = \sqrt{\frac{2R_c F_{sp}}{m}} \approx 5 \text{ m/s} \quad (3.8)$$

Laser beam profile

Our simulation for the stimulated slowing beams takes into account the laser's transverse Gaussian beam profile, which causes a spatial variation in laser intensity and hence in the Rabi frequency Ω . We assume the laser beam waist radius w to be in the few mm range, which results in the Rayleigh range $z_R = (\pi w^2 n)/\lambda$ of at least 20 m. Because the atoms travel over a distance (33 cm) much smaller than z_R , the laser beam divergence is negligible and the beam waist radius w is assumed to be constant. Hence, the Rabi frequency Ω decreases exponentially with the atom's radial distance $r = \sqrt{x^2 + y^2}$ from the beam axis:

$$\Omega(r) = \Omega_0 \exp(-r^2/w^2) \quad (3.9)$$

We calculate Ω every time we update the atom's position (x, y, z) before we compute the force on the atom in the next simulation cycle. While the Rabi frequency Ω depends on the atom's position, the modulation frequency δ in the bichromatic slowing beams remains unchanged. This means that the Ω/δ ratio, and hence the bichromatic force profile, vary drastically depending on how far the atom is from the beam axis relative to the beam waist w . We show in Sec.3.3 how the Gaussian beam profile significantly impacts the slowing and trapping efficiency.

Uncertainty in the MOT loading rate

The goal of the Monte Carlo simulation is to estimate the number of atoms that can be slowed and trapped by the MOT. We assume all atoms are independent; therefore, the MOT loading rate from the total of N atoms follows the binomial distribution $B(N, p)$. Here \hat{p} denotes the probability of each atom being trapped. Each Monte Carlo simulation run, which includes N atoms, gives an estimate \hat{p} for this binomial

probability. The variance of the estimator \hat{p} is given by

$$\text{Var}(\hat{p}) = \frac{\hat{p}(1 - \hat{p})}{N} \quad (3.10)$$

From this variance, we can calculate the Wald-type 95% confidence interval [119] for \hat{p}

$$\hat{p} \pm \sigma_{95\%} = \hat{p} \pm 1.96 \sqrt{\frac{\hat{p}(1 - \hat{p})}{N}} \quad (3.11)$$

From our preliminary results with $\hat{p} \approx 0.005$ (0.5% of all atoms are trapped), we find that to keep the uncertainty $\sigma_{95\%} \leq 0.001$, we would need

$$\sigma_{95\%} = 1.96 \sqrt{\frac{\hat{p}(1 - \hat{p})}{N}} \leq 0.001 \quad (3.12)$$

$$N \geq \frac{1.96^2 \hat{p}(1 - \hat{p})}{0.001^2} = 17,000 \quad (3.13)$$

Hence, we use $N \approx 20,000$ atoms per simulation to keep the uncertainty in the loading rate on the order of 0.001 or smaller.

Spontaneous emission

We have estimated the effects of momentum diffusion due to spontaneous emission. Due to the relatively long lifetime of the 3P_1 state (874 ns), Monte Carlo simulations estimate that an atom in resonance with the bichromatic light fields undergoes up to 49,000 stimulated and 1600 spontaneous emissions in the course of 3 ms. With the recoil velocity of 4 mm/s/photon, we estimate the random diffusion velocity to be ≈ 16 cm/s, which is negligible for this system. These effects are even smaller when atoms are driven by square wave amplitude-modulated light (Chapter 4). In that case, the number of spontaneous emissions is reduced by 33% and the estimated random diffusion velocity decreases to 13 cm/s. The heating effects from momentum diffusion would be more prominent for atoms with shorter lifetimes. For the 556 nm transition in Yb, we can neglect these effects and focused our efforts on achieving a large velocity slowing range (e.g., 200 m/s) and optimizing the loading rate into the

MOT. We discuss several approaches below.

3.3 Chirped BCF

Chieda and Eyler demonstrated on He* atoms that laser frequency chirp can extend the velocity range of stimulated slowing without requiring a very large (greater than 250γ) bichromatic detuning δ [97]. The laser frequency was swept in a sawtooth manner to keep the laser detuning in resonance with the moving atoms while they are being slowed. This method can extend the slowing velocity range from a few 10 m/s to >200 m/s without requiring larger δ and larger Rabi frequency Ω . Although the time dependence of the chirp method does not capture all of the atoms, the method does reduce the power requirement and avoids the large δ, Ω regime where the bichromatic force reportedly vanishes [97].

To produce the maximal bichromatic force (BCF) profile centered at velocity v_d , the counter-propagating bichromatic light fields are at frequencies $\omega \pm \delta + k(v - v_d)$ in the rest frame of a moving atom with longitudinal velocity v whereas the co-propagating fields are at frequencies $\omega \pm \delta - k(v - v_d)$. To implement the laser frequency chirp method, the velocity detuning v_d in each of the four beams is swept from a high velocity in the 200 m/s range to a low velocity near the capture velocity ≈ 5 m/s every few ms. Figure 3.7 shows the velocity detuning v_d as a function of time. Here v_d is swept in a sawtooth manner from 240 to 10 m/s in 2 ms with 100% duty cycle. This chirp setting was used in the Monte Carlo simulation result shown in Fig.3.8b. To implement chirp in our model, the velocity detuning v_d is updated after every simulation cycle ($10 \mu s$).

Figure 3.8 shows the velocity distributions of atoms before (black dashed line) and after (red solid line) bichromatic slowing with and without laser frequency chirp. The Monte Carlo simulation results show that laser frequency chirp can significantly increase the slowing range and fraction of slow atoms below the MOT capture velocity 5 m/s. In Fig.3.8a, the laser detuning was fixed at a frequency offset corresponding to a Doppler velocity of 240 m/s. Even at $\delta = 200\gamma$ and $\Omega = 244\gamma$, the affected atoms were only slowed by a few 10 m/s range, and, not surprisingly, the number of atoms

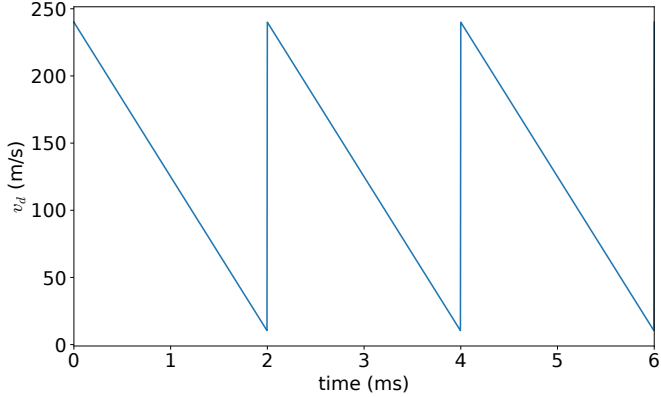


Figure 3.7: Velocity detuning v_d swept from 240 m/s to 10 m/s with a period of 2 ms and 100% duty cycle.

near zero velocity remained unchanged. In contrast, sweeping the detuning from 240 to 10 m/s in 2 ms substantially broadened the slowing velocity range and increased the population of atoms with velocities below the capture velocity of 5 m/s by at least four orders of magnitude. This result demonstrates that the laser frequency chirp method is an effective method to load the MOT. Our simulations also enabled us to investigate how other experimental conditions, such as the laser beam profile, affect the MOT loading rate.

As Fig.3.8b and 3.8c show, with stimulated slowing, the realistic laser Gaussian beam profile reduces the MOT loading rate relative to an unrealistic uniform intensity profile. Because the stimulated force is strongly dependent on the Ω/δ ratio and the Rabi frequency Ω rapidly decays with the atoms' distance from the beam axis, only atoms near the center of the beam experience a significant force and are slowed to the target capture velocity. In this particular example, the MOT loading rate was roughly five times smaller when using the Gaussian beam profile (Fig.3.8b) than it was when using the flat-top beam profile (Fig.3.8c), in which the Rabi frequency Ω remains constant and optimized across the beam area. Both simulations used the same chirped detuning (from 240 to 10 m/s), the same laser power, and the same beam diameter of 8 mm, which was twice as large as the oven aperture diameter of 4 mm, to compensate for the atomic beam divergence and maximize the number

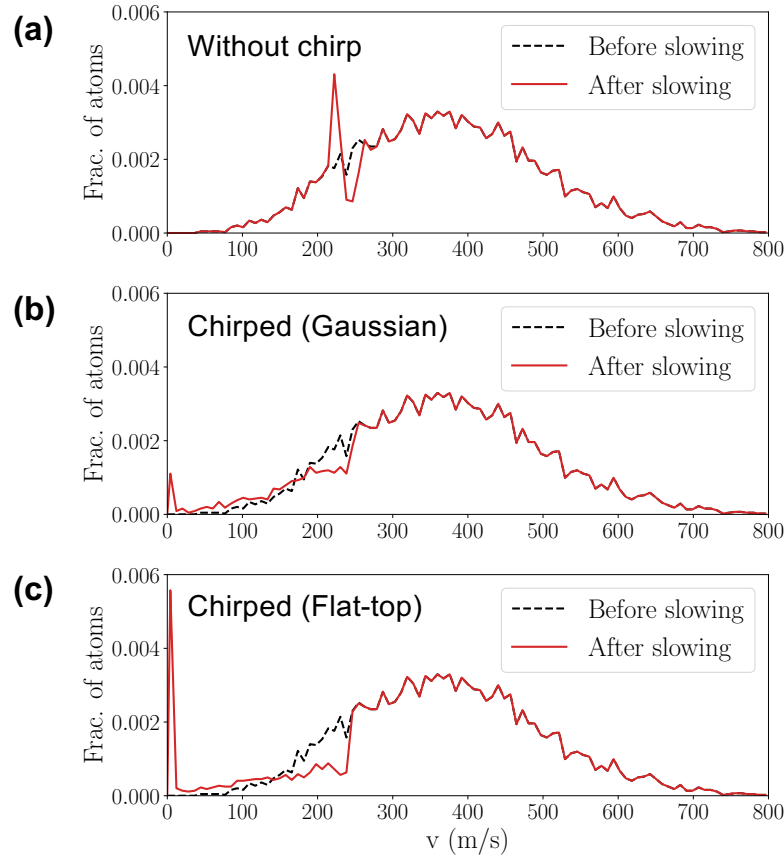


Figure 3.8: Velocity distributions before (black dashed line) and after (red solid line) slowing with (a) a fixed detuning at 240 m/s and (b) chirped detuning from 240 to 10 m/s in 2 ms. Gaussian beam diameter of 8 mm, $\delta = 200\gamma$ and peak Rabi frequency $\Omega = 244\gamma$ for both (a) and (b). (c) Same chirp parameters and laser power as (b) but with a flat-top beam profile of the same diameter. Rabi frequency $\Omega = 173\gamma$ is constant across the beam profile and δ was adjusted to 141γ . The unrealistic assumption of a flat-top beam profile overestimated the MOT loading rate. It is important to take into account the actual Gaussian beam profile.

of atoms slowed. In addition to the laser power, these geometric constraints of the experimental hardware must be taken into account to optimize the loading rate into the MOT.

To optimize the slowing force on atoms and the MOT loading rate, we kept the Ω/δ ratio at $\sqrt{3/2}$ at the center of the Gaussian beam. The Rabi frequency Ω is proportional to the square root of the laser intensity. Therefore, δ , Ω , and hence the stimulated force, are limited by laser intensity. For a fixed laser power, there is a trade-off between laser intensity, which sets the magnitude of the slowing force, and laser beam size, which determines the area across the laser beam profile where the force is present. Chirp parameters including the chirped detuning range and chirp period also play a role. A high laser intensity and large force allow a higher chirp rate, which means the starting detuning can be set to a higher velocity to slow a larger fraction of atoms that follow the effusion velocity distribution $f(v) \propto v^3 \exp(-mv^2/k_B T)$ (Eq.(3.4)). Therefore, the fraction of atoms in the atomic beam that will be slowed is strongly dependent on the choice of chirp parameters as well as on δ , Ω and the laser Gaussian beam diameter.

Under realistic experimental constraints including the Gaussian beam profile and total laser power of 1 W distributed equally between the stimulated slowing beams, we determined δ , Ω , and chirp parameters that optimized the loading rate of atoms into a 556 nm MOT. Figure 3.9 shows some of the best results predicted by our Monte Carlo simulations of over 20,000 atoms, using three different chirp settings: 140 → 10 m/s in 1.5 ms (square, solid line), 180 → 10 m/s in 2 ms (circle, dashed line), and 240 → 10 m/s in 2.5 ms (triangle, dot-dashed line). The error bars shown on the plot represent the 95% binomial confidence intervals. We found that the optimal settings for bichromatic slowing of Yb for the optical power limit of 1 W were $\delta = 105\gamma$, $\Omega = 129\gamma$, with a Gaussian beam 1/e diameter of 7.6 mm and a laser detuning chirp from 180 to 10 m/s in 2 ms. With these settings, up to $0.24 \pm 0.03\%$ of the total atomic flux from the oven can be trapped by the 556 nm MOT with 2 cm diameter located 33 cm away from the oven aperture. Here we assume the MOT beams are retroreflected and have a peak intensity of about 20 times the saturation intensity of the 556 nm transition, corresponding to a total power of <50 mW for the MOT.

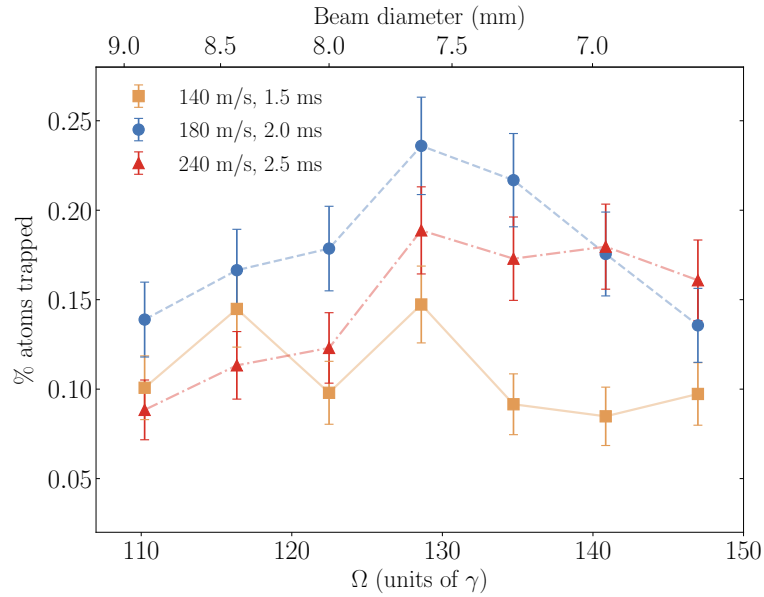


Figure 3.9: Percentage of atoms in the atomic beam that can be trapped by the 556 nm MOT after bichromatic slowing plotted against Rabi frequency Ω and laser beam diameter for three different chirp settings: $140 \rightarrow 10$ m/s in 1.5 ms (square, solid line), $180 \rightarrow 10$ m/s in 2 ms (circle, dashed line), and $240 \rightarrow 10$ m/s in 2.5 ms (triangle, dot-dashed line). The error bars represent 95% confidence interval. Up to 0.24% of atoms can be trapped using $\delta = 105\gamma$, $\Omega = 129\gamma$ with a Gaussian beam 1/e diameter of 7.6 mm and a laser detuning chirp from 180 to 10 m/s in 2 ms.

Assuming an atomic flux of 10^{11} atoms/s leaving the oven (as observed experimentally), the predicted loading rate of 0.24% is equivalent to 2.4×10^8 atoms/s. This predicted MOT loading rate using the chirped bichromatic slowing method is comparable to the 556 nm MOT loading rate achieved using a conventional 399 nm Zeeman slower [20]. We were encouraged by results by Kawasaki et al. who showed that loading Yb directly into a 556 nm MOT without first-stage cooling was also possible, but the loading rates were low (under 10^4 atoms per second) [74]. Our simulation results so far have shown that bichromatic slowing with the 556 nm laser may be able to replace a 399 nm Zeeman slower in loading Yb atoms into the MOT. We also explored different approaches to improve this stimulated slowing method including broadband cooling and polychromatic forces, which are discussed in the next chapter. We show in Chapter 4 that a square wave amplitude modulation can produce a polychromatic stimulated force that improves the MOT loading rate even further.

3.4 Broadband cooling

Various broadband cooling techniques have proven useful in some cases of Doppler cooling [120, 121, 122, 123, 124]. While laser cooling in general requires single-frequency, near-resonant laser beams to compress the atoms' velocity distribution, the monochromatic light has cooling effects only on atoms that are kept in resonance throughout the cooling stage. Alternatively, using multi-frequency light ensures that there are always atoms in resonance with at least part of the broad spectrum [125, 126, 127]. In our bichromatic slowing model, we investigated a broadband cooling approach by adding bichromatic light fields at different velocity detunings v_d to broaden the velocity range of the BCF and enhance the MOT loading rate.

So far, we have set the velocity detuning v_d in each of the bichromatic beams to slow atoms with velocities v in the range $v_d \pm \delta/4k$. In Fig. 3.3, v_d was set to zero to generate force-velocity profiles centered at the atom's velocity of $v = 0$. Recall that, in the rest frame of an atom traveling along the z-direction at velocity v , the bichromatic beams consist of the total of four frequencies $\omega \pm \delta \pm k(v - v_d)$, as shown in Fig.3.9a. To implement the broadband cooling method, we added a second set of bichromatic

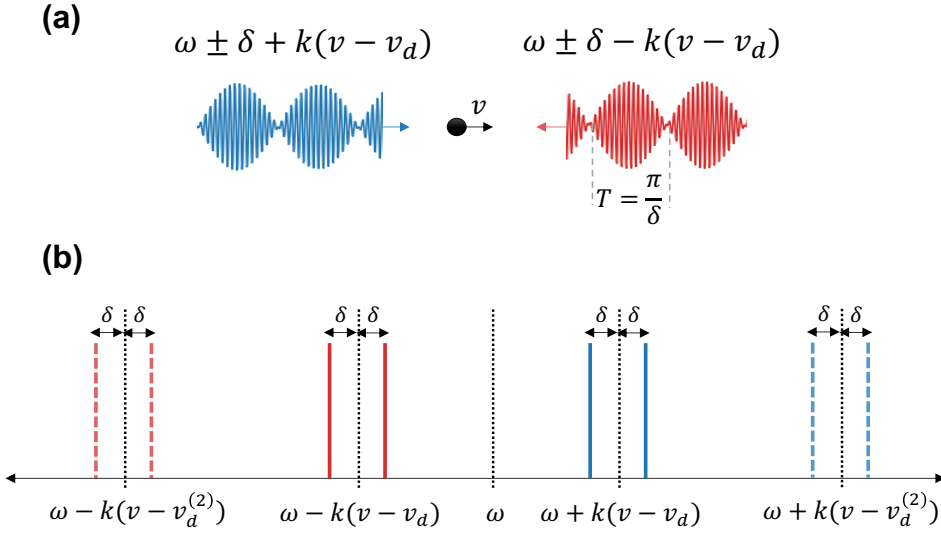


Figure 3.10: (a) An atom traveling at velocity v in co-propagating and counter-propagating bichromatic light fields, which are detuned to slow atoms with velocities v_d . (b) Eight frequencies are present in the broadband cooling setup with two sets of bichromatic light fields at two different velocity detunings v_d (solid) and $v_d^{(2)}$ (dashed). The colors represent the beams' propagating directions: counter-propagating (red) and co-propagating (blue), as in (a).

beams at a different velocity detuning $v_d^{(2)} \neq v_d$, i.e., at frequencies $\omega \pm \delta \pm k(v - v_d^{(2)})$, in the co-propagating and counter-propagating directions with respect to the atom. Using the same δ in both sets of the bichromatic fields, we expected to produce two identical bichromatic force-velocity profiles, which are centered at $v = v_d$ and $v = v_d^{(2)}$. Note that we still assume the phase difference $\chi = \pi/4$ between the counter- and co-propagating beams for both sets of the bichromatic light fields. Figure 3.10b show all eight frequencies present in the two sets of the bichromatic beams. The solid (dashed) lines represent the first (second) set of the bichromatic beams with velocity detuning v_d ($v_d^{(2)}$). The red and blue colors represent the counter-propagating and co-propagating beams, respectively.

Figures 3.11a and 3.11b show the force-velocity plots produced by this broadband cooling scheme with two detunings. Setting $\delta = 100\gamma$, the blue line in both plots represents the original BCF profile (previously shown in Fig. 3.3) with the width

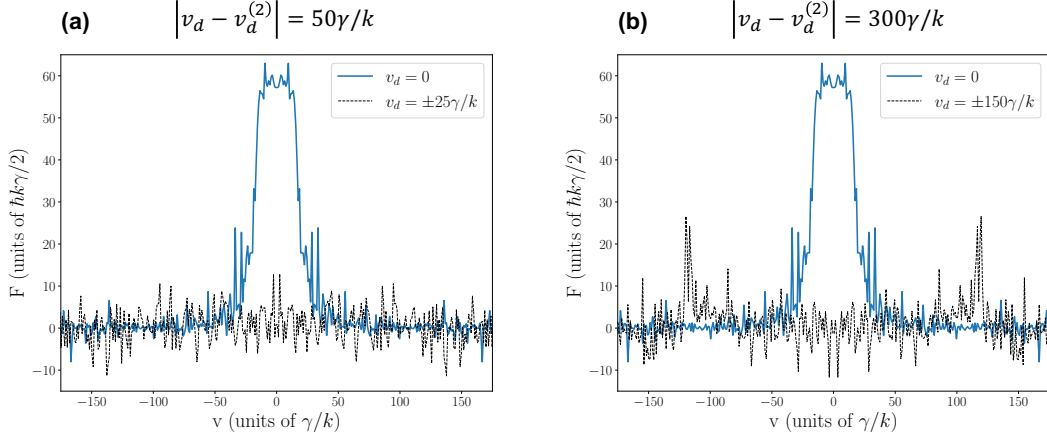


Figure 3.11: Bichromatic force-velocity plots centered at zero detuning $v_d = 0$ (blue, solid) and two velocity detunings at (a) $v_d = \pm\delta/4k = \pm 25\gamma/k$ (black, dashed), and (b) $v_d = \pm\delta/4k = \pm 25\gamma/k$ (black, dashed), $\delta = 100\gamma$ in both cases. Interference made the force vanish in (a), but some forces remained in (b), when the detuning difference exceeded $2\delta/k = 200\gamma/k$.

of $\approx \delta/2k = 50\gamma/k$. We thought that it would be possible to broaden the velocity range of the force by generating two identical force profiles next to each other, i.e., by centering the force profiles at $v_d = \pm 25\gamma/k$. However, as the dashed line in Fig. 3.11a shows, interference between the two sets of bichromatic light made the force vanish. This is true when the difference between two velocity detunings $|v_d - v_d^{(2)}| < 2\delta/k$. This threshold was estimated from contour plots of force, velocity, and detuning (an example of such plots is Fig. 3.12). As Fig. 3.11 shows, increasing the difference in the two velocity detunings $|v_d - v_d^{(2)}|$ from $50\gamma/k$ (a) to $300\gamma/k$ (b) can retrieve some stimulated forces. However, the two largest peaks that appear in Fig. 3.11b are still much smaller and narrower than the original, single force profile (blue curve). Therefore, this broadband cooling method improved neither the magnitude nor the velocity range of BCF.

To better visualize this parameter space of force, atom's velocity, and laser detunings, we plotted a contour plot in Fig. 3.12. In this broadband cooling setting, one velocity detuning was kept at $v_d = 100\gamma/k$ whereas the other detuning $v_d^{(2)}$ was varied between $150\gamma/k$ and $500\gamma/k$ (vertical axis). The color on the plot represents

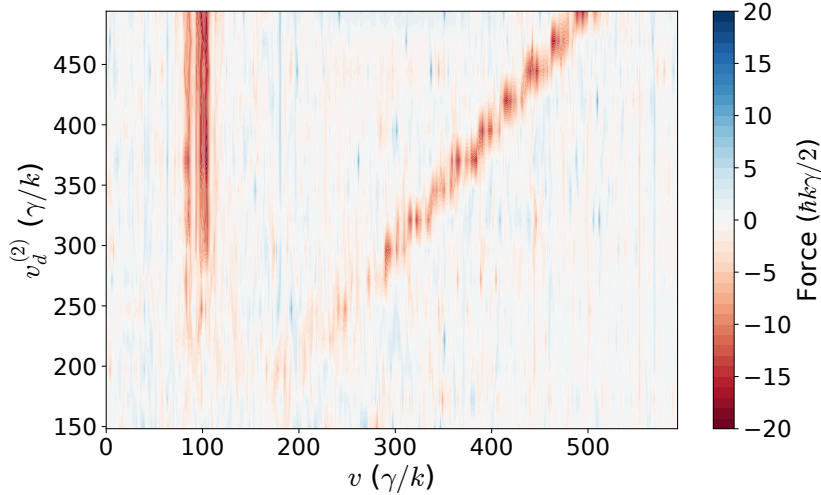


Figure 3.12: Contour plot of bichromatic force, atom’s velocity (horizontal axis), and second detuning (vertical axis). Darker red color represents a stronger (negative) slowing force.

the magnitude and sign of the force. A large decelerating (negative) force, which is favorable, is shown in darker red. Any horizontal cross-section of this contour plot is a force-velocity profile similar to those in Fig. 3.11, with prominent peaks located where the contour plot is dark red. For $v_d^{(2)} < 200\gamma/k$, meaning $|v_d - v_d^{(2)}| < 2\delta/k$, there is barely any dark red region in the contour plot, which means the force vanished. Increasing the second detuning to $200\gamma/k < v_d^{(2)} < 300\gamma/k$ retrieved some forces near $v = v_d = 100\gamma/k$ and $v = v_d^{(2)}$ but we would need $v_d^{(2)} \geq 300\gamma/k$ to clearly see two separate peaks at the two chosen detunings. However, the maximum magnitude of the force observed never exceeded $2F_{rad}$, which is smaller than the maximum BCF estimate $\hbar k \delta / \pi \approx 32F_{rad}$ for $\delta = 50\gamma$.

Contour plots of force, velocity, and detunings for different values of δ ’s show similar behavior as in Fig. 3.12. The bichromatic force vanishes when the detuning difference $|v_d - v_d^{(2)}|$ is less than $2\delta/k$, and some force is retrieved near v_d and $v_d^{(2)}$ when the velocity detunings are further apart. Note that the minimum detuning difference, $2\delta/k$, required to retrieve any force is greater than the width of an individual BCF profile of $\Delta v \approx \delta/2k$. This means that, at best, this broadband cooling method, with

two sets of bichromatic light fields tuned to slow two different velocity classes, can produce two separate force profiles but never a single, broadened stimulated force profile when applied to a simple two-level atom.

We also verified that it was not possible to produce optical molasses on a single two-level atom by combining two shifted bichromatic force profiles at the opposite phases $\chi = \pm\pi/4$. This is consistent with Partlow et al.'s findings [96] from their attempt to create the optical molasses force on He* atoms. To avoid interference, they had to apply the two force profiles on the atoms at two separate locations. On the other hand, as demonstrated by Wenz et al., in more complicated systems, such as diatomic and polyatomic radicals that can be represented by two coupled two-level systems, large molasses-like cooling forces can be realized using two separated BCF profiles [104]. This suggests that broadband cooling, which combines multiple BCF profiles of the same phase at different detunings, may be feasible in systems more complicated than a single two-level atom. So far, the most effective method we have found to extend the velocity range of the stimulated forces on two-level atoms is the laser frequency chirp method [97]. In Chapter 4, we show that using chirp and polychromatic forces together can improve the MOT loading rate even further.

Chapter 4

Stimulated Slowing with Polychromatic Forces

4.1 Introduction

Continuing from Chapter 3, which describes the theory and numerical model of the bichromatic stimulated force, this chapter provides details on how we modified our model to compute and investigate polychromatic stimulated forces produced by amplitude-modulated and phase-modulated light. We show in Sec.4.2 that square-wave amplitude modulation (square-wave AM) can produce strong slowing forces, which act over a broader velocity range than that of the BCF. We characterized and optimized this square-wave AM force, and then ran Monte Carlo simulations to estimate the MOT loading rate. With laser frequency chirp and when optimized, this square-wave AM stimulated force can achieve 70% higher MOT loading rate than the optimum BCF loading rate found in Sec.3.3. We discuss in Sec.4.3 the phase modulation method, which provides an alternative method to produce stimulated forces in the laboratory. This chapter concludes with a brief summary of our numerical model of the BCF and PCF.

4.2 Square wave amplitude modulation

Although the bichromatic force is already an effective method for stimulated slowing of Yb atoms, the stimulated force can be enhanced by adding higher harmonics of the bichromatic light [21]. Galica et al. presented numerical calculations of a four-color polychromatic force [21], which has a larger magnitude and broader velocity range than BCF, and is produced by adding the third harmonic of the bichromatic detuning δ to make the pulses narrower in time and more similar to separate π -pulses. Their results motivated us to investigate the use of square wave modulation and the effects of adding higher harmonics on stimulated forces on Yb.

4.2.1 Numerical model

Starting from the BCF model we developed (discussed in Chapter 3), we modified the Hamiltonian to describe square amplitude-modulated (AM) light. The cosine amplitude modulation terms in Eq.(3.1) are replaced by a square wave modulation at frequency δ_{sq} . The light fields now consist of two counter-propagating beams, each with Rabi frequency Ω , a square amplitude modulation at frequency δ_{sq} , and a phase difference χ between each beam. We investigated both near-ideal square waves produced by a built-in square wave function in the Scipy signal processing library and approximations from a truncated Fourier series of a square wave. The truncated square waves are more realistic for experiments because of the limited bandwidth of AM optical modulators. The Fourier series that contains n harmonics consists of odd harmonics $\pm\delta_{sq}, \pm 3\delta_{sq}, \pm 5\delta_{sq}, \dots, \pm(2n - 1)\delta_{sq}$ with decreasing amplitudes. For example, a square wave with only two harmonics ($n = 2$) has frequency components $\pm\delta_{sq}$ and $\pm 3\delta_{sq}$ with Rabi frequencies Ω and $\Omega/3$, respectively. Examples of these truncated square waves with $n = 2, 5, 5000$ are given in Fig. 4.1. One limitation of the square wave modulation is that we cannot specify the amplitudes or phases of different harmonics independently. We show later that this is not a problem provided we find the right Ω and χ .

Figure 4.2 illustrates how the envelopes of the co-propagating (blue) and counter-propagating (red) beams overlap in the time domain for the bichromatic and square

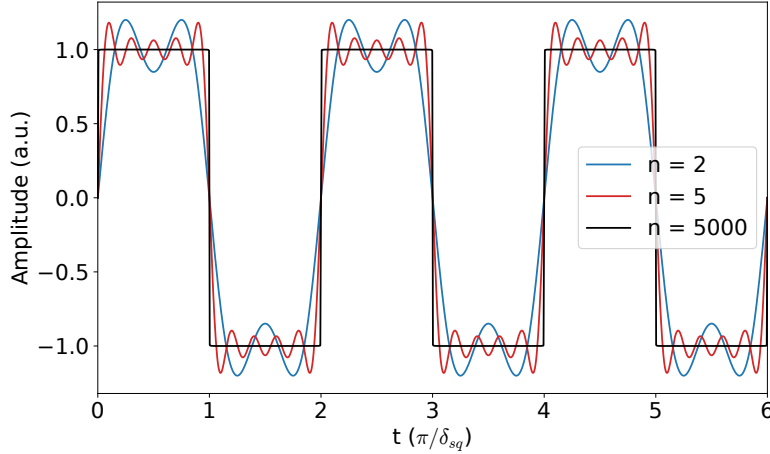


Figure 4.1: Square waves produced by the truncated Fourier series with $n = 2$ (blue), $n = 5$ (red), and $n = 5000$ harmonics of δ_{sq} .

wave settings. The relative phase χ determines the amount of overlap between the envelopes. In our model, choosing a positive $0 < \chi < \pi$ ensures that an atom absorbs a counter-propagating photon first. The later arrival of a co-propagating photon then triggers a stimulated emission; the atom slows down as it emits a photon in the direction the atom is moving in. Hence, $0 < \chi < \pi$ produces decelerating forces. The magnitude of χ , which defines the time between consecutive absorption and emission events, also plays a role. In the bichromatic case, $\chi = \pi/4$ optimizes the magnitude and velocity range of the BCF. On the other hand, we show in Sec.4.2.2 that $\chi = 0.36\pi \approx \pi/3$ optimizes the stimulated force in the square wave AM setting. The time-domain plots in Fig.4.2 show these optimal cases with $\chi = \pi/4$ in the bichromatic setting and $\chi = 0.36\pi$ in both square wave settings.

Previously in Sec.3.2.1, we applied the rotating wave approximation (RWA) to derive the Hamiltonian for a two-level atom in bichromatic light fields. Note that RWA still applies here. From the derivation in Sec.3.2.1, we considered an atom in the rotating frame at optical frequency $\omega = 2\pi \times 540$ THz, associated with the energy difference $\hbar\omega$ between the ground state 1S_0 and excited state 3P_1 , and dropped the fast oscillating terms $e^{\pm 2i\omega t}$ from the Hamiltonian. RWA requires that all other

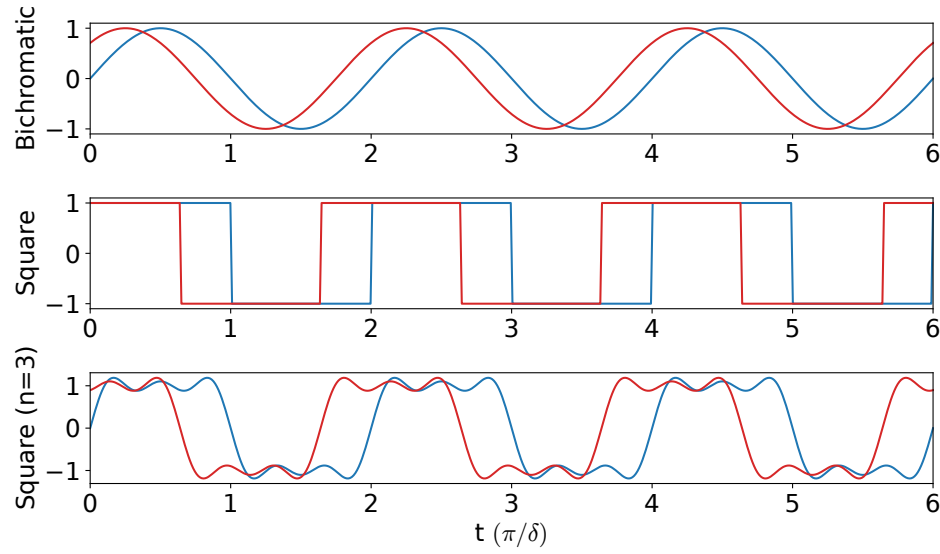


Figure 4.2: Envelopes of the co-propagating (blue) and counter-propagating (red) bichromatic beams (top), near-ideal square wave AM beams (center), and square wave AM with only the first $n = 3$ harmonics present (bottom). The amount of overlap between the counter-propagating (red) and the co-propagating (blue) envelopes in each case is defined by the relative phase χ . We set $\chi = \pi/4$ in the bichromatic case to optimize the BCF. For the two square wave cases shown here, $\chi = 0.36\pi \approx \pi/3$. Here the square wave modulation frequency $\delta_{sq} = \delta = 50\gamma$.

frequencies and detunings are much smaller than this ω . The Rabi frequency Ω used in our calculations never exceeded $\approx 200\gamma = 2\pi \times 36$ MHz $\ll \omega$. The modulation frequency δ_{sq} was also in the same regime as Ω , where $\Omega/\omega \approx \delta_{sq}/\omega < 10^{-8}$. For square wave amplitude-modulated light, we also need to consider the higher harmonics of δ_{sq} . The ratio $\delta_{sq}/\omega < 10^{-8}$ suggests that $10^5 \times \delta_{sq} \ll \omega$, which means that RWA still applies for at least the first 10^5 harmonics of δ_{sq} . In most of our calculations, the truncated Fourier series contains up to only the first $n = 5$ harmonics (up to $9\delta_{sq}$) so the detunings, including the velocity detuning of $kv_d < 2\pi \times 540$ MHz for $v_d < 300$ m/s, were still much smaller than ω . On the other hand, to produce sharp edges in near-ideal square waves requires a very large number of higher harmonics. Although, we did not know exactly how many harmonics were present in the Scipy square wave, the truncated Fourier series with n terms and the Scipy square wave started to converge when $n > 1000$. Fig. 4.1 shows that $n = 5000$ terms in the Fourier series produced near-ideal square waves with sharp edges (black). Given also that, in the Hamiltonian, the contribution from the m^{th} harmonic is only a factor of $1/m$ compared to the first harmonic, we assumed the very fast terms from $m > 10^5$ in the Scipy near-ideal square wave to be negligible.

With RWA applied, the 2×2 Hamiltonian still has zero diagonal elements and time-dependent off-diagonal elements $H_{01}^{sq}(t)$ and $H_{10}^{sq} = (H_{01}^{sq})^*$. These off-diagonal matrix elements contain either a truncated Fourier series of a square wave or a built-in square wave function from Scipy. Here χ still denotes the relative phase between counter- and co-propagating beams. Assuming again that the laser beams are tuned to slow atoms at velocity v_d , for an atom traveling at a longitudinal velocity v , H_{01}^{sq} with a truncated Fourier series is given by

$$\begin{aligned} H_{01}^{sq}(z, t) = & \Omega e^{-i[k(v-v_d)t+kz]} \sum_{i=1}^n \frac{4}{\pi(2i-1)} \sin((2i-1)(\delta_{sq} + \chi)) \\ & + \Omega e^{i[k(v-v_d)t+kz]} \sum_{j=1}^n \frac{4}{\pi(2j-1)} \sin((2j-1)\delta_{sq}) \end{aligned} \quad (4.1)$$

Similar to the steps described in Sec.3.2.1, we numerically solved the Linblad Master

equation (6.19), using the same collapse operator defined previously $C = \sqrt{\gamma}|0\rangle\langle 1|$, and calculated the force from $F(t) = \hbar\frac{\partial}{\partial z}\text{Tr}(\rho H^{sq})$.

4.2.2 Optimizing the force

To characterize and optimize this square polychromatic force (square PCF) computed from our model, we plotted this polychromatic force as a function of an atom's velocity v over a parameter space spanning a Rabi frequency range $0 \leq \Omega \leq 3\delta_{sq}$ and a phase range $0 \leq \chi \leq \pi$. Similar to those of the BCF, the magnitude and velocity range of the force are sensitive to both parameters Ω and χ . By inspecting the force-velocity profiles and computing the areas under the $F - v$ curves, we found that the Rabi frequency of $\Omega = \pi\delta_{sq}/4 \approx 0.8\delta_{sq}$ and the relative phase of $\chi = 0.36\pi \approx \pi/3$ optimized the magnitude and velocity range of the square PCF.

The contour plot in Fig. 4.3 demonstrates how the force-velocity profile varies with χ when the Rabi frequency Ω is fixed at the optimal value $\Omega = \pi\delta_{sq}/4 = 61\gamma$. The phase χ is shown in the units of π , ranging from 0 and $1/2$. With larger force shown in red, the plot indicates a region between $0.3\pi \leq \chi \leq 0.4\pi$ where a strong stimulated force is uniformly present over a broad velocity range of $\pm 25\gamma/k$. This width is almost twice the width at the peak of the optimal BCF force-velocity profile in Fig.3.3 for $\delta = 50\gamma$ and the same Rabi frequency $\Omega = 61\gamma$ (blue, lower line). For smaller values of χ , the velocity range of the square wave force splits into two narrow domains, and the force vanishes close to $\chi = 0$ and $\pi/2$. By calculating the area under the $F - v$ cross section for each χ , we verified that $\chi = 0.36\pi$ optimized the force magnitude and velocity range of the square PCF. This optimal phase remains the same regardless of the number of harmonics n present in the square wave, so we only display the $n = 3$ case in Fig.4.3.

The optimal Rabi frequency to produce the square PCF matches the π -pulse condition $\Omega = \pi\delta_{sq}/4$ described in [10, 16]. When this condition is fulfilled, the arrival of each pulse inverts the atomic population between the atom's ground and excited states. Counter-propagating pulse trains keep the atom cycling between the two states as it absorbs photons from one pulse train and re-emits them into the

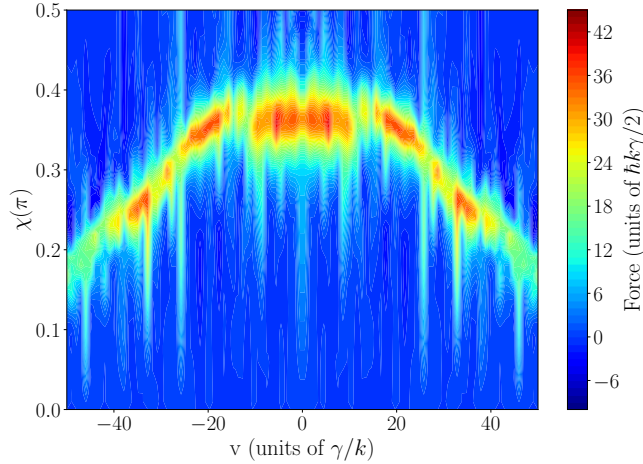


Figure 4.3: Stimulated force from an approximate square wave modulation with only the first three harmonics ($n = 3$) of δ_{sq} plotted in the parameter plane of the atom's velocity v and phase χ . $\Omega = \pi\delta_{sq}/4 = 61\gamma$, $\chi = 0.36\pi$ produce the strongest stimulated force with a magnitude of over $35F_{rad}$, which acts over a broad velocity range of over $\pm 25\gamma/k$.

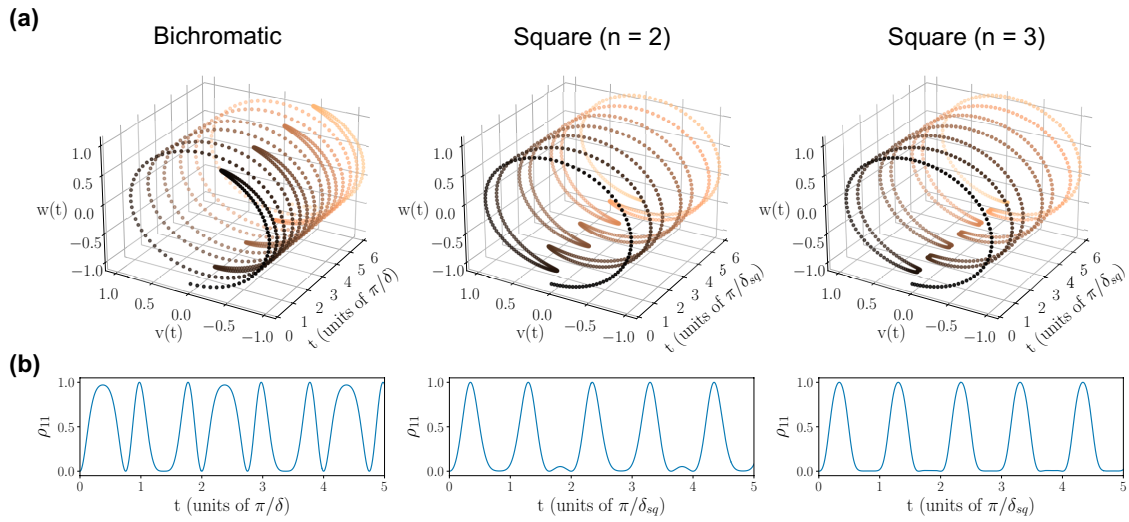


Figure 4.4: Time evolution of the Bloch vector (top row) and the excited-state population ρ_{11} (bottom row) for a two-level system in the optimal bichromatic (left) and square wave light fields with the first two harmonics (center), and three harmonics (right). The spacing between dots corresponds to the time interval of 0.4 ns.

other. We confirmed this finding at the optimal conditions $\Omega = \pi\delta_{sq}/4$, $\chi = 0.36\pi$ by plotting the Bloch vector of the two-level system as a function of time. The Rabi cylinder plots in Fig.4.4a show the time evolution of two components of the Bloch vector

$$\begin{aligned} v(t) &= i(\rho_{01} - \rho_{10}) \\ w(t) &= \rho_{11} - \rho_{00} \end{aligned}$$

for a two-level system without decay for the optimum BCF (left), and truncated square wave cases with only two (center) and three (right) harmonics n in the square wave Fourier series. The Bloch vector trajectory in the BCF case (left) shows symmetric wrapping around $w(t) = 0$ (note that our result is $\pi/2$ phase-shifted relative to Galica et al.'s result in [21]). Starting in the ground state, the Bloch vector rotates counterclockwise and approaches the excited state, at which it reverses direction, then returns to the ground state before rapidly completing a full clockwise rotation. The plot of excited-state population ρ_{11} as a function of time directly below the Bloch cylinder shows that the additional wrapping slows down the cycling between the ground and excited state. These BCF results draw a clear distinction between the bichromatic light fields and alternating π -pulses, which would produce a simple rotation of the Bloch vector without any wrapping.

On the other hand, the Bloch vector trajectories under the optimal square wave conditions are similar to the π -pulse-like periodic cycling between the ground and the excited state with minimal wrapping around the ground state. Figure 4.4b shows that on average, an atom spends less time in the excited state when driven by the optimal square wave light fields. This reduces the number of spontaneous decays by 33% compared to the number of spontaneous decays that occur in the BCF method, and hence decreases the heating effects from momentum diffusion. The center plot in Fig.4.4a with only two harmonics ($n = 2$) is very similar to the four-color force presented in [21], which also contains only the first and third harmonics of the bichromatic light fields. As Fig.4.4a shows, adding the 5th harmonic ($n = 3$) suppressed the wrapping around the ground state almost entirely. The excited-state population

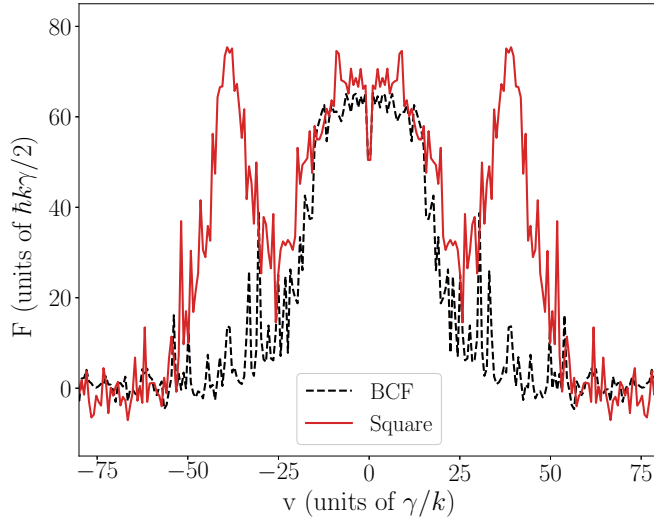


Figure 4.5: Force-velocity plots showing the BCF (dashed black line) and the square PCF from a near-ideal square wave (solid red line). $\Omega = 122\gamma$ for both cases. $\delta = 100\gamma$ in the BCF case to keep $\Omega/\delta = \sqrt{3}/2$ and $\chi = \pi/4$. For the square wave case, $\delta = 155\gamma$ and $\chi = 0.36\pi$ to optimize the force profile.

plot below for $n = 3$ shows a simple oscillation between the ground and excited state, which is more similar to the π -pulse behavior than the other two cases ($n = 2$ and bichromatic) are. When even higher harmonics are present, the Bloch vector simply reverses the direction at the ground state after each complete rotation, with virtually no wrapping at the ground state. Although the Bloch vector trajectories differ slightly for different number of harmonics n , we found that the force-velocity profile of the square wave force, shown as the solid curve in Fig.4.5, remained the same for all $n > 2$ for $\Omega = \pi\delta_{sq}/4$ and $\chi = 0.36\pi$. Note that both the strong force and the population inversion disappear if we remove the third and any other higher harmonics and revert to a sinusoidal modulation ($n = 1$) under the same conditions.

4.2.3 Optimum square PCF profile

Figure 4.5 plots the bichromatic force and polychromatic force (produced by the same Ω and optical power) as a function of an atom's velocity v . The plot shows that

the square wave modulation enhances the velocity range of the force. The square PCF (red solid curve), generated using the near-ideal square wave, which consists of a large number of harmonics, has a maximum magnitude comparable to that of the BCF of the same optical power (black dashed curve). The square PCF profile also contains three prominent broad peaks instead of one. The two side peaks are symmetrical around the center ($v_d = 0$) with about half the width of the central peak, which makes the total width of the square PCF profile roughly twice that of the BCF profile. As previously stated, the square wave force profile did not change significantly with the number of harmonics n present. The $n = 2$ force profile overlapped almost perfectly the force profile shown in Fig.4.5, which was generated by the sharp-edge square wave function from the Scipy library.

4.2.4 Estimating the MOT loading rate

After characterizing and optimizing the square wave force profile, we ran Monte Carlo simulations to predict and optimize the MOT loading rate. We applied the laser frequency chirp method, as described earlier in Sec. 3.3, to maximize the slowing velocity range. The velocity detuning v_d in each of the two counter-propagating beams was swept in a sawtooth manner every few ms to stay in resonance with atoms as they are being slowed from over 200 m/s to 10 m/s. Note that the laser frequency chirp was applied separately from the square wave amplitude modulation. The modulation frequency δ_{sq} remained constant to satisfy the condition $\Omega = \pi\delta_{sq}/4$ while at the same time the velocity detunings v_d was swept in a sawtooth manner. Using the total optical power of 1 W and optimal Rabi frequency, laser frequency chirp velocity range, chirp rate, and Gaussian beam size, we found that up to $0.40 \pm 0.05\%$ of Yb atoms in the atomic beam can be trapped by the 556 nm MOT after being slowed by the square wave stimulated force. Figure 4.6 shows the predicted loading rate as a function of Rabi frequency Ω and beam diameter for three different chirp settings: 220 → 10 m/s in 2 ms (square, solid line), 240 → 10 m/s in 2.5 ms (circle, dashed line), 260 → 10 m/s in 3 ms (triangle, dot-dashed line). The optimal conditions favor a larger 1/e Gaussian laser beam diameter of 11 mm compared with the BCF preferred

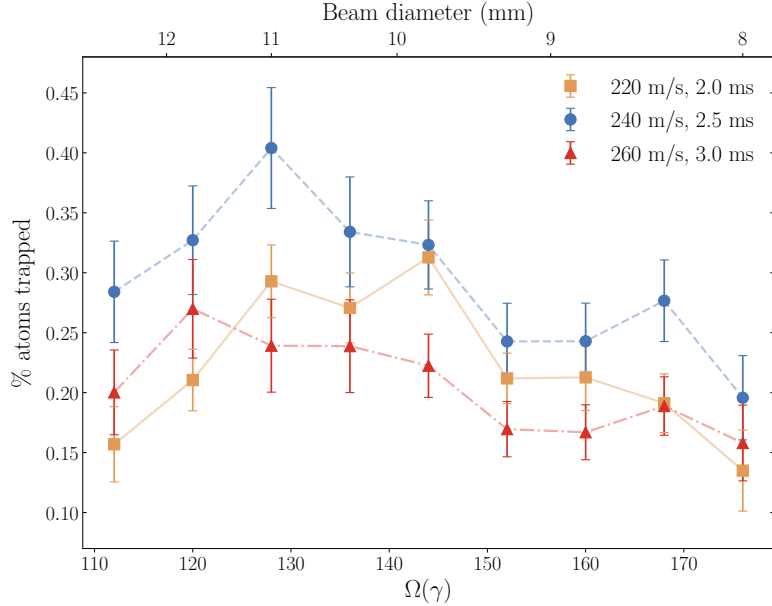


Figure 4.6: Percentage of atoms in the atomic beam that can be trapped by the 556 nm MOT after slowing with the square wave stimulated force plotted against Rabi frequency Ω and laser beam diameter for three different chirp settings: 220 → 10 m/s in 2 ms (square, solid line), 240 → 10 m/s in 2.5 ms (circle, dashed line), 260 → 10 m/s in 3 ms (triangle, dot-dashed line). Up to 0.40% of atoms can be trapped using $\delta_{sq} = 160\gamma$, $\Omega = 128\gamma$ with a Gaussian beam 1/e diameter of 11 mm, total laser power of 1 W, a slowing distance of 33 cm, and a laser detuning chirp from 240 to 10 m/s in 2.5 ms.

beam diameter of 7.6 mm. Given that our atomic beam has a diameter of only 4 mm, this result highlights the pronounced effects of the Rabi frequency variation in the Gaussian beam on the stimulated force produced by a square wave modulation. Using laser beams with a larger diameter can slow atoms more effectively because the Rabi frequency Ω varies more slowly across the beam area. This ensures that the ratio Ω/δ_{sq} (Ω/δ) remains optimal to maximize the square PCF (BCF) across a larger area in the atomic beam.

Compared to the optimal chirped BCF method, which can produce the MOT loading rate of 2.4×10^8 atoms/s, our simulation predicts that the square wave method can enhance the loading rate by 70% (4.0×10^8 atoms/s) when the same laser power

and a larger Gaussian beam diameter are used. For the square wave method, we have assumed that electro-optic modulators can produce the square wave amplitude modulation on the two counter-propagating beams at the desired modulation frequency around $\delta_{sq} = 160\gamma \approx 2\pi \times 29$ MHz without loss of any optical power, as opposed to splitting the laser beam into multiple laser beams and overlapping the different harmonics. This assumption allowed us to use larger beam sizes in the square wave case, in which 1 W of laser power was split evenly between two beams instead of four beams as is done in the BCF case. We have shown that both the square wave and BCF methods can produce a loading rate on the order of 10^8 atoms/s with only one 556 nm laser. The MOT loading rate might be improved further if one modifies the laser beam profile from Gaussian to flat-top over the slowing distance between the oven aperture and the MOT. This is difficult in our experiment due to the long slowing distance of 33 cm.

4.3 Phase modulation

Both the bichromatic and polychromatic stimulated slowing methods presented so far utilize counter-propagating amplitude-modulated (AM) light to induce a series of stimulated emissions in atoms. We discuss here a different approach, which uses phase-modulated (PM) light.

The setup consists of two CW beams traveling in the $+z$ and $-z$ directions. Let ε_{red} and ε_{blue} define the electric fields of the counter-propagating beam and the co-propagating beam, respectively. As done in our previous derivations, the counter-propagating field ε_{red} is red-detuned by $-kv_d$ whereas the co-propagating field ε_{blue} is blue-detuned by $+kv_d$. Taken into account Doppler shifts $\pm kv$ experienced by a moving atom with velocity v along the z -direction, the phase-modulated ε_{red} and

ε_{blue} can be represented by the following expressions:

$$\varepsilon_{red} = E_0 \cos [(\omega + k(v - v_d))t + kz + \phi_{red}] \quad (4.2)$$

$$= E_0 e^{i\phi_{red}} e^{i[(\omega+k(v-v_d))t+kz]} + c.c. \quad (4.3)$$

$$\varepsilon_{blue} = E_0 \cos [(\omega - k(v - v_d))t - kz + \phi_{blue}] \quad (4.4)$$

$$= E_0 e^{i\phi_{blue}} e^{i[(\omega-k(v-v_d))t-kz]} + c.c. \quad (4.5)$$

Here $\phi_{red}(t)$ and $\phi_{blue}(t)$ are time-dependent phase modulation functions. Motivated by the promising results from the square AM light, described in Sec.4.2, we first investigated a square wave phase modulation (square wave PM). In this setting, $\phi_{red}(t)$ and $\phi_{blue}(t)$ are square waves oscillating between 0 and $\pm\pi$ at a phase modulation frequency δ_ϕ . The relative phase χ , which has a fixed value, sets the offset between the phase switching in the red- and blue-detuned fields. We observe from the complex forms of ε_{red} and ε_{blue} (Eq. 2.3 and 2.5) that each electric field is made up of a time-dependent complex amplitude $E_0 e^{i\phi(t)}$ multiplied by a traveling plane wave $e^{i[(\omega \pm k(v - v_d))t \pm kz]}$. As Fig.4.7 shows, with the square wave PM, the real part of the time-dependent amplitude $\text{Re}(E_0 e^{i\phi(t)}) = E_0 \cos \phi$ is a square wave oscillating between E_0 and $-E_0$. Hence, with the right choice of parameters, it seemed we should be able to produce similar stimulated forces from the square wave PM. Figure 4.8, on the other hand, shows similar plots for a sine-wave phase modulation. ϕ_{red} and ϕ_{blue} in this case were sinusoidal functions oscillating between 0 and $\pm\pi$ with a phase shift of $\chi = \pi/4$ between them. In this case, the $E_0 \cos \phi$ waveform is not sinusoidal.

From the electric field expressions, we derived the time-dependent Hamiltonian and solved the Linblad Master Equation numerically for the density matrix $\rho(t)$ before calculating the stimulated forces. This is similar to what we did earlier with the square AM setting. With our model, we verified that a square wave PM can produce an identical stimulated force-velocity profile (solid curve in Fig.4.9) to the square wave AM force profile shown in Fig.4.5, provided the phase modulation frequency δ_ϕ and Rabi frequency Ω satisfy $\Omega = \pi\delta_\phi/4$ and the relative phase between the two counter-propagating beams is fixed at $\chi = 0.36\pi$. This result suggests that it is possible to replace amplitude modulators by phase modulators in a stimulated slowing

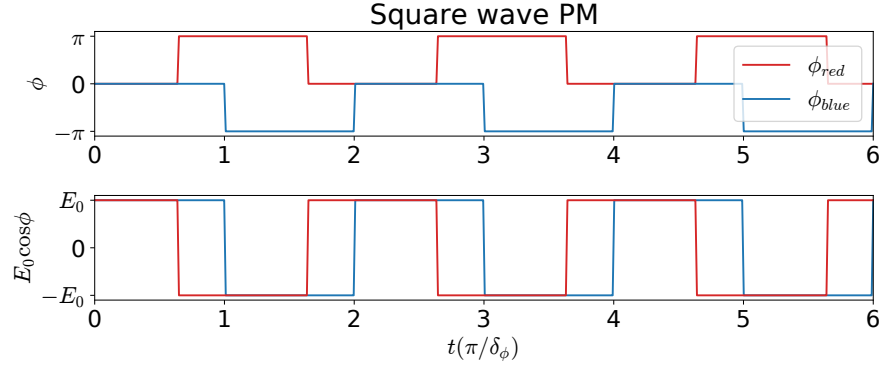


Figure 4.7: (Top) Square-wave phase modulation functions ϕ_{red} and ϕ_{blue} at modulation frequency δ_ϕ . Note the opposite signs and the phase shift $\chi = 0.36\pi \approx \pi/3$ between the two. (Bottom) Real part of the complex electric field amplitude $E_0 e^{i\phi(t)}$, which resembles the square AM envelope in Fig.4.2.

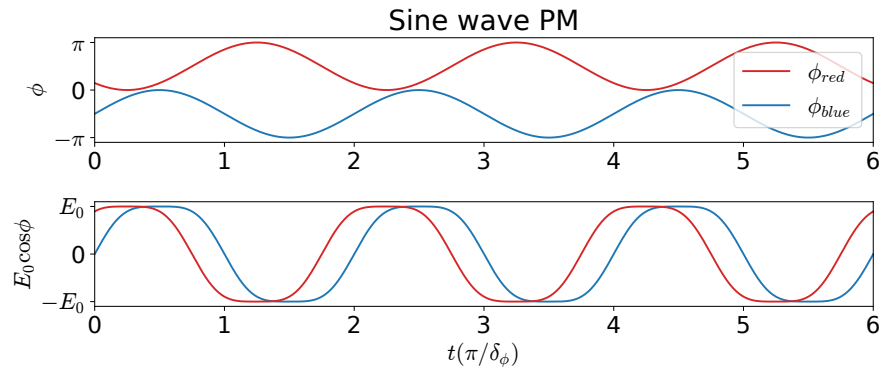


Figure 4.8: (Top) Sine-wave phase modulation functions ϕ_{red} and ϕ_{blue} at modulation frequency δ_ϕ . Note the opposite signs and the phase shift $\chi = \pi/4$ between the two. (Bottom) Real part of the complex electric field amplitude $E_0 e^{i\phi(t)}$.

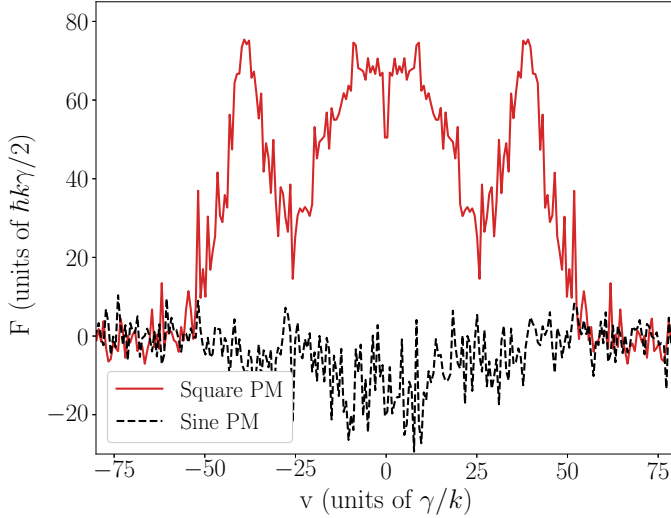


Figure 4.9: Force-velocity plots for square wave phase modulation function (solid) and sinusoidal phase modulation function (dashed). $\delta_\phi = 153\gamma$, $\Omega = 122\gamma$, and $\chi = 0.36\pi$ in both cases.

experiment to produce the same force as that produced by a square wave AM. As with the square wave AM, replacing the near-ideal square wave function with a truncated Fourier series did not alter the force-velocity profile shown in Fig.4.9.

We then tried replacing the square wave modulation with a sinusoidal phase modulation (sine PM) while keeping $\pi\delta_\phi/4$ and $\chi = 0.36\pi$. As shown in Fig.4.9, the force (dashed curve) almost vanishes and no longer looks symmetrical about zero velocity. In the time domain, other than the larger wrapping of the Bloch vector near the ground state, we did not identify any striking features that could explain this asymmetry in the force-velocity profile. We also tried searching the parameter space of Ω/δ_ϕ and χ to identify optimizing conditions for the sinusoidal PM setting, but we did not find any conditions under which the sinusoidal phase modulation can improve the stimulated force beyond the bichromatic force or the square-wave polychromatic force.

4.4 Conclusion

We developed a numerical model and Monte Carlo simulations to analyze bichromatic (Chapter 3) and polychromatic stimulated forces (this chapter) for the slowing of Yb atoms under realistic experimental conditions. We have shown theoretically that it is possible to cool and trap Yb atoms on the narrow 3P_1 transition and achieve a MOT loading rate on the order of 10^8 atoms/s using the total laser power of 1 W (Rabi frequency Ω near 25 MHz).

The square wave modulation results show great promise. At optimal conditions, this polychromatic force has about the same magnitude but almost twice the velocity range of the bichromatic force. Adding higher harmonics to the square wave modulation makes the pulses more similar to π -pulses as is shown in the Bloch vector trajectories. This square-wave stimulated force may be realized by modulating either the amplitude or the phase of two counter-propagating beams, instead of by overlapping four bichromatic CW beams. Splitting total laser power evenly between two rather than four beams partially accounts for the 70% enhancement in the predicted MOT loading rate compared to the chirped BCF method. Our simulation also shows that the square wave modulation reduces spontaneous emissions by up to 33% compared to the BCF method. This can help prevent heating, especially in atoms with shorter lifetimes, and population loss in multilevel systems and molecules.

Our model promises optimal experimental design for stimulated slowing and trapping of Yb atoms. The simulations we developed have flexibility and can be modified to investigate other two-level systems, such as other alkaline-earth-like atoms (e.g. Ca, Sr).

Chapter 5

Yb Atomic Magnetometer

5.1 Introduction

Following the theoretical and computational work on the stimulated slowing methods for Yb atoms with only the 556 nm laser (presented in Chapters 2-4), we set up a transverse beam deflection experiment to test that method. Square-wave amplitude-modulated laser light was set up in the transverse direction to deflect the thermal Yb atomic beam. A camera was placed above the intersection between the laser beam and the atomic beam to image the atoms' fluorescence. In the presence of a magnetic field gradient, my labmate, Hongquan Li, observed a dark-striped pattern across the atomic fluorescence that corresponds to magnetic field contour lines. The dark stripes were clearly visible both to the eye and the camera.

Following this intriguing discovery, I shifted the focus of my research to the theory and modeling of this magnetometer, which is the first atomic magnetometer that utilizes fluorescence imaging of thermal Yb atoms. Understanding the origin of the dark-striped pattern in the fluorescence requires a theoretical model that combines the Zeeman effect, Autler-Townes splitting [53], and the spatial Hanle effect [35, 54]. The combination of these effects has enabled us to both analyze and predict experimental observations. Based on fluorescence imaging of fast, thermal atoms, this magnetometer provides a powerful, novel method for imaging magnetic fields' contour lines and gradients and measurement of the magnetic fields' vector orientation.

Before I delve into the numerical model in Chapter 6, the inference of the magnetic fields' vector orientation in Chapter 7, and a demonstration of magnetic-field sensing in Chapter 8, this chapter will provide a brief contextual summary and lay the foundations for the following chapters. I give examples of recent magnetometers focusing on those that have imaging and vector capabilities, the two key features of our magnetometer. Later in Secs. 5.3 and 5.4, I briefly summarize the underlying effects that explain the dark stripes as mentioned above, namely Autler-Townes splitting, and the Hanle effect.

5.2 Atomic magnetometers

The development of magnetometers has a long history. Many different types of magnetometers were invented to measure magnetic fields or magnetic dipole moments. Among the earlier common technologies [128, 129] are Hall-effect [24] and fluxgate magnetometers [22, 23]. More recent prominent magnetometers that utilize quantum effects include SQUIDs (Superconducting Quantum Interference Devices) [25, 26], atomic magnetometers [28, 29, 30, 31, 32, 33], and diamond nitrogen-vacancy (NV) centers [27]. Here I give a few examples of atomic magnetometers that have spatial imaging [130, 51, 52, 131] or vector capabilities [39, 40, 41, 44, 48, 132, 133, 134, 135, 136, 137, 138, 139, 140, 141, 142, 143] or both [42, 49, 50, 144] as they are the most relevant for context and comparison with our system.

Many atomic magnetometers rely on interactions between resonant light and alkali atomic vapor (e.g. Cs, Rb, K) and the sensitivity of the ground state hyperfine structure to magnetic fields. The most common technique is to measure the Larmor precession frequency of the atoms' magnetic dipole moments. As described in the review of optical magnetometers [30] by Budker and Romalis, near-resonant light fields induce a prominent magnetic dipole direction for atoms in the ground state. In a magnetic field, the atoms' dipoles undergo Larmor spin precession, which alters the transmission of light through the vapor. Many excellent review articles [28, 29, 30, 31, 33] and books edited by Budker and Kimball [32] and Grosz, Haji-Sheikh,

and Mukhopadhyay [145] provide extensive background for these resonant magneto-optical techniques in optical magnetometry. These techniques have enabled some of the most sensitive and accurate methods for measuring magnetic fields.

The development of better diode lasers and denser vapor cells of alkali atoms with longer ground-state relaxation times have enabled atomic magnetometers that take advantage of the spin-exchange relaxation-free (SERF) regime [146, 147, 148, 149]. Dang, Maloof and Romalis developed a SERF magnetometer with a sensitivity of $0.16 \text{ fT}/\sqrt{\text{Hz}}$ [147]. The SERF technique is also a type of Hanle magnetometers. This subfemtotesla sensitivity has exceeded that of SQUID magnetometers, which are commonly used in neuroimaging for mapping brain activity [150]. While ultrasensitive sensors like SQUID and SERF magnetometers operate at near-zero fields in a shielded environment for applications in medicine [150] and fundamental physics [151], their limited dynamic range makes them unsuitable to measure larger fields and, unless modified, they can measure only the magnitude but not the direction of the magnetic fields. Other types of atomic magnetometers that operate in the non-SERF regime or rely on different types of measurements, as reviewed in Ref. [33], can perform in an unshielded environment (at Earth's field) and offer limited vector capabilities.

Among the notable atomic magnetometer technologies [33], some systems that are similar to our Autler-Townes-based magnetometer are those that utilize coherent quantum effects in multilevel atoms such as electromagnetically induced transparency (EIT) [37] and coherent population trapping (CPT) [38] to measure magnetic fields. One advantage of these EIT-based [40, 41, 42] and CPT-based [43, 44] magnetometers is the vector measurement of magnetic fields. Several examples of vector magnetometers are discussed below in Sec. 5.2.2. Our Yb magnetometer, which is based on Autler-Townes (AT) splitting [53], can also utilize laser polarization rotation to provide additional information about the vector directions of the magnetic fields, but, as discussed later Sec. 8.4.2, comparing our experimental data to the theoretical model can give the magnitudes of three B_x, B_y, B_z components without rotating the laser polarization at all.

While Cs, Rb, and K are the most widely used atomic vapor in magnetometers, two-electron atomic magnetometers such as He [144] and Sr [49] are less common.

Similar to our Yb system, the Sr magnetometer by Jackson & Durfee [49] utilizes fluorescence imaging of thermal atoms for spatial magnetic field measurements that provide vector information based on the Hanle effect [35, 36].

The only other Yb magnetometry system that we know of [152] measured magnetic fields through temporal measurements of the Larmor precession frequency and was based on a different type of theoretical model. There are many key differences between their system and ours. While their system measured the hyperfine splitting (375 Hz/G) in the $^1\text{P}_1$ state of the odd isotope ^{171}Yb , we use the Zeeman splitting (≈ 2.1 MHz/G) in the $^3\text{P}_1$ state of the even isotope ^{174}Yb with zero nuclear spin to avoid having to deal with the hyperfine structure and resulting optical pumping. Instead of Larmor frequency measurements like theirs, our system utilizes spatial fluorescence imaging of dark resonances from Autler-Townes and the spatial Hanle effects, neither of which were investigated in their system.

Our Yb magnetometer's unique capabilities include fast imaging of the magnetic fields' contour lines and gradients and measurement of the magnetic fields' vector orientation. To put these features into context, I will briefly mention other magnetometer systems that have related capabilities.

5.2.1 Imaging of magnetic fields

One desirable feature of magnetometers is the ability to take spatially-resolved measurements of magnetic fields for mapping magnetic fields' contours and gradients. Different spatial imaging approaches that have been developed for magnetic field measurements include fluorescence imaging [49, 130, 131], absorption imaging [42, 50] and imaging of BECs [51, 52]. Taking advantage of small sensors, some systems including Ref. [153] used atomic magnetometers to raster scan and take spatially resolved measurements. One drawback of this method is that it takes much longer (40 ms/pixel [153]) to perform a complete 2D scan of the measurement area with a small sensor than to capture a single image on a camera. This scanning probe technique for magnetic field imaging is increasingly common with nanoscale diamond NV-center magnetometers [154], but the downsides remain the long measurement time and the

lack of accurate calibration.

Instead of scanning the measurement area with small magnetometers, BEC imaging [51, 52] provides an alternative high-resolution and sensitive method for magnetic field imaging. In Ref. [51], Vengalattore et al. developed an imaging magnetometer based on imaging of Larmor precession of spin-polarized ^{87}Rb condensates. Their method achieved good sensitivity on the order of $\text{pT}/\sqrt{\text{Hz}}$, and data collection took 250 ms for $120 \mu\text{m} \times 120 \mu\text{m}$ image size. Another notable BEC imaging magnetometer is the Scanning Quantum Cryogenic Atom Microscope (SQCRAMscope) developed by Yang et al. [52]. Both the Rb spinor BEC [51] and the SQCRAMscope, which utilizes magnetically levitated BECs, achieved the imaging resolution near the $\sim \mu\text{m}$ range. Fig. 4 in Ref. [52] and references therein provide a good comparison between similar imaging magnetometers in terms of both sensitivity and spatial resolution. Both of these BEC imaging methods are comparable to other scanning probe methods that utilize sensitive NV centers, SQUIDs, or Hall effect magnetometers in terms of sensitivity and resolution, but one main advantage of systems like the SQCRAMscope is the ability to put the magnetic sensor very close to the samples or surfaces of interest.

While magnetic field measurements via fluorescence (this work and [49, 130, 131]) and absorption [42, 50] imaging can be less competitive in terms of sensitivity, the data collection is fast as the rate is set by the video frame rates (resulting in measurement time of $< 200 \mu\text{s}$ in our system). In a short time, these imaging methods simultaneously take a large number of spatially-resolved measurements as well as provide information about the vector orientation of the magnetic fields. In Ref. [50], a spatial Fourier analysis of a single absorption image of cold ^{87}Rb atoms probed with a vector vortex laser beam enabled 3D magnetic field measurement. In Ref. [42], EIT absorption of a radially polarized vector beam by a warm ^{87}Rb vapor depends on the transverse magnetic-field strength and orientation. Both of these absorption-based vector magnetometers [42, 50] can take many spatially-resolved measurements in a single mm-scale imaging frame.

Instead of absorption imaging, a magnetometer that is more similar to our Yb

system, which utilizes fluorescence imaging of thermal alkali earth-like atoms, is described in Ref. [49]. Jackson and Durfee used fluorescence imaging of a thermal Sr atomic beam to characterize the magnetic field in their magneto-optical trap (MOT). The spatial Hanle effect [35, 36], which determines the orientation and spatial distribution of the atoms' dipole radiation pattern, produces prominent dark spots in the fluorescence where the magnetic field is zero given that the imaging direction (depending on camera location) is along the laser polarization direction. The visible dark spots seen on their fluorescence images allowed the authors to quickly locate the trapping region and optimize the magnetic field settings in their MOT. In our Yb system, we observed similar dark features due to the Hanle effect at or near zero magnetic fields as well as additional dark stripes produced by dark resonances due to Autler-Townes splitting. I have referred to the quantum (density matrix) model described in the supplemental material for Ref. [49] to incorporate the Hanle effect in our Yb magnetometer model. While we observed additional dark stripes due to dark resonances from Autler-Townes splitting in the 1S_0 - 3P_1 in Yb, Jackson and Durfee used the 1S_0 - 1P_1 transition in Sr and did not report any observations of dark resonances at non-zero fields like we did because they operated in a weak optical field limit where Autler-Townes effects are insignificant.

As mentioned previously, several of the imaging magnetometers described above [42, 49, 50] are capable of vector measurements of magnetic fields. Some other types of vector atomic magnetometers are discussed below.

5.2.2 Vector magnetometers

While many sensitive magnetometers including SQUIDs [25, 26], spin-exchange relaxation-free (SERF) [146], and optical pumping magnetometers [155] can measure only the magnitude of the magnetic fields, other magnetometry approaches such as EIT [39, 40, 41, 42], CPT [44], the Hanle effect [48, 49], the Voigt effect [138], spatial analysis of vector vortex beam absorption [42, 50], and microwave polarization reconstruction [136] have vector capabilities. Alternatively, adding more laser beams and/or oscillating magnetic fields in different directions [133, 134, 139, 141, 142, 143, 144]

can make intrinsically scalar Larmor precession measurements or optical pumping magnetometers sensitive to the magnetic fields' vector orientation.

In our system and several of the EIT [40] and CPT systems [44], rotating the laser polarization direction reveals information about the vector orientation of the magnetic fields. In EIT, CPT, and Autler-Townes splitting, absorption, transmission, and fluorescence signals are sensitive to the angle between the laser polarization and the magnetic field vector because the relative angle defines which type(s) of atomic transitions (σ^+ , σ^- , or π) are allowed. In the EIT magnetometer developed by Cox et al. [40], the authors measured seven Zeeman shifted EIT resonances in ^{87}Rb . While the spectral positions of the resonances reveal the magnitude of the magnetic field, the direction of the field can be deduced [156] from the relative amplitudes of the EIT peaks. More recently, kernel principal component analysis (KPCA), an unsupervised machine learning technique, was employed [157] in the prediction of magnetic field vector orientation from these EIT resonance spectra. The model was trained on a large spectral dataset taken at different laser polarization and magnetic field directions. KPCA was used to map each spectrum containing seven EIT peaks onto a 3D space for a subsequent regression step to deduce the magnetic field's orientation. Similar techniques can be applied in other magnetometer systems that rely on optical spectroscopy.

Although our Yb magnetometer also relies on laser polarization rotation for enhanced vector measurements, the dark resonances that we observe are in the spatial domain not in the frequency domain like the magnetometers that measure EIT [40] and CPT [44] spectra. Therefore, we would need different data analysis techniques for predictions of the vector orientation from the fluorescence images. For our Yb magnetometer, the analysis of the laser polarization dependence for vector measurements is covered in Chapter 7 of this thesis.

Having provided examples of relevant atomic magnetometers with similar imaging and vector capabilities, the next section of this chapter will provide more background specific to our Yb magnetometer. I will briefly cover the two phenomena underlying our observations of dark resonances in the fluorescence: Autler-Townes splitting [34] and the spatial Hanle effect [35, 36].

5.3 Autler-Townes splitting

Autler-Townes effect was discovered by Autler and Townes in 1955 [34]. In a microwave transition of carbonyl sulfide (OCS), strong coupling (via a strong resonant rf field) between one of the levels in the transition and a third level causes the levels to split into two components due to AC Stark shifts. Such splitting in the energy levels results in an effective decrease in absorption and, as discovered later, fluorescence. Autler and Townes carried out time-dependent perturbation calculations as well as experimentally observed the splitting in two microwave absorption lines in OCS. From their approximate solutions to the time-dependent perturbation calculations, on resonance, each absorption line is split into two equally strong components separated by the Rabi frequency of the perturbing field. This effect can manifest as a splitting of a single Lorentzian peak into a doublet. Because the separation between two peaks is given by the Rabi frequency, this doublet separation is proportional to the electric-field amplitude of the perturbing field and is more clearly observed when the field is strong. Illustrations of the level splitting in our system and the numerically calculated doublet fluorescence lineshape are presented and discussed later in Sec. 6.3.1 (see Figs. 6.3 and 6.4).

Autler-Townes effect can also be analyzed using the dressed-atom approach [158, 159]. In the dressed-state picture, Cohen-Tannoudji quantized the strong resonant perturbation field instead of expressing it semi-classically as a sinusoidal driving field. Combining the quantized state of photons and atom allows for a representation of Autler-Townes splitting as an anticrossing of two eigenenergies of the dressed state. On resonance, the energy separation between this anticrossing is \hbar times the Rabi frequency, which is consistent with the result from the semiclassical model by Autler and Townes [34].

The review by Cohen-Tannoudji [159] also covers demonstrations of Autler-Townes effects in multilevel atoms with optical transition frequencies, which allows for this effect to be observed via atomic fluorescence. Examples of such experiments include Ref. [160], which observed the Autler-Townes doublet in spectral measurements using a beam of Na atoms and laser fields in the transverse direction to the atoms.

Classifying Autler-Townes splitting as doublets of dressed states also highlights the similarities to the Mollow triplet [161], which describes the three spectral components of fluorescence from a single transition at high intensity or large detuning. Another similar effect to Autler-Townes is the vacuum Rabi splitting in cavity quantum electrodynamics (cavity QED) [162], which can be analyzed using the Jaynes-Cummings model [163].

For our context and application, which focus on interactions between multiple strong driving fields and a multilevel atom, optical coherent effects that are similar to AT splitting include electromagnetically induced transparency (EIT) [37] and coherent population trapping (CPT) [38]. As reviewed previously in Sec. 5.2.2, some magnetometers [40, 43, 44] rely on EIT and CPT measurements for both scalar and vector measurements of the magnetic fields. AT splitting, EIT, and CPT have been observed in different types of three-level systems: Λ , V, cascade-B, and cascade-U. These configurations are illustrated in Fig. 5.1. In our Yb system, when driven by two optical fields, two (out of three) of the Zeeman sublevels in the excited state 3P_1 and the single ground state 1S_0 form a V system like the one shown in Fig. 5.1(b). In our analysis, the two driving fields have equal or comparable intensities, so we do not designate them as coupling or probe fields nor make any assumptions about their relative strengths, but for the purpose of discussing the analyses and comparisons between EIT and AT from other literature [164, 165, 166], the diagrams in Fig. 5.1 use the coupling and probe beam notations from Ref. [164], assuming that the probe beam is weak and the probe detuning δ_p is swept to measure the spectral lineshapes. Ω_c and Ω_p represent the Rabi frequencies of the coupling (strong) field and the probe (weak) field, respectively.

Because both EIT and AT splitting can lead to a decrease in absorption on resonance, discerning the effects of these two mechanisms has caught interest [164, 165, 166]. While EIT is a result of destructive Fano interference between two transition pathways [167], AT splitting is caused by strong-field AC Stark effects. To distinguish EIT and AT in the four different types of three-level systems shown in Fig. 5.1, Abi-Salloum's theoretical analysis expressed the probe absorption spectra for the Λ , V, and cascade systems into two components (resonances) and analyzed the respective

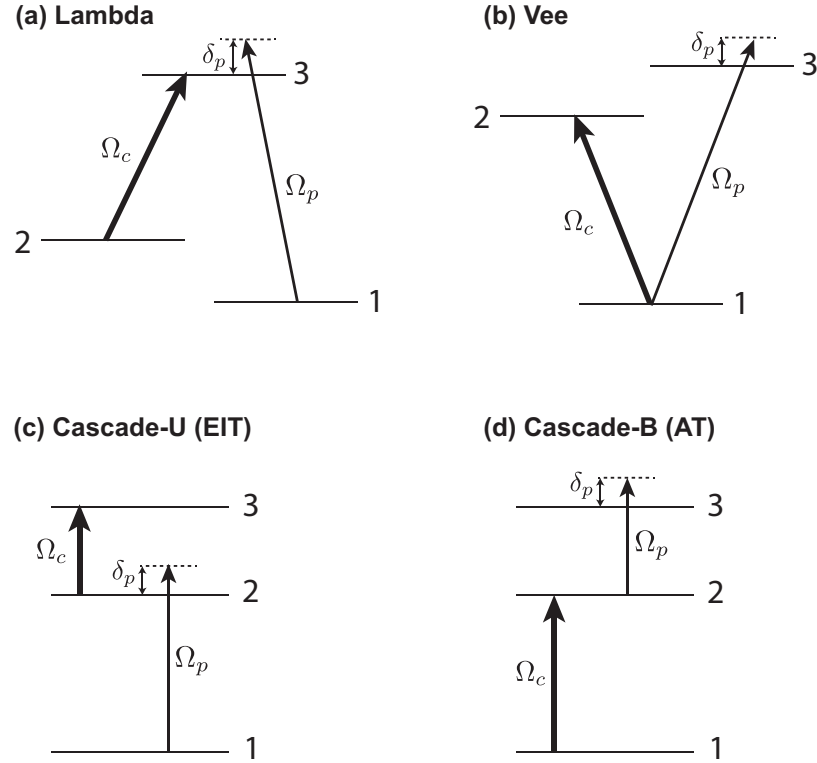


Figure 5.1: Different types of three-level systems: (a) Λ , (b) V , (c) cascade-U (EIT) and (d) cascade-B (AT). Ω_c and Ω_p represent the Rabi frequencies of the coupling (strong) field and the probe (weak) field, respectively. The diagrams and notations here are based on the analysis in [164], where the probe field is assumed weak and the spectral lineshapes of EIT and AT are generated by sweeping the probe detuning δ_p .

amplitudes in different Ω_c (coupling field strength) regimes. He concluded that in the strong field regimes $\Omega_c > \Omega_t$, where Ω_t is the threshold value that depends on the relevant decay rates present in different types of the systems ($\Omega_t = \gamma_{12}$ in the V and cascade-B systems, and $\Omega_t = |\gamma_{12} - \gamma_{13}|$ in the Λ and cascade-U systems), AT splitting, where the dark resonance corresponds to the “gap” between the two resonances, is the dominant mechanism observed in all four types of systems. On the other hand, in the weak-field regime where $\Omega_c < \Omega_t$, only one resonance remains in the V and cascade-B (AT) systems. This result is consistent with our numerical calculation in Fig. 6.4 showing singlet Lorentzian peaks in the weak field case as opposed to the

Autler-Townes doublet. In contrast, in the Λ and cascade-U (EIT) systems, when $\Omega_c < \Omega_t$, EIT still produces transparency in the absorption spectra [164], which leads to a conclusion that EIT does not occur in V and cascade-B systems. Several other references such as [166] did not make this strong claim and sometimes had contradictory conclusions. To distinguish whether an experimental observation is produced by AT or EIT, Anisimov et al. proposed a method [166] based on Akaike's information criterion, which was also applied in Ref. [168].

In this work, our numerical model (described in detail in Chapter 6), which is based on solving the Linblad Master equation, has enabled an analysis of Autler-Townes effect in the 1S_0 - 3P_1 transition in Yb. This four-level atom consists of three possible V configurations depending on which of the two transitions are being considered. The optical driving fields are frequency sidebands of square-wave amplitude-modulated laser light at 556 nm, hence their strengths are comparable, and as stated previously, we do not classify them as coupling or probe beams nor assume one is weaker than the other. Instead of tuning one of the laser frequencies to capture fluorescence and absorption spectra, the excited states are Zeeman-shifted such that the $m_J = \pm 1$ levels in the 3P_1 state shift simultaneously in opposite directions in a non-zero magnetic field. Doppler broadening from the transverse velocities of atoms in the atomic beam is incorporated numerically by averaging the fluorescence from $N = 1000$ atoms or more with transverse velocities sampled from a Gaussian distribution with a Gaussian width of $\sigma \approx 4.5$ m/s, approximate width of our atomic beam based on the atomic beam divergence (half-angle of divergence of 17 mrad). The numerical model allows us to investigate and characterize the effects of Doppler broadening on the Autler-Townes lineshape for our magnetic field sensing purposes.

5.4 Hanle effect

Hanle effect [35, 36] generally refers to the redistribution of polarized light scattered by an atomic vapor. This effect is sensitive to both the magnitude and direction of the magnetic field, and hence has been used to develop vector magnetometers [48, 49]. The Hanle effect also determines the spatial distribution of the fluorescence light

emitted by atoms depending on the laser polarization direction and the magnetic field. As described earlier in Sec. 5.2.1, the Sr magnetometer developed by Jackson and Durfee based on fluorescence imaging, which has both spatial imaging and vector features, relies on the spatial Hanle effect to locate the trapping region in their MOT where the magnetic field is zero [49]. Their paper [49] provides a concise review and description of the Hanle effect, which I will briefly summarize here.

Without the magnetic field present, light interacting with an atom induces a dipole moment oscillating along the laser polarization direction. The spatial shape of the atom's dipole radiation pattern is a toroid (donut shape) symmetric around the laser polarization axis. This means that light emitted by the atom will not reach a (small) detector that is precisely located along the polarization axis. In Jackson and Durfee's magnetometer, this spatial Hanle effect produced visible dark spots [49] in the fluorescence images of thermal Sr atoms where the magnetic field is zero. These dark spots allowed the authors to characterize and optimize the trapping region in their MOT. On the other hand, introducing a magnetic field causes a precession of the dipole oscillation axis to rotate around the field and changes the polarization of the light emitted by the atom.

In this work, we are interested in calculating the atomic fluorescence detected by the camera located above the interaction region where the laser “light sheet” intersects with the atomic beam (see Fig. 6.1 in Chapter 6). In most cases, the laser is linearly polarized along the vertical direction, meaning our camera (detector) is located along the polarization axis and would not see any fluorescence light at zero magnetic field. The spatial Hanle effect provides an initial qualitative prediction (no fluorescence observed at zero magnetic field) and an explanation for one of the prominent dark features in our fluorescence images.

To quantitatively account for the Hanle effect, the supplemental material of Ref. [49] presents several methods to calculate the emitted light intensity pattern ranging from classical to semiclassical, to quantum. The authors analytically derived the light intensity emitted along different directions as a function of magnetic field strength from all the models, assuming a weak optical driving field. In our system, however, multiple strong optical fields are present, so we cannot directly use their analytic solutions

for our fluorescence calculation, but we can apply their quantum model, which is based on the density matrix calculation, to numerically calculate the light intensity emitted by the atoms along the vertical direction towards the camera.

The quantum model from Ref. [49] is based on the Hanle effect calculation by Avan and Cohen-Tannoudji [169] for a four-level atom ($J = 0 \rightarrow J' = 1$ transition), like our 1S_0 - 3P_1 transition in Yb, driven by an optical field. By writing down the 4×4 Hamiltonian and solving the Master equation for the density matrix, the intensity of light emitted along different directions depends on a combination of diagonal density matrix elements representing the population of atoms in the excited states that would emit light upon spontaneous decays and off-diagonal density matrix elements representing coherences between the excited states.

This method of calculating the Hanle effect is easily incorporated into our model, which is based on solving the Master equation numerically for the density matrix. See Sec. 6.4 for a complete derivation. For our experimental configuration, we are most interested in the intensity of light emitted along the vertical (y) direction, which consists of z -polarized light emitted from the $m_J = 0$ state and x -polarized light from a combination of the $m_J = \pm 1$ states. The input laser polarization is linear and its direction can be rotated in the yz plane, as illustrated in Fig. 6.1 in Chapter 6.

Overall, our density matrix model incorporates both the Autler-Townes and the spatial Hanle effects occurring in the four-level Zeeman-shifted system to predict the fluorescence pattern as a function of magnetic fields. The theoretical results help us understand the underlying physics as well as predict our experimental observations. Chapters 6 and 7 present the theoretical model and results for both scalar and vector measurements of the magnetic fields, and then Chapter 8 will demonstrate that our system can be used for gradient mapping and vector measurements of magnetic fields.

Chapter 6

Numerical Model

6.1 Overview

This chapter goes over the derivation of our theoretical model of the Yb magnetometer. We built the model based on the experimental setup in our lab, as shown in Fig. 6.1. A Yb atomic beam exits an oven at $\sim 450^\circ\text{C}$ and travels horizontally in the $+z$ direction. A laser beam at 556 nm is propagating in the $+x$ direction, transverse to the atomic beam. The laser beam is linearly polarized, and its polarization can be rotated in the yz plane by a motorized half-wave plate. θ defines the angle between the laser polarization direction and the horizontal axis z , where $\theta = 90^\circ$ corresponds to y -polarization (vertical) and $\theta = 0^\circ$ corresponds to z -polarization (horizontal). The laser is square-wave amplitude modulated at the modulation frequency δ_{mod} , which is variable but typically in the MHz range. The square wave modulation duty cycle is set at 10% to maximize the number of frequency sidebands (we discuss this later in Sec. 8.2) and optimize the dark-line contrast. In the Fourier space, the laser beam contains a carrier (at the laser frequency ω_L) and evenly spaced sidebands at $\omega_L \pm n\delta_{mod}$ (where n is an integer). For fluorescence imaging, a camera is set up above the interaction region to collect images of the xz plane.

The interaction region (dashed cube) on the schematic diagram is located ≈ 20 cm away from a pair of large anti-Helmholtz coils and in proximity to a permanent magnet in a Zeeman slower, which sits between the interaction region and the oven

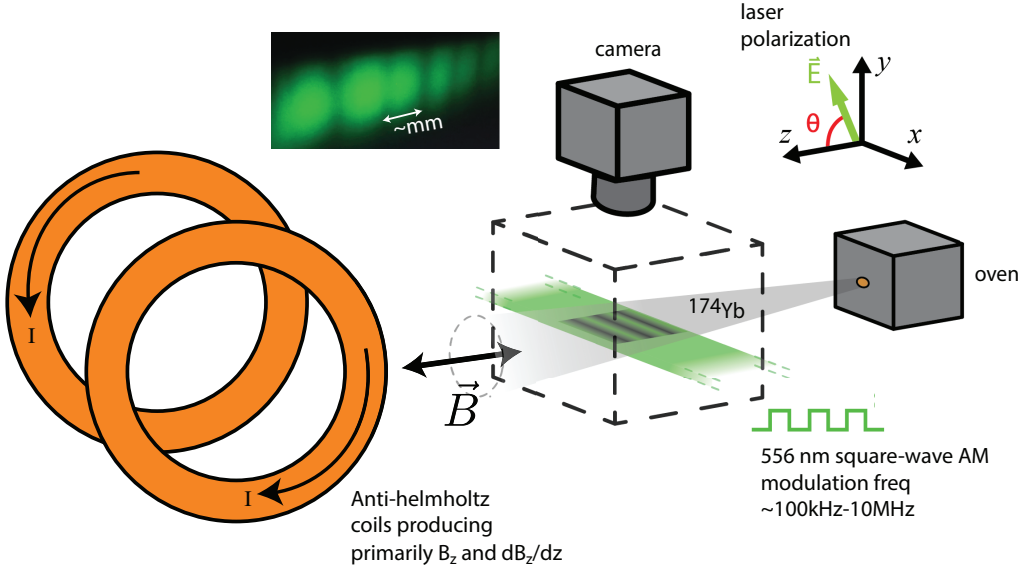


Figure 6.1: Experimental schematic showing an atomic beam traveling in the z -direction (horizontal), a square-wave amplitude-modulated laser beam propagating in the x -direction transverse to the atoms. The laser is linearly polarized in the yz plane, making an angle of θ with the z -axis. The camera collects atomic fluorescence from the imaging (xz) plane. A large pair of anti-Helmholtz coils produce a magnetic field and a magnetic field gradient primarily along the z -direction. An example image of the dark stripes are shown where the dark lines are $\sim\text{mm}$ apart.

(not shown in the schematic here). With a current in the anti-Helmholtz coils, the coils produce a magnetic field gradient that is primarily along the z -axis. As depicted in Fig. 6.1, the magnetic field gradient produces a series of prominent dark stripes in the fluorescence images. The stripes are oriented along the x direction, perpendicular to the gradient, resembling magnetic field contour lines.

To understand the origin of the dark lines and their dependence on the magnetic field, we developed a numerical model of a four-level atom driven by strong laser fields. Focusing on even isotopes of Yb (including the most abundant ^{174}Yb), which have zero nuclear spin $I = 0$ and thus no hyperfine splitting, the four energy levels included in the model consist of the ground state $^1\text{S}_0$ and the three Zeeman sublevels in the $^3\text{P}_1$ state, with $m_J = -1, 0, 1$. The ground state does not have any magnetic sublevels.

6.2 Constructing the system's Hamiltonian

Here we derive the Hamiltonian that describes a 4-level atom, the perturbation from weak-field Zeeman shifts, and electric dipole interactions between the driving laser fields and the atom. The total Hamiltonian is given by

$$H = H_0 + V_{ZS} + V_D \quad (6.1)$$

where H_0 is the unperturbed atom's Hamiltonian, V_{ZS} is the Zeeman shifts and V_D is the electric dipole interactions with the laser.

Starting with one ground state and three excited states (with $m_J = -1, 0, 1$), the unperturbed Hamiltonian for the 4-level atom is

$$H_0 = 0|g\rangle\langle g| + \omega_0|e_1\rangle\langle e_1| + \omega_0|e_0\rangle\langle e_0| + \omega_0|e_{-1}\rangle\langle e_{-1}| \quad (6.2)$$

where ω_0 is the transition frequency for the 1S_0 - 3P_1 transition.

Next, add the perturbation by the magnetic field \vec{B} . Assuming the weak-field limit, total angular momentum J is conserved, and linear Zeeman shifts in the $J = 1$ excited states are given by

$$V_{ZS} = -\vec{\mu} \cdot \vec{B} = g\mu_B(\vec{J} \cdot \vec{B}) = g\mu_B(\hat{J}_x B_x + \hat{J}_y B_y + \hat{J}_z B_z) \quad (6.3)$$

where the Landé g-factor $g = 1.5$ (measured value for Yb is 1.49282 [170]) for the 3P_1 state. Bohr magneton $\mu_B = e\hbar/2m_e \approx 9.274 \times 10^{-24}$ JT $^{-1}$. J_x , J_y , and J_z represent the three components of the angular momentum operator.

$$J_x = \frac{1}{\sqrt{2}} \begin{pmatrix} 0 & 1 & 0 \\ 1 & 0 & 1 \\ 0 & 1 & 0 \end{pmatrix} \quad (6.4)$$

$$J_y = \frac{1}{\sqrt{2}} \begin{pmatrix} 0 & -i & 0 \\ i & 0 & i \\ 0 & i & 0 \end{pmatrix} \quad (6.5)$$

$$J_z = \begin{pmatrix} 1 & 0 & 0 \\ 0 & 0 & 0 \\ 0 & 0 & -1 \end{pmatrix}. \quad (6.6)$$

In the case where the magnetic field \vec{B} only contains the z-component, $\vec{B} = (0, 0, B)$, V_{ZS} simplifies to $\sum m_J g \mu_B B |e_{m_J}\rangle \langle e_{m_J}| = g \mu_B B |e_1\rangle \langle e_1| - g \mu_B B |e_{-1}\rangle \langle e_{-1}|$. For this transition, with the given g-factor $g = 1.5$, $B = 1$ Gauss results in the Zeeman energy shift $g \mu_B B \approx 2.1$ MHz.

Finally, add the time-dependent electric dipole perturbation of the light fields. We need at least two light fields (two different frequencies) to form an effective V-system and produce Autler-Townes splitting. Starting with two coherent laser fields with amplitudes E_1, E_2 and frequencies ω_1, ω_2 with the same polarization vector $\vec{\epsilon}$, V_D is given by

$$V_D = \hat{d} \cdot \vec{E} = \sum_{m_J} \langle g | \hat{d} \cdot \vec{\epsilon} | e_{m_J} \rangle (E_1 \cos(\omega_1 t) + E_2 \cos(\omega_2 t)). \quad (6.7)$$

6.2.1 Baseline model (y-polarized light)

In the baseline model, the laser is linearly polarized in the vertical (y) direction, and the magnetic field lies along the horizontal (z) axis $\vec{B} = (0, 0, B)$. Note that the laser beam propagates in the $+x$ direction. In this setting, only σ^+ and σ^- transitions are allowed between the ground state to the excited states with $m_J = \pm 1$, as shown in Fig. 6.2a. Only two laser frequencies are included in the model initially. As Fig. 6.2b shows, 10% duty square-wave modulation produces many evenly spaced sidebands with the spacing of δ_{mod} between two consecutive ones. The baseline model only includes the two first-harmonic sidebands, highlighted in Fig. 6.2b, that are symmetrically detuned by $\pm \delta_{mod}$ from the resonance transition frequency between the ground and $m_J = 0$ excited state.

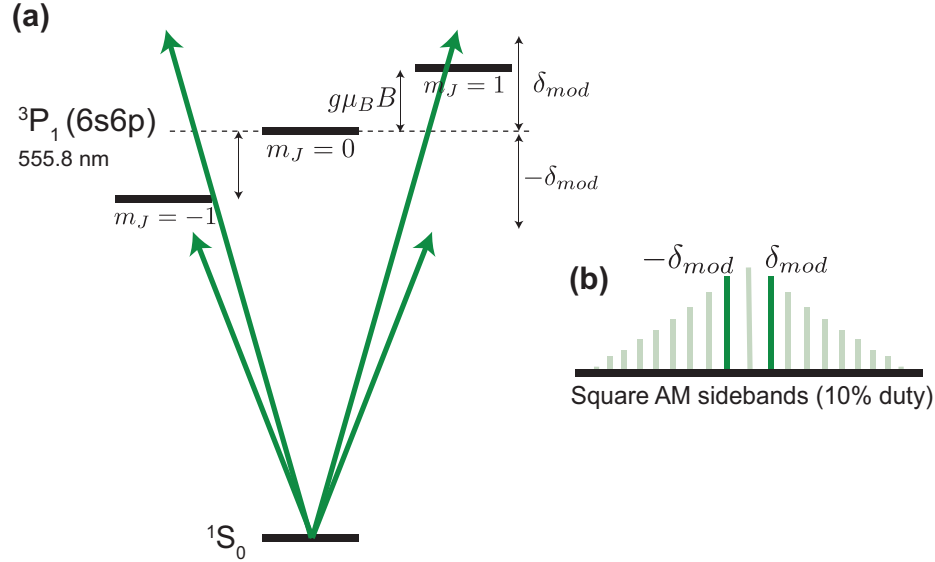


Figure 6.2: (a) Energy level diagram of the 1S_0 - 3P_1 transition in Yb. (b) Carrier and sideband frequencies in the square-wave AM light at a modulation frequency δ_{mod} . Only the first harmonic sidebands with detunings $\pm\delta_{mod}$ (darker vertical lines) are included in the energy level diagram in (a) and in our initial numerical model.

For this four-level atom, an atomic state can be represented by a vector

$$|\psi| = \begin{pmatrix} A_g \\ A_1 \\ A_0 \\ A_{-1} \end{pmatrix} \quad (6.8)$$

where A_1, A_0 and A_{-1} represent the amplitudes of the $m_J = 1, 0, -1$ excited states, respectively, and A_g represents the amplitude of the ground state. Next, we can write down the total Hamiltonian $H = H_0 + V_{ZS} + V_D$ as a 4×4 matrix:

$$H_y = \hbar \begin{pmatrix} 0 & -\frac{i}{\sqrt{6}}\Omega(t) & 0 & -\frac{i}{\sqrt{6}}\Omega(t) \\ \frac{i}{\sqrt{6}}\Omega(t) & \omega_0 + \frac{g\mu_B}{\hbar}B & 0 & 0 \\ 0 & 0 & \omega_0 & 0 \\ \frac{i}{\sqrt{6}}\Omega(t) & 0 & 0 & \omega_0 - \frac{g\mu_B}{\hbar}B \end{pmatrix} \quad (6.9)$$

where $\Omega(t) = \Omega_1 \cos(\omega_1 t) + \Omega_2 \cos(\omega_2 t)$ with Ω_1 and Ω_2 denoting the Rabi frequencies of the two light fields: $\Omega_{1,2} = \sum_{m_J} E_{1,2} \langle g | \hat{d}_y | e_{m_J} \rangle$. The factor of $1/\sqrt{6}$ in front of $\Omega(t)$ arises from the Clebsch–Gordan coefficients of the excited states. I also used the Atomic Density Matrix package on Mathematica [171] to verify this derivation and subsequent derivations for arbitrary linear polarization directions and B-field directions.

6.2.2 Arbitrary linear polarization

So far, we have assumed that the laser beam is linearly polarized along the y -axis (vertical). In our experiment, we can rotate the laser polarization direction in the yz plane. Let θ denote the angle between the laser's polarization direction and the horizontal axis (z). $\theta = 0^\circ$ means the laser is horizontally polarized (along the z -axis), and $\theta = 90^\circ$ means the laser is vertically polarized (along the y -axis).

With the quantization axis along z , when the laser polarization is also along z ($\theta = 0^\circ$), only π -transitions from the ground state 1S_0 to the $m_J = 0$ state are allowed. In this case, the Hamiltonian becomes

$$H_z = \hbar \begin{pmatrix} 0 & 0 & \frac{1}{\sqrt{3}}\Omega(t) & 0 \\ 0 & \omega_0 + \frac{g\mu_B}{\hbar}B_z & 0 & 0 \\ \frac{1}{\sqrt{3}}\Omega(t) & 0 & \omega_0 & 0 \\ 0 & 0 & 0 & \omega_0 - \frac{g\mu_B}{\hbar}B_z \end{pmatrix} \quad (6.10)$$

. Hence, for a general linear polarization with angle θ with respect to the z -axis,

$$H_\theta = \hbar \begin{pmatrix} 0 & -\frac{i}{\sqrt{6}}\Omega(t)\sin\theta & \frac{1}{\sqrt{3}}\Omega(t)\cos\theta & -\frac{i}{\sqrt{6}}\Omega(t)\sin\theta \\ \frac{i}{\sqrt{6}}\Omega(t)\sin\theta & \omega_0 + \frac{g\mu_B}{\hbar}B_z & 0 & 0 \\ \frac{1}{\sqrt{3}}\Omega(t)\cos\theta & 0 & \omega_0 & 0 \\ \frac{i}{\sqrt{6}}\Omega(t)\sin\theta & 0 & 0 & \omega_0 - \frac{g\mu_B}{\hbar}B_z \end{pmatrix} \quad (6.11)$$

. Note that $\Omega(t)$ remains $\Omega_1 \cos(\omega_1 t) + \Omega_2 \cos(\omega_2 t)$, for Rabi frequencies Ω_1, Ω_2 and two respective optical frequencies ω_1, ω_2 .

6.2.3 B_x and B_y components

In most of our experiments, the magnetic field and its gradient are primarily along the z -axis, but background fields from the Earth's field and the permanent magnet in our Zeeman slower generate fields with x and y components. Magnetic field components B_x and B_y are incorporated in the Hamiltonian via the dot product of the field \vec{B} and the $3 \times 3 \vec{J}$ operators with components defined previously in eqs. (6.4), (6.5), and (6.6). Hence, the x and y components of the B-fields show up in the Hamiltonian as off-diagonal elements. To simplify the notation for the i th component, let $\frac{g\mu_B}{\hbar}B_i = b_i$. We can rewrite H_θ as

$$H_\theta = \hbar \begin{pmatrix} 0 & -\frac{i}{\sqrt{6}}\Omega(t)\sin\theta & \frac{1}{\sqrt{3}}\Omega(t)\cos\theta & -\frac{i}{\sqrt{6}}\Omega(t)\sin\theta \\ \frac{i}{\sqrt{6}}\Omega(t)\sin\theta & \omega_0 + b_z & \frac{1}{\sqrt{2}}(b_x - ib_y) & 0 \\ \frac{1}{\sqrt{3}}\Omega(t)\cos\theta & \frac{1}{\sqrt{2}}(b_x + ib_y) & \omega_0 & \frac{1}{\sqrt{2}}(b_x - ib_y) \\ \frac{i}{\sqrt{6}}\Omega(t)\sin\theta & 0 & \frac{1}{\sqrt{2}}(b_x + ib_y) & \omega_0 - b_z \end{pmatrix}. \quad (6.12)$$

6.2.4 Rotating Wave Approximation

Because the detunings $|\Delta_{1,2}| = |\omega_{1,2} - \omega_0|$ and Zeeman splitting $\pm g\mu_B B$ are much smaller than the optical transition frequency ω_0 , we can make a unitary transformation and the rotating-wave approximation to simplify the time-dependent Hamiltonian H_θ .

To transform into a reference frame that is rotating at ω_0 , we apply a unitary transformation on the density matrix and the Hamiltonian with the following unitary operator

$$U = \begin{pmatrix} 1 & 0 & 0 & 0 \\ 0 & e^{-i\omega_0 t} & 0 & 0 \\ 0 & 0 & e^{-i\omega_0 t} & 0 \\ 0 & 0 & 0 & e^{-i\omega_0 t} \end{pmatrix} \quad (6.13)$$

. In this rotating frame, the density matrix ρ and the system's Hamiltonian H become

$$\tilde{\rho} = U^\dagger \rho U \quad (6.14)$$

$$\tilde{H}(t) = -i\hbar U^\dagger \frac{\partial U}{\partial t} + U^\dagger H(t) U \quad (6.15)$$

. The density matrix becomes

$$\tilde{\rho} = \begin{pmatrix} \rho_{00} & \rho_{01} e^{-i\omega_0 t} & \rho_{02} e^{-i\omega_0 t} & \rho_{03} e^{-i\omega_0 t} \\ \rho_{10} e^{i\omega_0 t} & \rho_{11} & \rho_{12} & \rho_{13} \\ \rho_{20} e^{i\omega_0 t} & \rho_{21} & \rho_{22} & \rho_{23} \\ \rho_{30} e^{i\omega_0 t} & \rho_{31} & \rho_{32} & \rho_{33} \end{pmatrix} \quad (6.16)$$

, and the Hamiltonian from Eq. (66) becomes

$$H_\theta = \hbar \begin{pmatrix} 0 & -\frac{i}{\sqrt{6}} e^{-i\omega_0 t} \Omega(t) \sin \theta & \frac{1}{\sqrt{3}} e^{-i\omega_0 t} \Omega(t) \cos \theta & -\frac{i}{\sqrt{6}} e^{-i\omega_0 t} \Omega(t) \sin \theta \\ \frac{i}{\sqrt{6}} e^{i\omega_0 t} \Omega(t) \sin \theta & b_z & \frac{1}{\sqrt{2}} (b_x - i b_y) & 0 \\ \frac{1}{\sqrt{3}} e^{i\omega_0 t} \Omega(t) \cos \theta & \frac{1}{\sqrt{2}} (b_x + i b_y) & 0 & \frac{1}{\sqrt{2}} (b_x - i b_y) \\ \frac{i}{\sqrt{6}} e^{i\omega_0 t} \Omega(t) \sin \theta & 0 & \frac{1}{\sqrt{2}} (b_x + i b_y) & -b_z \end{pmatrix}. \quad (6.17)$$

Next, we make the rotating wave approximation. Expanding $\Omega(t) = \frac{\Omega_1}{2}(e^{i\omega_1 t} + e^{-i\omega_1 t}) + \frac{\Omega_2}{2}(e^{i\omega_2 t} + e^{-i\omega_2 t})$ and dropping fast rotating terms $e^{\pm i(\omega_0 + \omega_1)t}$ and $e^{\pm i(\omega_0 + \omega_2)t}$ give us

$$\begin{aligned} e^{-i\omega_0 t} \Omega(t) &= \frac{\Omega_1}{2} e^{-i\omega_0 t} (e^{i\omega_1 t} + e^{-i\omega_1 t}) + \frac{\Omega_2}{2} e^{-i\omega_0 t} (e^{i\omega_2 t} + e^{-i\omega_2 t}) \\ &\approx \frac{1}{2} (\Omega_1 e^{i\Delta_1 t} + \Omega_2 e^{i\Delta_2 t}) = \frac{\tilde{\Omega}(t)}{2} \\ e^{i\omega_0 t} \Omega(t) &\approx \frac{1}{2} (\Omega_1 e^{-i\Delta_1 t} + \Omega_2 e^{-i\Delta_2 t}) = \frac{\tilde{\Omega}^*(t)}{2} \end{aligned}$$

. Hence the Hamiltonian after RWA is

$$\tilde{H}_\theta = \begin{pmatrix} 0 & -\frac{i}{2\sqrt{6}}\tilde{\Omega}(t)\sin\theta & \frac{1}{2\sqrt{3}}\tilde{\Omega}(t)\cos\theta & -\frac{i}{2\sqrt{6}}\tilde{\Omega}(t)\sin\theta \\ \frac{i}{2\sqrt{6}}\tilde{\Omega}^*(t)\sin\theta & b_z & \frac{1}{\sqrt{2}}(b_x - ib_y) & 0 \\ \frac{1}{2\sqrt{3}}\tilde{\Omega}^*(t)\cos\theta & \frac{1}{\sqrt{2}}(b_x + ib_y) & 0 & \frac{1}{\sqrt{2}}(b_x - ib_y) \\ \frac{i}{2\sqrt{6}}\tilde{\Omega}^*(t)\sin\theta & 0 & \frac{1}{\sqrt{2}}(b_x + ib_y) & -b_z \end{pmatrix} \quad (6.18)$$

where $\tilde{\Omega}(t) = \Omega_1 e^{i\Delta_1 t} + \Omega_2 e^{i\Delta_2 t}$, with Δ_1 and Δ_2 denote frequency detunings from the optical transition frequency ω_0 . We can use this Hamiltonian to numerically calculate fluorescence and investigate the effects of B-field components B_x and B_y .

6.3 Calculating atomic fluorescence

From the time-dependent Hamiltonian (6.18), we can calculate the density matrix $\tilde{\rho}$ in the rotating frame.

$$\dot{\tilde{\rho}}(t) = -\frac{i}{\hbar}[\tilde{H}(t), \tilde{\rho}(t)] + \frac{1}{2} \sum_{m_J} [2C_{m_J}\tilde{\rho}(t)C_{m_J}^\dagger - \tilde{\rho}(t)C_{m_J}^\dagger C_{m_J} - C_{m_J}^\dagger C_{m_J}\tilde{\rho}(t)] \quad (6.19)$$

where $C_{m_J} = \sqrt{\gamma}|g\rangle\langle e_{m_J}|$ is a collapse operator representing spontaneous decays from any of the excited $|e_{m_J}\rangle$ to the ground state, with $\gamma = 2\pi \times 182$ kHz. With the QuTiP package [115, 116] in Python, I solve the Linblad Master Equation numerically for the density matrix $\tilde{\rho}(t)$ and then estimate the steady-state solution by averaging $\tilde{\rho}(t)$ for $t > 10/\gamma$.

We can then calculate the fluorescence from the density matrix. Total atomic fluorescence is proportional to the total excited-state population $\rho_e = \rho_{11} + \rho_{22} + \rho_{33} = \tilde{\rho}_{11} + \tilde{\rho}_{22} + \tilde{\rho}_{33}$, invariant under the unitary transformation. Starting from the baseline

model, $b_x = b_y = 0$ and $\theta = 90^\circ$ (y-polarization), the Hamiltonian \tilde{H}_θ reduces to

$$\tilde{H}_y = \hbar \begin{pmatrix} 0 & -\frac{i}{2\sqrt{6}}\tilde{\Omega}(t) & 0 & -\frac{i}{2\sqrt{6}}\tilde{\Omega}(t) \\ \frac{i}{2\sqrt{6}}\tilde{\Omega}^*(t) & b_z & 0 & 0 \\ 0 & 0 & 0 & 0 \\ \frac{i}{2\sqrt{6}}\tilde{\Omega}^*(t) & 0 & 0 & -b_z \end{pmatrix} \quad (6.20)$$

where $\tilde{\Omega}(t) = \Omega_1 e^{i\Delta_1 t} + \Omega_2 e^{i\Delta_2 t}$. In the case where the two laser fields correspond to two first-harmonic sidebands of the square-wave AM light, assume $\Omega_1 = \Omega_2 = \Omega$ and the detunings are set to $\Delta_1 = \delta_{mod}$ and $\Delta_2 = -\delta_{mod}$. We can then solve the Master equation and calculate fluorescence for different values of $b_z = \frac{g\mu_B}{\hbar}B$.

6.3.1 Autler-Townes splitting

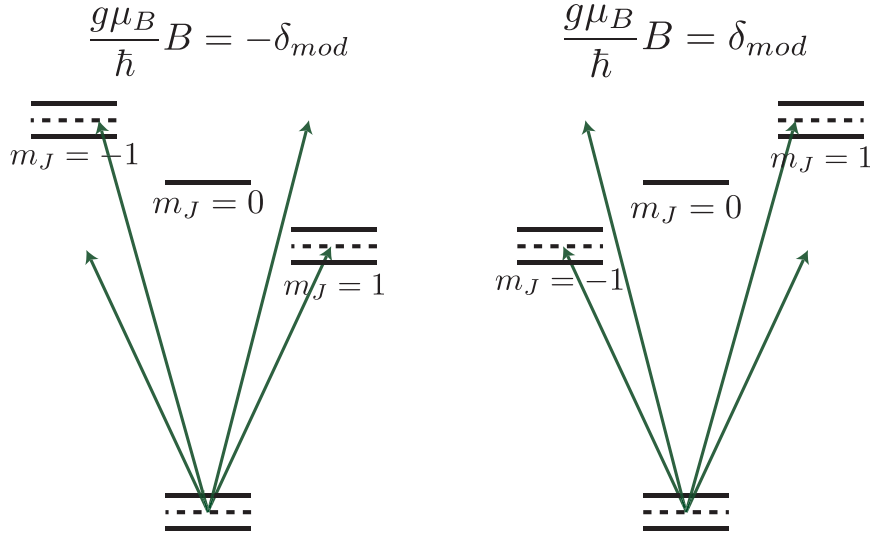


Figure 6.3: Autler-Townes splitting occurs when $\frac{g\mu_B}{\hbar}B = \delta_{mod}$ (and by symmetry, when the magnetic field sign is reversed, $\frac{g\mu_B}{\hbar}B = -\delta_{mod}$)

As illustrated in Fig. 6.3, when $b_z = \frac{g\mu_B}{\hbar}B = \pm\delta_{mod}$, both laser fields are simultaneously in resonance with the $m_J = \pm 1$ excited states. Strong-field AC Stark effects cause the ground state and both $m_J = \pm 1$ excited states to split, resulting in

a decrease in both fluorescence and absorption. This “dark” resonance is known as Autler-Townes (AT) splitting [53]. The frequency splitting is equal to the Rabi frequency Ω of the driving field, so the splitting is observable when the system is driven by strong fields. AT splitting produces a double-Lorentzian lineshape in Doppler-free fluorescence and absorption spectra. With the current system’s Hamiltonian \tilde{H}_y , numerically calculated fluorescence as a function of $b_z = \frac{g\mu_B}{\hbar}B_z$ is shown in Fig. 6.4 below.

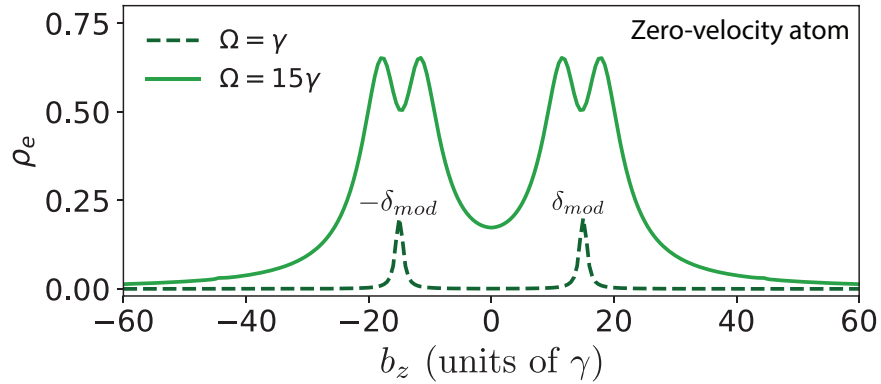


Figure 6.4: Total excited-state population (proportional to total emitted fluorescence) as a function of the Zeeman shift $b_z = \frac{g\mu_B}{\hbar}B_z$ at Rabi frequencies $\Omega_1 = \Omega_2 = \Omega = \gamma$ (weak field, dashed line) and 15γ (strong field, solid line) and modulation frequency $\delta_{mod} = 15\gamma$, which set the field detunings to $\pm 15\gamma$. As expected, the plot shows two resonances at $b_z = \pm 15\gamma = \pm \delta_{mod}$ and AT splitting is only observed in the strong field case ($\Omega = 15\gamma$).

Figure 6.4 shows a plot of total excited-state population $\rho_e = \rho_{11} + \rho_{22} + \rho_{33}$ as a function of the Zeeman shift $b_z = \frac{g\mu_B}{\hbar}B_z$ for a weak-field case ($\Omega = \gamma$) and a strong-field case ($\Omega = 15\gamma$). In the weak-field case (dashed line), there are two Lorentzian peaks centered at $b_z = \pm 15\gamma$, where the two driving fields are in resonance with the $m_J = \pm 1$ excited states. In the strong-field case (solid line), the peaks split into doublets, producing two dark resonances centered at $b_z = \pm 15\gamma = \pm \delta_{mod}$ as expected. The dark resonances due to Autler-Townes splitting have given us a glimpse of how the fluorescence is darker at specific regions in a magnetic field gradient. However, without Doppler shifts included, the lineshape depicted in Fig. 6.4 is not representative of what we would observe from hot, moving Yb atoms in our experiment.

The next step in improving this model is to incorporate Doppler broadening in our calculation.

6.3.2 Doppler broadening

To account for Doppler shifts from moving atoms in our experiment, we sample transverse velocities v_x from a Gaussian distribution with the velocity width $\sigma = 4.5$ m/s and compute an average excited-state population $\bar{\rho}_e$ from $N = 1000$ or more atom samples. The velocity width $\sigma = 4.5$ m/s is estimated from the width of the longitudinal velocity (from effusion velocity distribution at the temperature of $450^\circ C$) multiplied with the AOSense atomic beam divergence (half-angle of divergence ≈ 17 mrad from the AOSense operating manual). A histogram of 1000 v_x samples is shown in Fig. 6.5. At each sampled velocity v_x , the field detunings become $\Delta_{1,2} \rightarrow \Delta_{1,2} - \vec{k} \cdot \vec{v} = \Delta_{1,2} - kv_x$, where k is the laser's wavenumber.

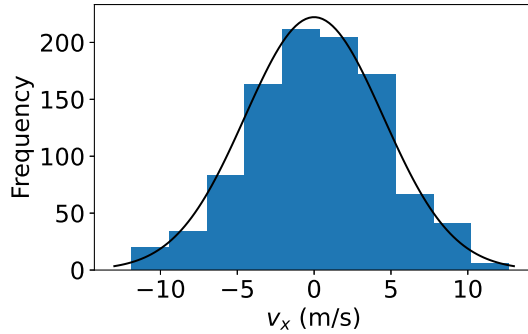


Figure 6.5: Histogram of atoms' transverse velocities v_x ($N = 1000$) from a Gaussian velocity distribution with velocity width $\sigma = 4.5$ m/s.

The bottom (green) curve in Fig. 6.6 represents the Doppler-averaged excited-state population $\bar{\rho}_e$ (with a semi-transparent standard error band given by $\sqrt{\frac{\bar{\rho}_e(1-\bar{\rho}_e)}{N}}$ for N atoms) for $\Omega = 15\gamma$ and $\delta_{mod} = 15\gamma$. As before, only two laser frequencies are present at detunings $\pm\delta_{mod}$ in the baseline model with the magnetic field along the z -direction. With Doppler broadening, the green curve shows three prominent dips at $b_z = \frac{g\mu_B}{\hbar}B = -\delta_{mod}, 0, \delta_{mod}$. This suggests that, in a magnetic field gradient,

fluorescence would appear dark where the magnetic field satisfies these dark-resonance conditions.

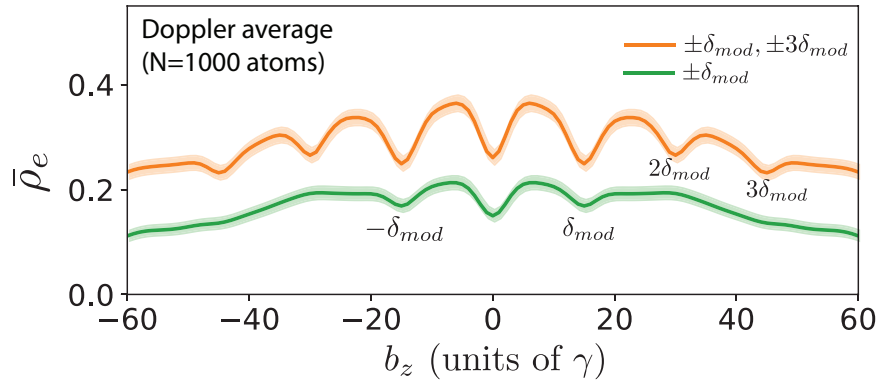


Figure 6.6: Doppler averaged excited-state population $\bar{\rho}_e$ as a function of $b_z = g\mu_B B$. Modulation frequency $\delta_{mod} = 15\gamma$ and Rabi frequency in each sideband $\Omega = 15\gamma$.

6.3.3 Adding more fields

So far, the model includes only the first harmonic sidebands at detunings $\pm\delta_{mod}$ whereas the experiment utilizes a large number of sidebands of a square wave. In theory, including more fields at different frequencies would produce additional dark lines. This is because any pair of laser frequencies with a frequency difference $\Delta\nu$ produces a dark resonance where $b_z = g\mu_B B = \Delta\nu/2$ (with $\Delta\nu = 2\delta_{mod}$ for the first-harmonic sidebands at $\omega_0 \pm \delta_{mod}$).

We can include in the model, for example, two additional fields at frequencies $\omega_0 \pm 3\delta_{mod}$. The top (orange) curve in Fig. 6.6 shows additional dips at $b_z = \pm 2\delta_{mod}$ and $b_z = \pm 3\delta_{mod}$. These extra dips arise from additional frequency differences as $\Delta\nu$ between any frequency pairs can be $2\delta_{mod}$, $4\delta_{mod}$ or $6\delta_{mod}$. I used the same Rabi frequency $\Omega = 15\gamma$ for all the four fields (detunings of $\pm\delta_{mod}$ and $\pm 3\delta_{mod}$) in this calculation. In general, having more sideband frequencies produce more dark lines

that we can observe, which makes mapping the magnetic-field gradient more efficient.

6.4 Hanle effect: light emitted along y

So far, we have used the total excited-state population $\rho_e = \rho_{11} + \rho_{22} + \rho_{33}$ to represent the atomic fluorescence. However, in the experiment, the camera is located directly above the interaction region and primarily collects light emitted vertically (along the y -direction). The spatial distribution of the dipole radiation in magnetic fields must be included in the model to realistically simulate the fluorescence observed by the camera. The following derivation of the intensity of light emitted vertically (along the y -direction) is adapted from the supplemental material of Jackson & Durfee (2019) [172].

The intensity of light emitted along the y -direction consists of z -polarized light emitted by the $m_J = 0$ excited state, with intensity proportional to $|A_0|^2$, and light emitted by the $m_J = \pm 1$ excited states. In our setup, light emitted by the $m_J = \pm 1$ excited states can be decomposed into the y -polarized portion with intensity proportional to $\frac{1}{2}|A_1 + A_{-1}|^2$ and the z -polarized portion with intensity proportional to $\frac{1}{2}|A_1 - A_{-1}|^2$, where A_1 and A_{-1} are the amplitudes defined in (6.8). Assuming the camera only sees light emitted in the y direction, the y -polarized portion of the fluorescence will not be observed. The total observed intensity I_y , accounting for the directional Hanle effect, is a combination of the z -polarized light emitted from the excited states and is proportional to

$$\begin{aligned} I_y &\propto \frac{1}{2}|A_1 - A_{-1}|^2 + |A_0|^2 = \frac{1}{2}(\rho_{11} + \rho_{33} - (\rho_{13} + \rho_{31})) + \rho_{22} \\ &= \frac{1}{2}(\tilde{\rho}_{11} + \tilde{\rho}_{33} - (\tilde{\rho}_{13} + \tilde{\rho}_{31})) + \tilde{\rho}_{22} \end{aligned}$$

which is also invariant under the unitary transformation and can be calculated directly from the density matrix elements.

One major difference we expect is the light intensity at zero magnetic fields. With y -polarized light, and without magnetic fields, atoms' electric dipoles would be oriented vertically along the y direction such that the camera looking down the

y -axis would not see any light according to the dipole radiation pattern. Non-zero B-fields along the z direction (perpendicular to the original laser polarization) cause the dipoles to precess about the z -axis. The dipole radiation pattern is tilted and no longer oriented along the y -axis, resulting in some fluorescence light being able to reach the camera. At $b_z \neq 0$, we expect the fluorescence emitted along y to be about half of the total fluorescence, but the spatial Hanle effect should not affect the dark lines at non-zero B-fields significantly because the precession is rapid.

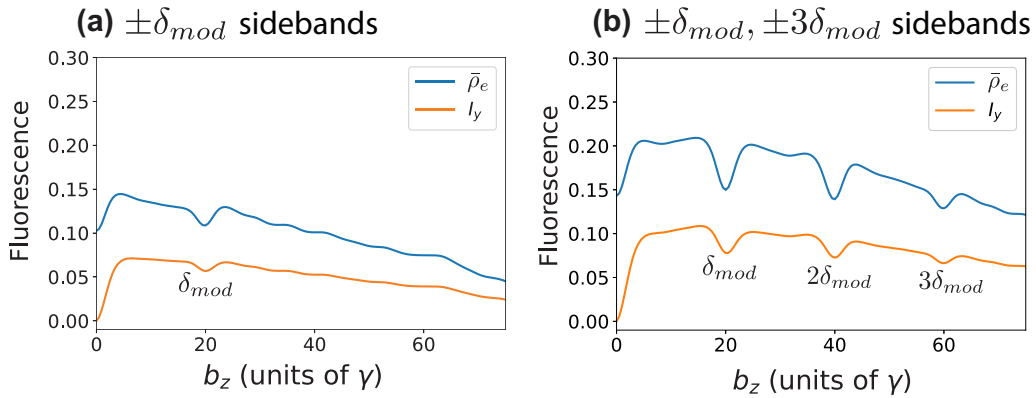


Figure 6.7: Doppler averaged excited-state population $\bar{\rho}_e$ (blue curve) representing total fluorescence and $I_y = \frac{1}{2}(\rho_{11} + \rho_{33} - (\rho_{13} + \rho_{31})) + \rho_{22}$ (orange curve) representing fluorescence emitted along the y -axis taking into account Autler-Townes and the spatial Hanle effects for $\delta_{mod} = 20\gamma$ and Rabi frequency $\Omega = 10\gamma$ in each sideband. The left plot (a) includes only the fields at detunings $\pm\delta_{mod}$. The right plot (b) has additional sidebands at $\pm 3\delta_{mod}$, which produce additional dips at $b_z = 2\delta_{mod}$ and $3\delta_{mod}$. In both plots, the Hanle effect (orange) makes the fluorescence go to zero where there is zero magnetic field $b_z = 0$.

Figure 6.7 shows the Doppler-averaged total excited-state population $\bar{\rho}_e = \rho_{11} + \rho_{22} + \rho_{33}$, which is proportional to total emitted fluorescence and Doppler-averaged $I_y = \frac{1}{2}(\rho_{11} + \rho_{33} - (\rho_{13} + \rho_{31})) + \rho_{22}$, which is proportional to the intensity of light emitted along the y -axis and would be collected by the camera in the experiment. The magnitude of I_y is approximately half of that of $\bar{\rho}_e$ everywhere except where the magnetic field is zero $b_z = 0$. At zero B-field, $I_y = 0$ is expected because with the

driving laser fields linearly polarized along y , the dipole radiation pattern is oriented along y , producing no fluorescence along the y -axis. For $b_z \neq 0$, a non-zero magnetic field along the z -direction causes the electric dipole to precess and as a result, emit light along y .

The Hanle effect does not affect the positions of the fluorescence dips due to Autler-Townes splitting at non-zero B-fields. Figure 6.7a shows dark lines at $b_z = \delta_{mod}$, where the two light fields at detunings $\pm\delta_{mod}$ are simultaneously in resonance with the $m_J = \pm 1$ states. Adding additional laser fields at detunings $\pm 3\delta_{mod}$ introduce additional dips at $b_z = 2\delta_{mod}$ and $3\delta_{mod}$, as depicted in Fig. 6.7b. In the next chapter, I will show that the model results with the Hanle effect included show better agreement with our experimental results.

6.5 Summary

Thus far, we have built a numerical model that describes a 4-level atom (with $J = 1$ excited state and $J = 0$ ground state) driven by two or more strong laser fields. The baseline model assumes two driving fields at detunings $\pm\delta_{mod}$ from the $m_J = 0$ excited state, linearly polarized along the y -direction, and a magnetic field along the z -direction. The laser fields driving σ^+ and σ^- transitions effectively form a V-system, which allows for Autler-Townes splitting to occur where $|b_z| = \frac{g\mu_B}{\hbar}|B| = \delta_{mod}$. With the baseline model, we numerically calculated Doppler-free fluorescence followed by Doppler-averaged fluorescence from the transverse motion of atoms. We also incorporated the spatial Hanle effect to better estimate the fluorescence pattern observed by the camera that primarily collects light along the y -axis.

The next chapter will focus on comparisons between the theory and the experiment. To better simulate the experiment, more sidebands are added and we need to extend the model beyond magnetic fields in one dimension. We will discuss the laser polarization dependence as well as how off-axis magnetic fields B_x, B_y affect the dark lines.

Chapter 7

Beyond the 1D model: vector magnetometer

7.1 Introduction

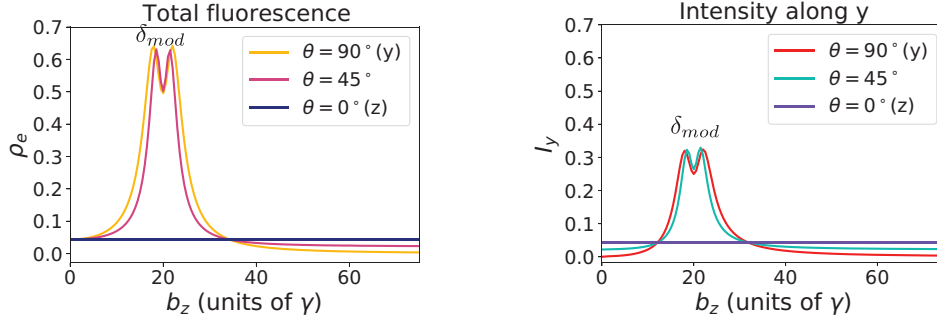
Based on the numerical model we derived in the previous chapter, this chapter extends the model to investigate how the fluorescence pattern changes with the laser polarization (polarization angle $0 \leq \theta \leq 90^\circ$) and when the magnetic fields are no longer assumed to be perfectly along the z -axis.

7.2 Polarization dependence

Figure 7.1 shows the total fluorescence (left column) and intensity of light emitted along the y -axis (right column) as a function of the Zeeman shift due to magnetic fields along the z -axis $b_z = \frac{g\mu_B}{\hbar}B_z$. Only two light fields at detunings $\omega_0 \pm \delta_{mod}$ and Rabi frequencies $\Omega_1 = \Omega_2 = 10\gamma$ are included in this calculation.

For a zero-velocity atom, Fig. 7.1a (top row) shows a double-Lorentzian lineshape due to Autler-Townes splitting centered at $b_z = \delta_{mod} = 20\gamma$ when $\theta = 90^\circ$ (as before) and $\theta = 45^\circ$. In general when $\theta \neq 90^\circ$, the laser polarization is no longer perpendicular to the chosen quantization axis along z . The laser fields now have a polarization component along the z -axis, which allows π transitions from the ground

(a) Zero-velocity atom



(b) Doppler-averaged (N=1000)

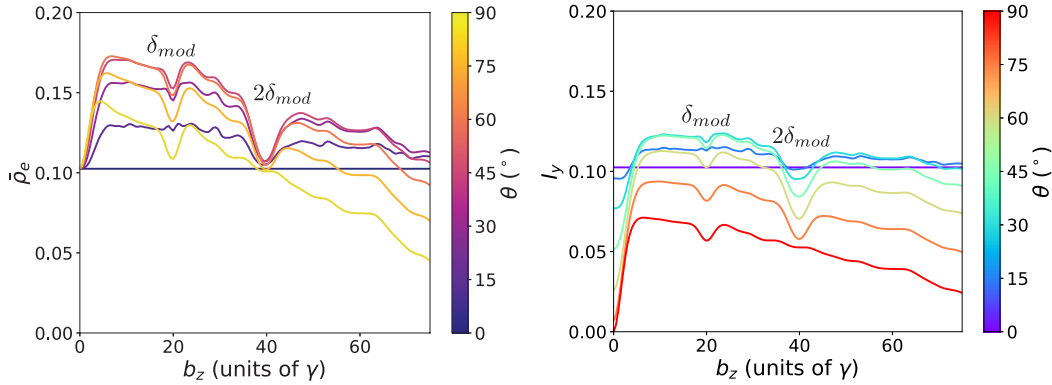


Figure 7.1: Polarization dependence: fluorescence as a function of Zeeman splitting $b_z = \frac{g\mu_B}{\hbar} B_z$ (a) for a zero-velocity atom and (b) Doppler broadened fluorescence (averaged over $N = 1000$ atoms) at polarization angles $0^\circ \leq \theta \leq 90^\circ$. Assume two light fields at detunings $\pm\delta_{mod} = \pm20\gamma$ and Rabi frequencies $\Omega_1 = \Omega_2 = 10\gamma$. Both plots on the left column represent the total excited-state population (proportional to total fluorescence), whereas the plots on the right column represent the intensity emitted along the y -direction, which would be collected by the camera, calculated with the Hanle effect incorporated.

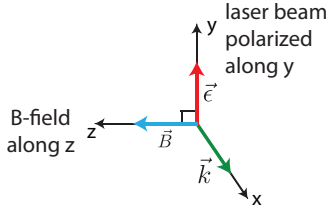
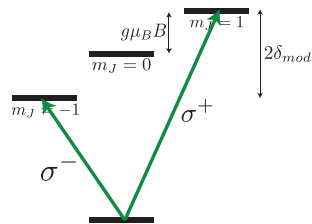
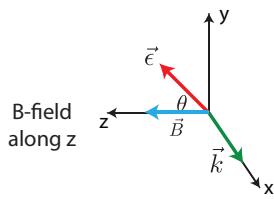
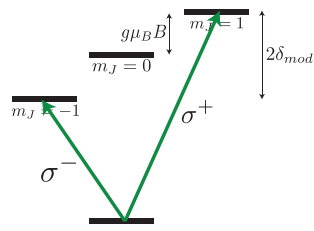
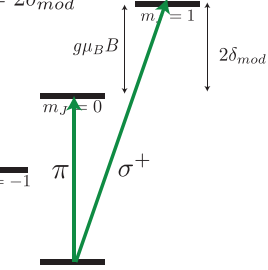
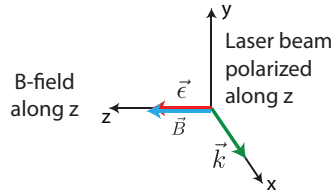
state to the $m_J = 0$ state in addition to the combination of σ^\pm transitions that can produce Autler-Townes splitting. Hence, at $\theta = 45^\circ$, half the laser power is driving the π transitions to the $m_J = 0$ state and only the other half is driving the σ^\pm transitions that produce a dark resonance at $b_z = \delta_{mod} = 20\gamma$. This explains why the doublet becomes narrower due to less power broadening at $\theta = 45^\circ$.

On the other hand, the doublet completely disappears at $\theta = 0^\circ$ (laser linearly

polarized along the z -axis). At this polarization, only π transitions from the ground state to the $m_J = 0$ state are allowed and the $m_J = 0$ state does not shift in the magnetic field. Hence, the fluorescence from the $m_J = 0$ state is constant for any B-field values. The ground state and the $m_J = 0$ excited state still experience Autler-Townes splitting, but with only one field interacting with the states (no V-system), the total fluorescence does not have a dark resonance.

With Doppler broadening from the atoms' transverse motion, the Doppler-averaged fluorescence plots in Fig. 7.1b tell a similar story but with an additional feature at $b_z = 2\delta_{mod} = 40\gamma$. The major difference here is that in the Doppler-free case (a), the light field detunings $\pm\delta_{mod}$ keep the fields off-resonance from the $m_J = 0$ state regardless of the magnetic field b_z and hence there is barely any fluorescence from $m_J = 0$ atoms. In contrast, with Doppler broadening (b), a combination of a π and either a σ^+ or σ^- transition can also produce Autler-Townes splitting. As illustrated in Fig. 7.2b, when all three types of transitions are allowed, in addition to the dark resonance from the σ^\pm transitions ($b_z = \frac{g\mu_B}{\hbar}B = \delta_{mod}$), there can be an additional dark resonance at $b_z = 2\delta_{mod}$ for atoms in some velocity classes. This results in additional dips in the fluorescence plots at $b_z = 2\delta_{mod}$ when $0^\circ < \theta < 90^\circ$. When $\theta = 0^\circ$ (polarization along z), only π transitions are allowed and fluorescence remains unchanged with b_z as expected.

Similar to Fig. 6.7 from the previous chapter, both plots on the right represent the fluorescence that would be collected by the camera with the spatial Hanle effect accounted for. When the laser polarization is along the y -direction ($\theta = 90^\circ$, red curves in both top and bottom rows), intensity along y -direction, I_y , goes to zero at zero magnetic fields. As the polarization angle θ is rotated, the orientation of the atom's electric dipole rotates accordingly, which allows more light to reach the camera even when the magnetic fields remain zero. As the right plot of Fig. 7.1b shows, having $\theta < 90^\circ$ lifts the intensity minimum from zero and also increases the overall amount of fluorescence observed (all non-red curves are above the red curve). The contrast of other dark lines at $b_z = \delta_{mod}$ and $b_z = 2\delta_{mod}$ also changes with θ for the same reasons described earlier. Changing θ changes the fraction of optical power that produces the dark resonances (from σ^\pm transitions) vs. the amount of power

(a) $\theta = 90^\circ$ Dark resonance at $g\mu_B|B| = \delta_{mod}$ (b) $0^\circ < \theta < 90^\circ$ Dark resonance at
 $g\mu_B|B| = \delta_{mod}$ Dark resonance at
 $g\mu_B|B| = 2\delta_{mod}$ (c) $\theta = 0^\circ$ 

No dark resonance

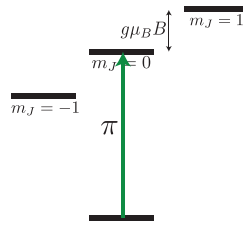


Figure 7.2: How does θ affect the dark resonances? (a) $\theta = 90^\circ$: σ^\pm transitions produce a dark resonance at $b_z = \delta_{mod}$. (b) $0^\circ < \theta < 90^\circ$: π transitions are also allowed, hence there are two dark resonances at $b_z = \delta_{mod}, 2\delta_{mod}$. (c) No dark resonance at $\theta = 0^\circ$.

that drives the π transition.

Overall, Figs. 7.1 and 7.2 illustrate the effects of polarization direction on the observed fluorescence due to the different types of transitions allowed. The next question we are interested in exploring is how B-field components that are not along the main axis z affect the fluorescence pattern.

7.3 Non-zero B_x and B_y components

In our lab, background magnetic fields including the Earth's field (≈ 0.5 G) and the permanent magnet in our AOSENSE Zeeman slower can affect the fluorescence images. Because the Earth's field is primarily oriented in the xy -plane in our coordinate system, it is important to understand how non-zero B_x and B_y components affect the fluorescence.

The figures in this section were produced by the numerical model that includes one additional light field at ω_0 , making a total of three strong driving fields at frequencies: $\omega_0 - \delta_{mod}$, ω_0 and $\omega_0 + \delta_{mod}$. The light field at ω_0 was added to better mimic the square-wave amplitude-modulated light. In our experiment, the amplitude modulation is produced by an Acousto-Optic Modulator (AOM) that chops the beam on and off at the modulation frequency δ_{mod} that is in the 100 kHz \rightarrow 10 MHz range. At 10% duty cycle (achievable up to ~ 3 MHz with our current AOM), there is significant laser power in the carrier. More details on the modulation and frequency sidebands present are given in Sec. 8.2.

The next chapter discusses the frequency components present in more detail but here, for simplicity, we assume here that the three light fields have the same Rabi frequency $\Omega = 10\gamma$. Any two (out of three) frequencies present can produce Autler-Townes splitting. The frequency difference between two fields can be either δ_{mod} or $2\delta_{mod}$, so we expect dark resonances where $2\frac{g\mu_B}{\hbar}|B| = \delta_{mod}, 2\delta_{mod}$, i.e.,

$$b = \frac{g\mu_B}{\hbar}|B| = \frac{1}{2}\delta_{mod}, \delta_{mod}. \quad (7.1)$$

7.3.1 Non-zero B_y

In our setup, the laser polarization can be rotated in the yz plane. So far, we have assumed the polarization to be vertical, along the y -axis, making it perpendicular to the primary magnetic field along z . Adding non-zero B_y effectively produces a net magnetic field in the yz plane but the vector \vec{B} is no longer perpendicular to the laser polarization.

We can visualize the effects of B_y by plotting a 2D map of fluorescence as a

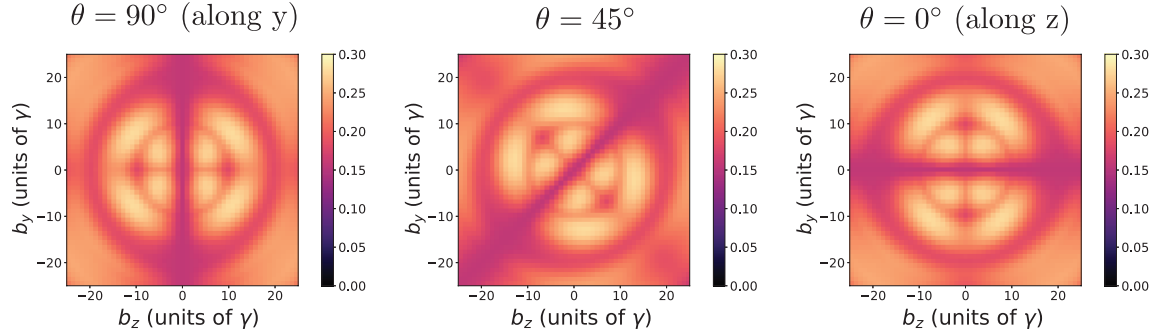
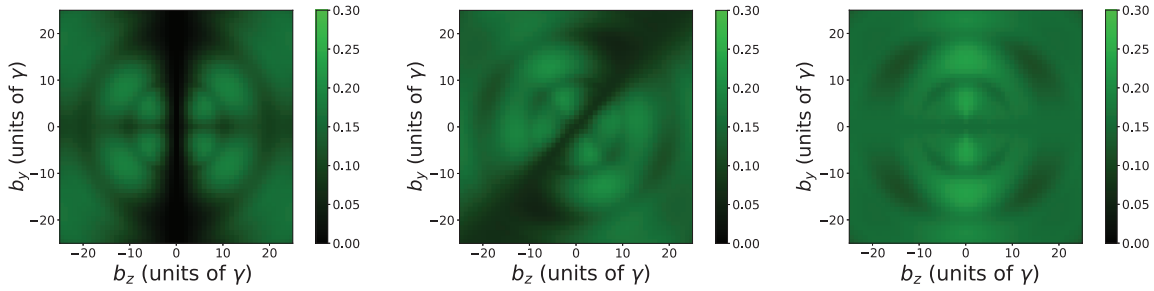
(a) Total fluorescence (b_y , b_z)(b) Fluorescence along y 

Figure 7.3: (a) Total fluorescence and (b) intensity emitted along the y -axis as a function of (b_y, b_z) at polarization angles $\theta = 90^\circ, 45^\circ$ and 0° . The fluorescence intensity is calculated from the Doppler averaged excited-state population, which can have values between 0 and 1. For illustration and direct comparison, the color scales run from 0 to 0.3 for all plots. There are linear gradients in both b_y and b_z in these plots, so these fluorescence patterns (in some cases) can correspond to the magnetic field contours in the yz plane. Because we are imaging in the xz plane, we are unlikely to observe these directly in the experiments.

function of $b_y = \frac{g\mu_B}{\hbar}B_y$ and $b_z = \frac{g\mu_B}{\hbar}B_z$, as shown in Fig. 7.3. The top row shows Doppler-averaged total excited-state population $\bar{\rho}_e$, and the bottom row represents the intensity of light emitted along the y -axis, I_y , taking into account the Hanle effect. The circular contours correspond to the dark resonance condition $b = \frac{g\mu_B}{\hbar}|B| = \frac{1}{2}\delta_{mod}$, δ_{mod} . Hence, $\delta_{mod} = 20\gamma$ produces two circular contours with radii of 10γ and 20γ , respectively.

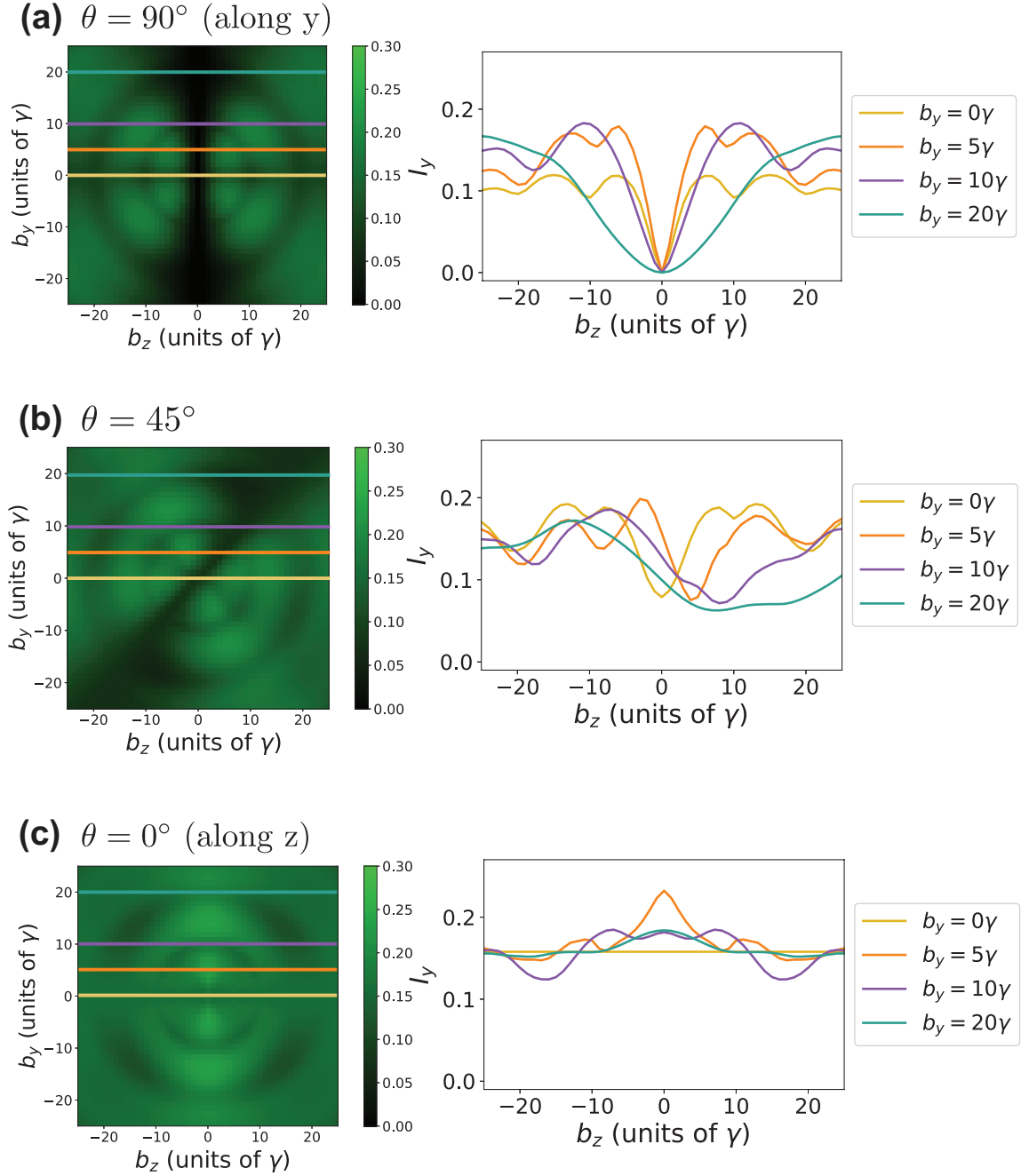


Figure 7.4: Intensity cross sections (of fluorescence light emitted along y) at polarization angles $\theta = 90^\circ, 45^\circ$ and 0° , representing how the fluorescence profile in a b_z gradient changes with different values of $b_y = 0, 5\gamma, 10\gamma, 20\gamma$.

In the 2D (b_y, b_z) picture, the total fluorescence $\bar{\rho}_e$ pattern rotates with the polarization angle. The prominent dark diameter that rotates with θ corresponds to the polarization direction, showing that the fluorescence remains unchanged when the polarization direction is parallel to the B-field (consistent with earlier results when $\theta = 0^\circ$). With the spatial Hanle effect incorporated, the fluorescence that would be observed by the camera down the y -axis looks slightly different depending on the laser polarization angle θ , which defines the orientation of the dipole radiation.

Since our system is primarily used for imaging of B_z gradients, we can plot horizontal cross-sections of Fig. 7.3b to visualize how B_y affects the dark resonances. Examples of the cross-sections are shown in Fig. 7.4. Note that $b_y = 5\gamma, 10\gamma, 20\gamma$ correspond to the magnetic field strengths of $B_y = 0.43, 0.86, 1.7$ G, respectively.

Because we mostly use $\theta = 90^\circ$ (y -polarized light) in our experiment, intensity cross sections in Fig. 7.4a very closely correspond to the fluorescence pattern we may observe in a B-field gradient along z with non-zero B_y present. The yellow curve on the right (with $b_y = 0$) shows an intensity minimum at $b_z = 0$ and additional dips at $b_z = \pm 10\gamma, \pm 20\gamma$ as expected for modulation frequency $\delta_{mod} = 20\gamma$. Adding a small $b_y = 5\gamma$ ($B_y \approx 0.43$ G), the light green curve shows that the dips at $b_z = \pm 10\gamma, \pm 20\gamma$ seem to shift slightly inwards and the contrasts become uneven. At $b_y = 10\gamma$ (dark green curve), the central minimum at $b_z = 0$ becomes broader and the first-order dips at $\delta_{mod} = 10\gamma$ disappear completely. This helps us later account for missing dips from the experimental data in Sec. 8.3 in the next chapter.

At $\theta = 45^\circ$, as depicted in Fig. 7.4b, the fluorescence pattern appears to be rotated by 45° as the laser polarization is rotated. This produces apparent lateral shifts in the central minimum and distortion on other dark lines. This spatial shift in the central minimum was observed experimentally as shown later in Sec. 7.4. The minimum no longer corresponds to $b_z = 0$ at this polarization setting, but for small b_y , the fluorescence is the darkest (but non-zero) where $b_y = b_z$.

At $\theta = 0^\circ$ (z-polarized light), there is no obvious diagonal direction along which the fluorescence is the darkest. This is mainly due to the spatial Hanle effect. With the z-polarized light, the electric dipole orientation is now perpendicular to the y -direction along which the camera is collecting light, so the dark-line contrast is the

lowest in this orientation. There are still circular contours that correspond to where $b_y^2 + b_z^2 = \delta_{mod}/2, \delta_{mod}$. As a result, the intensity cross-sections contain shallow dips for the several values of b_y we plotted. Remarkably and understandably so, instead of a dark line at $b_z = 0$, the fluorescence becomes bright at non-zero b_y . This was also observed in the experimental data in Sec. 7.4.

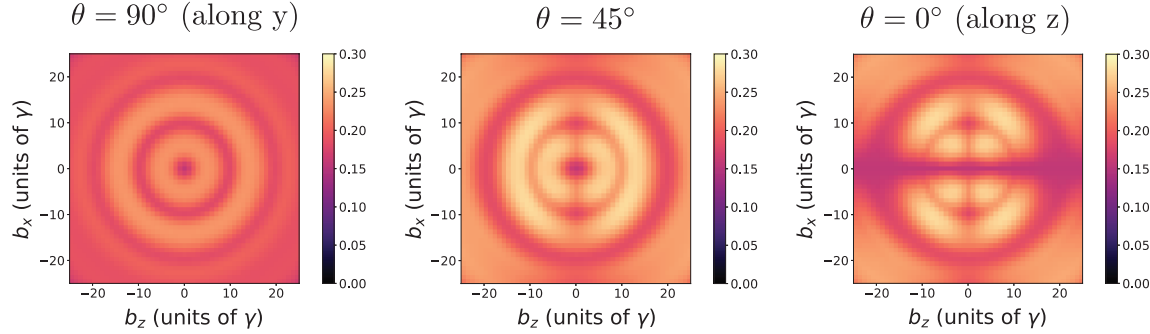
Overall, non-zero B_y can account for the following features: missing dark lines where $\frac{g\mu_B}{\hbar}|B| = \delta_{mod}/2$, spatial shifts in the central minimum, and “bright” fluorescence where the central minimum is without B_y (in this case there is no location where $|B| = 0$).

7.3.2 Non-zero B_x

Instead of adding non-zero y -component of the magnetic field, we can plot equivalent (b_x, b_z) contours. The major difference here is that B_x is not in the laser polarization plane, so the fluorescence pattern does not show clear a rotation trend that directly corresponds to θ , as shown in Fig. 7.5. Same as before, the top row shows Doppler-averaged total excited-state population $\bar{\rho}_e$, and the bottom row represents the intensity of light emitted along the y -axis, I_y , taking into account the spatial Hanle effect. The circular contours still correspond to the dark resonance condition $b = \frac{g\mu_B}{\hbar}|B| = \frac{1}{2}\delta_{mod}, \delta_{mod}$ but with $|B| = \sqrt{B_x^2 + B_z^2}$. Hence, $\delta_{mod} = 20\gamma$ produces two circular contours with radii of 10γ and 20γ , respectively.

At $\theta = 90^\circ$ (y -polarized light, left panel), the contours appear perfectly circular with a dark spot in the center where $b_x = b_z = 0$. Because both x - and z -components of the magnetic fields are perpendicular to the laser polarization, adding non-zero b_x does not introduce any π -transitions to the $m_J = 0$ state. Hence there is no diagonal direction along which the fluorescence is constant or darker than others.

At $\theta = 0^\circ$ (right panel), the total fluorescence contour (top row of Fig. 7.5) is the same as the respective (b_y, b_z) contour shown earlier in Fig. 7.3a, showing a prominent dark diameter where $b_x = 0$ (or earlier, $b_y = 0$). With the Hanle effect (bottom row), the fluorescence pattern is darker near where $b_z = 0$, with the outer circular contour showing uneven contrast and appearing less dark away from the north and south

(a) Total fluorescence (b_x , b_z)

(b) Fluorescence along y

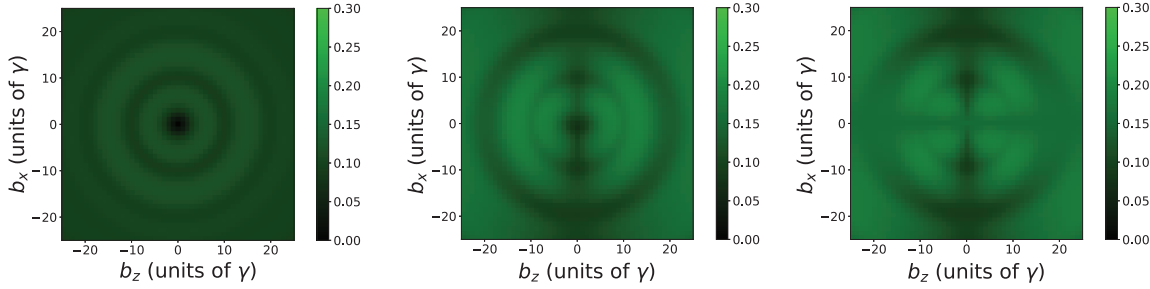


Figure 7.5: (a) Total fluorescence and (b) intensity emitted along the y -axis as a function of (b_x, b_z) at polarization angles $\theta = 90^\circ, 45^\circ$ and 0° . The fluorescence intensity is calculated from the Doppler averaged excited-state population, which can have values between 0 and 1. For illustration and direct comparison, the color scales run from 0 to 0.3 for all plots. There are linear gradients in both b_x and b_z in these plots, so these fluorescence patterns (in some cases) can correspond to the magnetic field contours in the xz plane, which can be observed directly in the experiments where we take fluorescence images of the xz plane.

poles.

Perhaps the least intuitive picture is when $\theta = 45^\circ$ (center). There is a hint of a “dark” north-south diameter, which becomes darker as $\theta \rightarrow 0^\circ$, suggesting that π -transitions are at play. Similar to what we did previously with the (b_y, b_z) contours, we can also plot horizontal cross-sections of Fig. 7.5b to visualize how B_x affects the dark resonances. Examples of the cross-sections are shown in Fig. 7.6. Note that $b_x = 5\gamma, 10\gamma, 20\gamma$ correspond to the magnetic field strengths of $B_x = 0.43, 0.86, 1.7$ G, respectively.

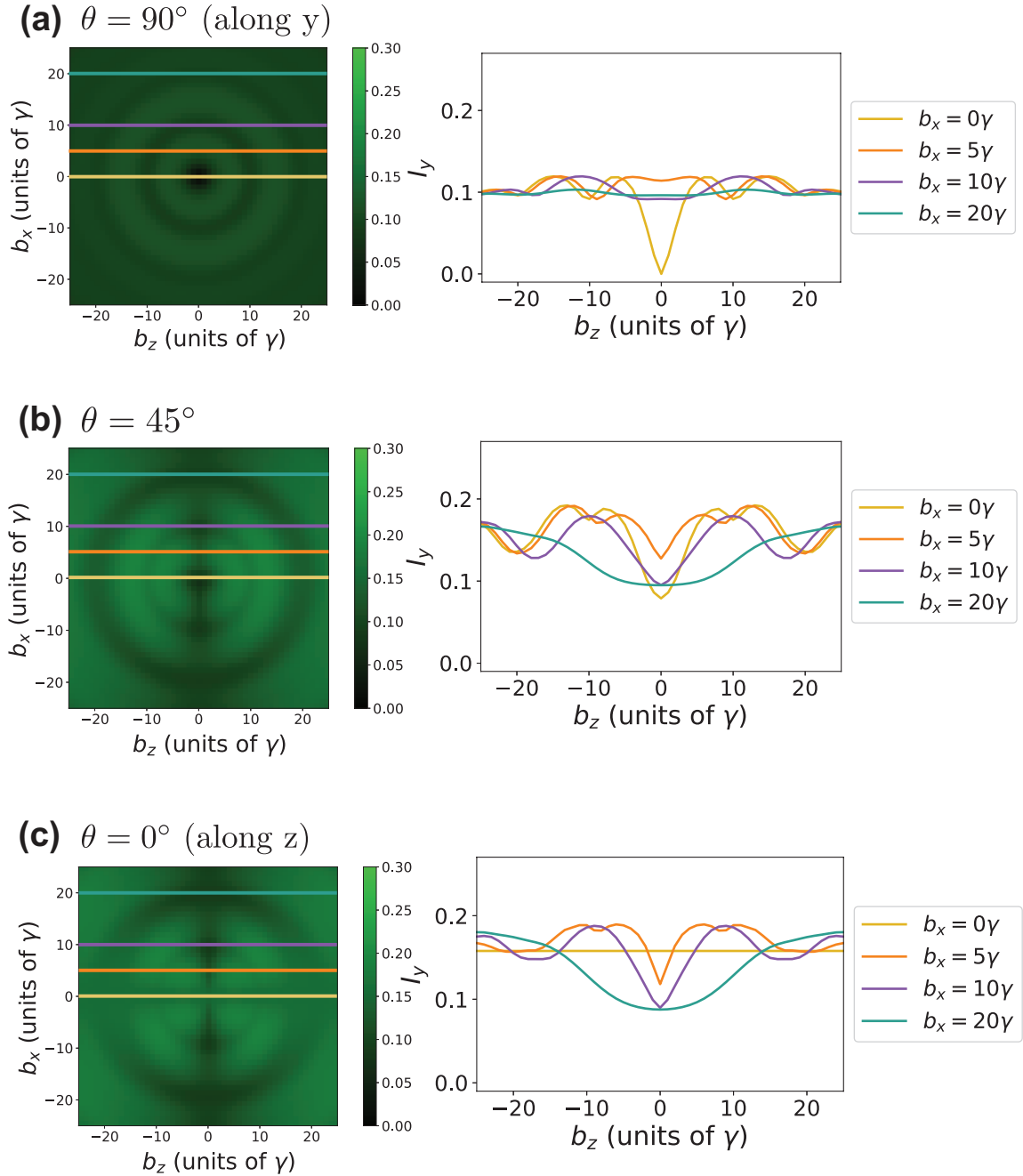


Figure 7.6: Intensity cross sections (of fluorescence light emitted along y) at polarization angles $\theta = 90^\circ, 45^\circ$ and 0° , representing how the fluorescence profile in a b_z gradient changes with different values of $b_x = 0, 5\gamma, 10\gamma, 20\gamma$.

From the $\theta = 90^\circ$ cross-sections in Fig. 7.6a, one of the most noticeable effects of adding non-zero b_x is the central minimum no longer at zero. At this polarization, adding non-zero b_y would not lift the minimum from zero. This allows us to infer b_x from the data, as illustrated and discussed later in Sec. 8.4.2 in the next chapter.

At $\theta = 45^\circ$ and 0° , the cross-sections turn out to be quite similar with the exception of the $b_x = 0$ curve (yellow curve) at $\theta = 0^\circ$ being completely flat. It is when all the fluorescence comes from the $m_J = 0$ state, which does not shift in the magnetic fields.

At all polarization settings, the circular nature of the contours causes some dark lines to shift slightly but the central minimum never does. This is another major difference between having non-zero b_x as opposed to b_y . This difference allows our magnetometer system to distinguish the effects of the two orthogonal components of the magnetic fields. Now that we know that the system is sensitive to polarization and B_x, B_y components, we can investigate these effects experimentally as follows.

7.4 Experimental data

My labmates Josh Tong and Mario Duenas built 3 additional pairs of Helmholtz coils around the imaging region in the experiment to cancel background magnetic fields. They adjusted the currents in the x and y Helmholtz coils until they saw a dark spot in the fluorescence that resembles a zero-field minimum. To rotate the laser polarization, a motorized half-wave plate (HWP) was rotated by 360° while recording a video with the camera to see how the fluorescence changed.

At the initial setting $\theta_{HWP} = 0^\circ$ (before any rotation), the laser polarization is set along the y -direction ($\theta = 90^\circ$). As the half-wave plate axis is rotated, the laser polarization θ changes by twice the HWP rotation amount. This means that every $\Delta\theta_{HWP} = 45^\circ$ on the half-wave plate is equivalent to 90° rotation on the polarization. From the initial position $\theta_{HWP} = 0^\circ \rightarrow 45^\circ$, the laser polarization is rotated from $\theta = 90^\circ$ (y -polarized light) to $\theta = 0^\circ$ (z -polarized light).

From one of the video datasets, extracting the first eighth frames ($45^\circ/360^\circ = 1/8$ of the total number of frames recorded in one full HWP rotation) and plotting the intensity cross-sections yield the results shown in Fig. 7.8a. 11 frames were taken

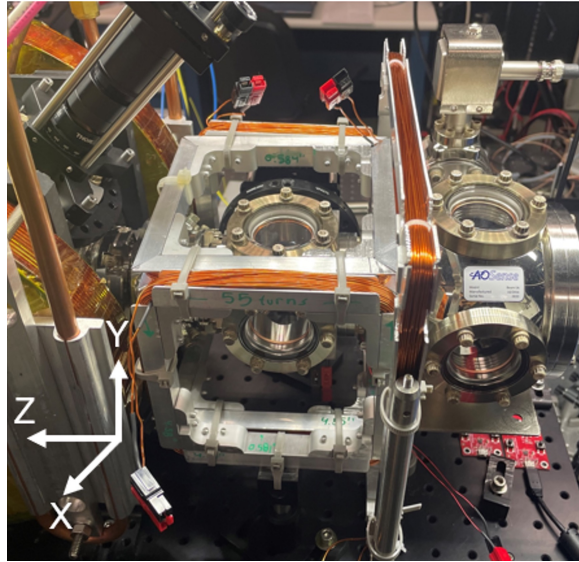


Figure 7.7: Compensation Helmholtz coils to cancel background magnetic fields (photo by Mario Duenas).

at evenly spaced time intervals corresponding to evenly spaced polarization angles between $0^\circ \leq \theta \leq 90^\circ$. From each frame, an intensity cross-section curve is plotted in different colors depending on θ . The color scale ranges from violet ($\theta = 0^\circ$) to red ($\theta = 90^\circ$).

Starting from a prominent dip in the red curve, this dip indicates that the magnetic field along z is zero at the fluorescence minimum. We can also infer that there must be a B_z gradient along the z -direction because the fluorescence is not uniformly dark. As the laser polarization θ changes, the dip (dark spot) gradually shifts to the left of the frame (by a few mm) with decreasing contrast. Eventually, this “dark” spot became even brighter than the background, as shown by the peak in the violet curve. Taking multiple cross-sections at different laser polarization directions provides more information and allows us to use these characteristics to estimate the residual B-fields (x and y components) by comparing the data to numerical calculations in Figs. 7.8b through 7.8e.

Figure 7.8b shows theoretical curves (calculated fluorescence emitted along the y direction) at different polarization angles θ if the magnetic fields were completely

canceled in both x and y directions, i.e., $B_x = B_y = 0$. At $\theta = 90^\circ$ (y -polarized light, red curve), we would expect zero fluorescence where the magnetic field is zero, then this minimum (dark spot) would gradually lose its contrast as θ decreases to zero. Without B_y , there is no spatial shift in the minimum (see Fig. 7.4b for example). At $\theta = 0^\circ$ (z -polarized light, violet curve), the intensity profile is completely flat, which is not what we observed in the experimental data in (a).

In Fig. 7.8c, $B_y = 0.1$ G was added to the model to produce the theoretical curves while B_x remains zero. The non-zero B_y introduces a spatial shift in the minimum. Note that the horizontal axes of the theoretical curves contain a negative sign $-b_z = -\frac{g\mu_B}{\hbar}B_z$. The negative sign in the z -gradient is used here for visualization purposes, such that the spatial shift occurs in the same direction as the data. Adding B_y also produces a bright peak in the center where $b_z = 0$ when $\theta = 0^\circ$, which is what we observed in the data in (a). Overall, the theoretical curves in (c) show good semi-quantitative agreement with the experimental data and capture important features including the spatial shift and the bright peak at $\theta = 0^\circ$.

By contrast, adding $B_x = 0.1$ G (keeping $B_y = 0$) in Fig. 7.8d produced different features from what was seen in the data. As illustrated earlier in Fig. 7.6, non-zero B_x lifts the minimum intensity above zero even at $\theta = 90^\circ$ (red curve). This can be understood via the spatial Hanle effect as magnetic fields in the x -direction cause precession of the atom's electric dipole such that it no longer aligns along the y -direction, allowing some emitted light to reach the camera. Similar to what was seen in panel (b), the contrast of the minimum decreases as $\theta \rightarrow 0^\circ$, but the main difference is that there is still a small dip in the violet curve instead of having a completely flat intensity profile.

The last setting presented here is when both B_x and B_y are non-zero. $B_x = B_y = 0.1$ G were used to produce the theoretical curves in Fig. 7.8e, where a combination of B_x and B_y features are present: spatial shift, brightness at $\theta = 0^\circ$, and a non-zero minimum at $\theta = 90^\circ$. One remarkable feature here is how the violet curve is no longer symmetrical around $b_z = 0$, which is a result of having non-zero B_x . This asymmetry becomes more significant at larger B_x values. In our experimental data (a), the “bright” peak at $\theta = 0^\circ$ looks almost perfectly symmetrical, so it is likely

that Josh and Mario successfully canceled nearly all of the background B_x .

From the model calculations and by exploring the parameter space of B_x and B_y , we conclude that $B_y = 0.10 \pm 0.02$ G ($B_x = 0$) produces fluorescence profiles that are the most similar to the experimental data. This data collection and forward simulation framework that takes advantage of variable laser polarization directions allows for the estimation of background or residual B_x and B_y . Currently, we do not fully understand the results at intermediate angles $0^\circ < \theta < 90^\circ$, so investigating these polarization trends and building better predictive models of B_x and B_y would be interesting future research directions to pursue. Note that this basic model assumes a linear B_z gradient along the z -direction, which may not be precisely true because of the close proximity of the Zeeman slower magnet to the observation region.

So far, this chapter and the previous chapter have laid the theoretical foundations of this Yb magnetometer based on the understanding of Autler-Townes splitting and the spatial Hanle effect. We have discussed the origin of dark resonances and their relationships to the magnetic field magnitudes and presented the effects of laser polarization directions and different vector components, and how both of them may be used to estimate the B_x and B_y components of the magnetic fields. The next chapter will combine all of these aspects together and demonstrate how this magnetometer works in practice.

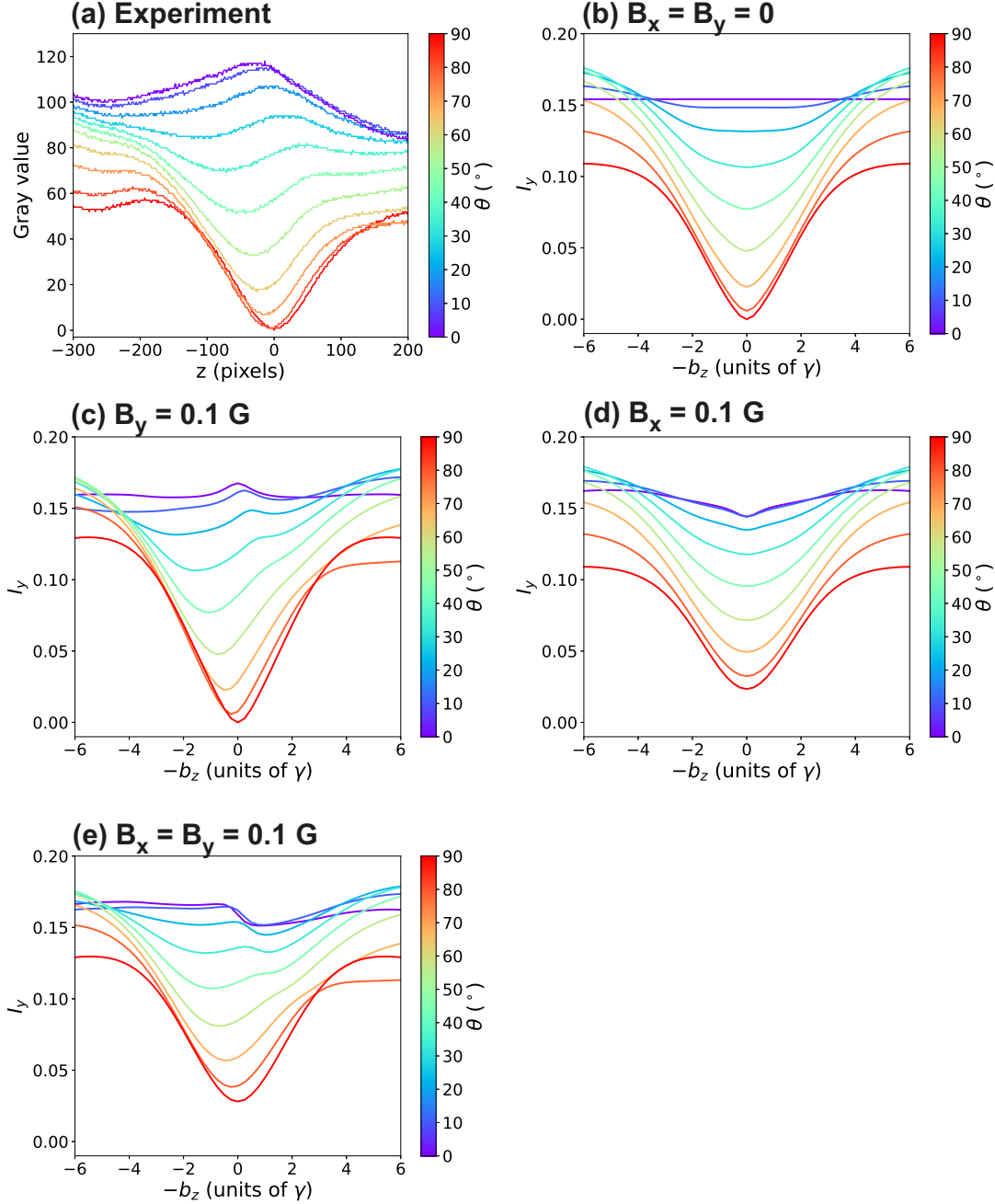


Figure 7.8: Intensity cross-sections of a “dark spot” where the magnetic field is nearly zero at different polarization angles $0^\circ \leq \theta \leq 90^\circ$. The experimental data in (a) show spatial shifts and change in contrast as θ changes. Numerical calculations in (b)-(e) represent how fluorescence characteristics change with different magnetic field settings. (c) $B_x = 0, B_y = 0.1$ G shows the best agreement with the experimental data.

Chapter 8

Magnetic field sensing in practice

8.1 Introduction

This chapter demonstrates how the theoretical model and results from Chapters 6-7 can be applied in practical magnetic field sensing. I will first go over how the model that includes only two frequency sidebands can be extended for all the frequencies present in square-wave amplitude-modulated light and the implications on dark resonance conditions. Next, I will demonstrate how to map magnetic field magnitudes from an experimental dataset taken at different modulation frequencies. From the same dataset, I will also show how we can deduce the magnetic field vector components B_x, B_y, B_z based on what we learned from Chapter 7. I will then investigate the laser power dependence on the dark resonances. And finally, the chapter concludes with estimates of the magnetometer's figures of merit.

8.2 Square-wave sidebands

As shown previously in Sec. 6.3.3, adding more driving optical fields leads to more dark lines. For example, as shown in Fig. 6.7b adding light fields at detunings $\pm 3\delta_{mod}$ to the model produces additional dark resonances at $|b_z| = \frac{g\mu_B}{\hbar}|B| = 2\delta_{mod}$ and $3\delta_{mod}$. This is because, with Doppler broadening, any pair of sidebands can produce a dark resonance due to Autler-Townes splitting where the frequency difference of the pair

matches the splitting $2g\mu_B|B|$ between the $m_J = \pm 1$ excited states. As each dark line provides a direct measurement of the magnetic field at its location, the more lines we see on one camera frame the more locations we can map the B-fields. Hence, in the experiment, we would like to have as many discrete laser frequencies as possible to produce many visible dark resonances. Alternatively, it is possible to use fewer frequency sidebands and sweet the modulation frequency δ_{mod} to map out the B-field gradient.

In our experiment, we typically use square-wave amplitude modulation to produce many laser frequency sidebands. As illustrated in Fig. 8.1c, the duty cycle of 10% (the laser beam is turned “on” by an acousto-optic modulator (AOM) only 10% of the time) produces more sidebands than the 50% duty cycle. These plots of ideal square waves and their Fourier transforms were made using Scipy and I used $\delta_{mod} = 1$ MHz for illustration purposes. δ_{mod} is typically in the MHz range in the experiment.

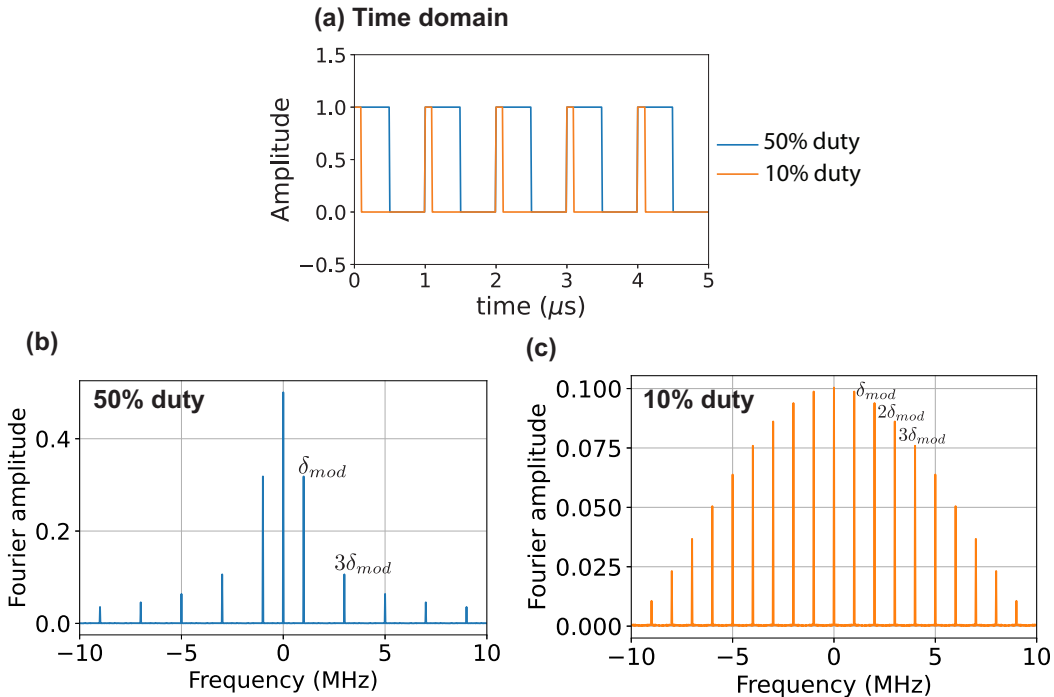


Figure 8.1: Time and frequency domains of square-wave amplitude modulated light at 50% and 10% duty cycles at modulation frequency $\delta_{mod} = 1$ MHz.

Figures 8.1b and 8.1c show the Fourier transform (FT) of the square waves at 50% and 10% duty cycles, respectively. Both Fourier transforms contain the carrier frequency (at zero frequency) because the amplitude is modulated between 0 (“off”) and 1 (“on”). Besides the carrier, the Fourier Transform of the 50% duty square wave contains odd harmonics of δ_{mod} at decreasing amplitudes whereas the 10% duty square wave FT contains both even and odd harmonics of δ_{mod} . The Fourier amplitudes also decrease less rapidly for the 10% duty square wave. The fluorescence images taken using a 10% duty square wave are shown in Fig. 8.3. With multiple dark resonances present, we can reconsider the dark-resonance conditions and compute the magnetic fields as follows.

8.2.1 Dark-resonance condition

With only two driving fields at detunings $\pm\delta_{mod}$ linearly polarized along y -direction (vertical) with polarization angle $\theta = 90^\circ$, a dark resonance due to Autler-Townes splitting occurs when the frequency difference between the two fields $\Delta\omega = 2\delta_{mod}$ matches the energy splitting $2\frac{g\mu_B}{\hbar}|B|$ between the $m_J = \pm 1$ excited states. In addition to dark lines where $\frac{g\mu_B}{\hbar}|B| = \delta_{mod}$ The spatial Hanle effect predicts zero fluorescence along the y -direction where the magnetic field is zero.

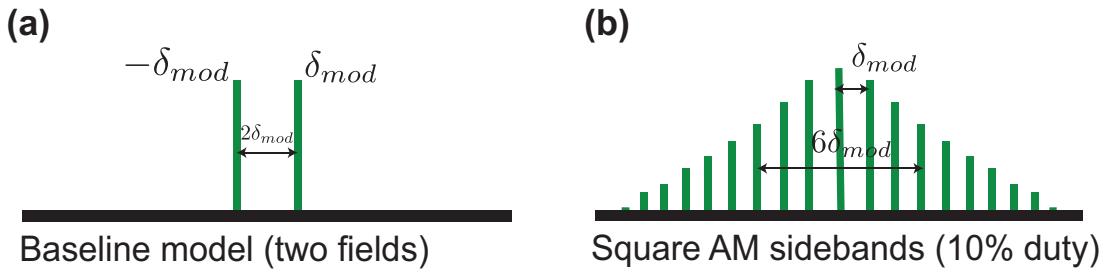


Figure 8.2: Frequency differences $\Delta\omega$ between the optical fields present in (a) the baseline model ($\Delta\omega = 2\delta_{mod}$) and (b) a 10% duty square wave ($\Delta\omega = n\delta_{mod}$). Any pair of sidebands in (b) has a frequency difference that is a multiple of δ_{mod} .

For square-wave AM light with a carrier and many evenly spaced sidebands (δ_{mod} apart), any pair of driving fields can produce a dark resonance. The frequency difference between a pair of driving fields $\Delta\omega$ can be any integer multiple of δ_{mod} , as

shown in Fig. 8.2b. Hence, we would expect many dark resonances where

$$2\frac{g\mu_B}{\hbar}|B| = \Delta\omega = n\delta_{mod} \quad (8.1)$$

or in our notation

$$b = \frac{g\mu_B}{\hbar}|B| = \frac{n}{2}\delta_{mod} \quad (8.2)$$

where n can be any integer 1, 2, 3, ...

In a magnetic field gradient along the x - or z -direction, this setting produces a series of dark stripes perpendicular to the gradient and allows us to determine the B-field value at the location of each stripe. Some ambiguity in the value of n may exist unless we can specify where the field is zero (fluorescence is or near zero). Sweeping the modulation frequency δ_{mod} can identify dark stripes more precisely, as demonstrated in the next section.

8.3 Mapping B-fields from data

My labmate Hongquan Li took the data shown in Figure 8.3. He used a pair of anti-Helmholtz coils to produce a magnetic field gradient primarily along the z -direction and collected fluorescence images while scanning the laser modulation frequency δ_{mod} . At this stage, we did not have additional Helmholtz coils to cancel background magnetic fields in x or y directions. The effects of B_x and B_y components of the background B-fields from the Earth's field and the permanent magnet in our Zeeman slower will be discussed later in Sec. 8.4.

Figure 8.3 shows the fluorescence images taken at modulation frequencies of 1, 2, and 4 MHz as well as respective cross-sections (line scans) along the z -direction. The dark-resonance condition (8.2) predicts a series of dark resonances where $b = \frac{g\mu_B}{\hbar}|B| = \frac{n}{2}\delta_{mod}$, which changes with the choice of the modulation frequency δ_{mod} . At $\delta_{mod} = 2\pi \times 1$ MHz, more dark lines are visible because the smaller δ_{mod} means a narrower spacing between consecutive dark stripes, providing a finer spatial map of magnetic fields.

To determine values of magnetic fields at the locations of the dark stripes (as

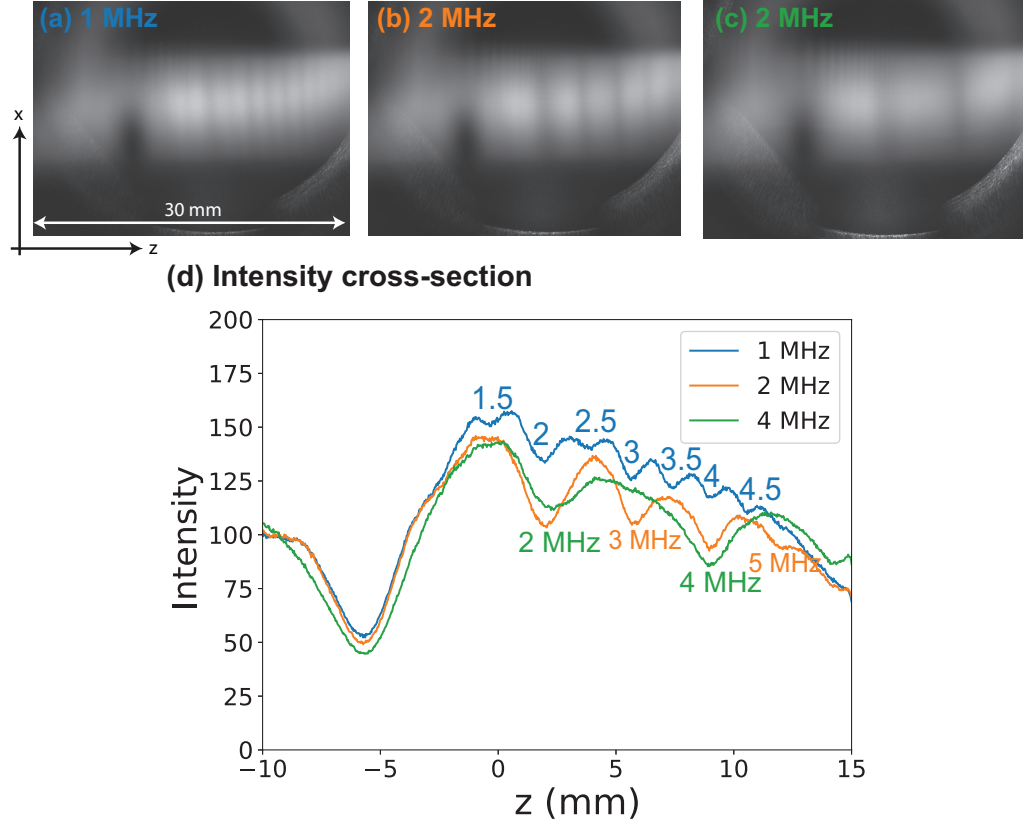


Figure 8.3: Images taken at the modulation frequencies of (a) 1 MHz, (b) 2 MHz, and (c) 4 MHz. The length of the images is 30 mm along the z -direction, with the scale z running from -15 to 15 mm. (d) Intensity cross-sections (line scans) from the three frames are shown. The labels on the dips represent the respective values of the Zeeman splitting (frequency) in MHz inferred from the dark-resonance condition (8.2). Note that the frequency splitting of ≈ 2.1 MHz is equivalent to the magnetic field strength of 1 G.

shown in Fig. 8.3d), we first note that the prominent dark spot near $z = -5$ mm present in all images indicates $b_z = \frac{q\mu_B}{\hbar}|B_z| = 0$. Next, we can assume $|B|$ gradually increases away from the zero- b_z spot. From the dark-resonance condition (8.2), we expect dark lines everywhere that $b = \frac{q\mu_B}{\hbar}|B|$ is equal to multiples of $\delta_{mod}/2$. Starting with the 4 MHz data (green line scan), the first and second dips next to the zero- b_z spot correspond to the Zeeman (frequency) splitting of $\frac{q\mu_B}{\hbar}|B| = 2$ MHz and 4 MHz, respectively. The other two line scans (1 and 2 MHz), also contain respective dips at 2 and 4 MHz since they are also multiples of a half of the modulation frequency.

Next, we can fill out other dips in between that are present in the other two line scans with the respective spacing. Note that the Zeeman splitting of 2.1 MHz is equivalent to a magnetic field of 1 G, so these data show a B-field gradient map with $|B|$ in the few G range. On the line scans, some dips including ones at 0.5 MHz and 1 MHz are missing from the 1 MHz and 2 MHz curves. We later learned that background B_y fields can account for the missing dips, as discussed in Sec. 7.3.1.

So far, we have demonstrated how the magnitudes of magnetic fields can be read off a fluorescence image assuming a smooth interpolation between the dark stripes. To reveal a finer structure, this process can be easily scaled up by increasing the number of frames (taken at different modulation frequencies) included in the analysis. In practice, the modulation frequency can be swept while taking a video of the atomic fluorescence, which makes the data collection fast and convenient. The next goal of our analysis is to turn discrete data points from the dark stripes into a continuous magnetic field gradient map.

We can generalize the dark-resonance condition for magnetic fields in 3D by substituting $|B| = \sqrt{B_x^2 + B_y^2 + B_z^2}$ in (8.2). With this, we obtain

$$b = \frac{g\mu_B}{\hbar} |B| = \frac{g\mu_B}{\hbar} \sqrt{B_x^2 + B_y^2 + B_z^2} = \frac{n}{2} \delta_{mod}. \quad (8.3)$$

The square of this relationship represents a series of spherical surfaces in the (B_x, B_y, B_z) space with radii of $\frac{n\hbar\delta_{mod}}{2g\mu_B}$. Note that choosing either $B_x = 0$ or $B_y = 0$ reduces the mapping into 2D as shown in the contour plots in Figs. 7.3 and 7.5 in Chapter 7.

With this updated expression (8.3), the b values labeled on Fig. 8.3d directly provide the magnitude of the B-fields, $b = \frac{g\mu_B}{\hbar} |B| = \frac{g\mu_B}{\hbar} \sqrt{B_x^2 + B_y^2 + B_z^2}$, and the dark oval-shaped spot corresponds to $B_z = 0$. The dark circles in Fig. 8.4 show the Zeeman splitting b deduced from the dark stripes as well as the corresponding magnetic field values in G. Using the data from only three frames in Fig. 8.3, we estimate the uncertainty in $|B|$ to be on the order of 0.01 G (10 mG). For a scalar magnetometer, our job here is done! However, we can also use the numerical model to estimate individual components B_x, B_y and B_z .

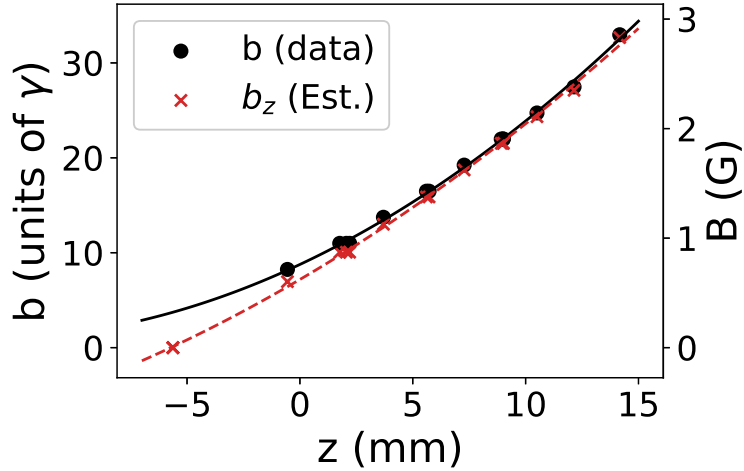


Figure 8.4: B-field gradient map calculated from the positions of the dark stripes from the experimental data shown in Fig. 8.3. The magnitudes of the field $b = \frac{g\mu_B}{\hbar}|B|$ measured from the data are plotted in black. With estimates $B_x = 0.12$ G, $B_y = 0.36$ G, we calculated the B_z component and plotted in red. Both black and red lines represent respective quadratic fits of b and b_z . The left vertical scale represents the frequency splitting in the units of γ , and the right vertical scale converts b (in γ) into magnetic field strength in G.

8.4 Estimating B_x and B_y from data

As discussed in the previous chapter, magnetic field components B_x and B_y from the Earth's field and the Zeeman slower permanent magnet can alter the observed fluorescence pattern in several ways. First, non-zero B_x can lead to some light being emitted along y where we expect $B_z = 0$. Recall the dark spot from Fig. 8.3. The intensity cross-sections show that the intensity was not completely zero near $z = -5$ mm. Although the background scattered light may account for some of this discrepancy, since we did not cancel the background Earth's field, it is likely that the background B_x is at play. With the spatial Hanle effect, non-zero B_x can tilt the dipole radiation pattern away from it being oriented along the y -direction, resulting in some light traveling vertically and reaching the camera.

Another observation from the data is several missing dips where $b = \frac{g\mu_B}{\hbar}|B| = 0.5$

and 1 MHz. This is likely a result of non-zero B_y in the background. Inspecting the (B_y, B_z) contour map in Fig. 7.3 and plotting cross-sections at constant B_y 's show that in the 2D picture (with circular contours $\frac{g\mu_B}{\hbar}\sqrt{B_y^2 + B_z^2} = \frac{n}{2}\delta_{mod}$), non-zero B_y can shift the apparent dark lines closer to the $B_z = 0$ location and wash out the appearance of the first few dips.

We can use our numerical model to explore the (B_x, B_y) parameter space to see which values produce the closest result to the data. We will focus on the intensity cross-section taken with $\delta_{mod} = 2$ MHz (orange curve in Fig. 8.3) because it is missing a dip at $b = 1$ MHz and has non-zero minimum intensity, displaying two prominent characteristics of non-zero B_x and B_y .

8.4.1 Model implementation - 10% duty square wave

In this section, we would like the model to replicate the experiment as closely as possible and show all the visible dark stripes, so we included a total of seven driving fields to model a 10% duty square wave.

Building off of the baseline model, which originally includes only two driving fields, several more sidebands of a 10% duty square wave are added to the model: the carrier (assumed to be on resonance ω_0), the second harmonic sidebands at $\omega_0 \pm 2\delta_{mod}$, and the third harmonic sidebands at $\omega_0 \pm 3\delta_{mod}$. There are now a total of seven fields, corresponding to the carrier and the first three harmonics of the modulation frequency δ_{mod} . The relative strengths of these different fields are obtained from the Fourier amplitudes shown in Fig. 8.1c. The strengths of the first three harmonic sidebands are given in the table below in terms of the Rabi frequency ratios $\Omega_{i=1,2,3}/\Omega_0$, where Ω_0 is the Rabi frequency of the carrier.

The Rabi frequencies of the 3rd harmonic sidebands at $\omega_0 \pm 3\delta_{mod}$ are only 17% smaller than that of the carrier Ω_0 . The choice to include up to the 3rd harmonic sidebands was arbitrary. The main consideration was the number of fluorescence dips we would like our model to reproduce such that we could make a quantitative comparison with our experimental data. Including up to the third harmonic driving fields produces dark resonances where $\frac{g\mu_B}{\hbar}|B| = \frac{1}{2}\delta_{mod}, \delta_{mod}, \dots, 3\delta_{mod}$. This is sufficient to

Frequency	Fourier amplitude	Relative Ω_i/Ω_0
ω_0 (carrier)	0.109	1
$\omega_0 \pm \delta_{mod}$	0.107	0.98
$\omega_0 \pm 2\delta_{mod}$	0.101	0.93
$\omega_0 \pm 3\delta_{mod}$	0.091	0.83

Table 8.1: Fourier amplitudes and Rabi frequency ratios of the modulation sidebands included in the model.

reproduce the first six dark lines (excluding the zero-field dark spot).

Using the magnitude of B-fields $|B|$ (and b) from the data, we fitted a quadratic curve to interpolate and extrapolate the values across the z range. Assuming for now that there are constant B_x and B_y present, we can calculate $|B_z| = \sqrt{|B|^2 - B_x^2 - B_y^2}$ at each location z and plug the B-field values into the model to compute the fluorescence emitting along y , as observed by the camera. We can estimate B_x and B_y from the data and the numerical model as follows.

8.4.2 Results (2 MHz modulation frequency)

The black curves in Fig. 8.5 are the same intensity cross-section from the 2 MHz data shown in Fig. 8.3d. The orange curves with semi-transparent uncertainty bands, estimated from $\sqrt{\frac{I_y(1-I_y)}{N}}$ for N atoms in the simulation, are the fluorescence curves calculated from the model at different magnetic fields B_x, B_y settings and multiplied with a constant so they lay on top of the data.

Plot (a) shows a case where we assume $B_x = B_y = 0$. Without the transverse B-fields, we would expect the minimum intensity to go to zero where $B_z = 0$ and an additional dip where $b = 2\pi \times 1$ MHz. Introducing $B_y = 0.36$ G (keeping $B_x = 0$) in (b) shows how this “missing dip” gets washed out. We estimate this B_y value by inspecting horizontal cross-sections of the (b_y, b_z) contour plot in the previous chapter (Fig. 7.3). Next, to account for non-zero minimum intensity, we introduced non-zero B_x . The combination of $B_x = 0.12 \pm 0.02$ G and $B_y = 0.36 \pm 0.02$ G gives the best agreement with the data, as shown in (d). With these B_x, B_y values, we estimated B_z and plotted in red in Fig. 8.4. We note that these values of B_x and

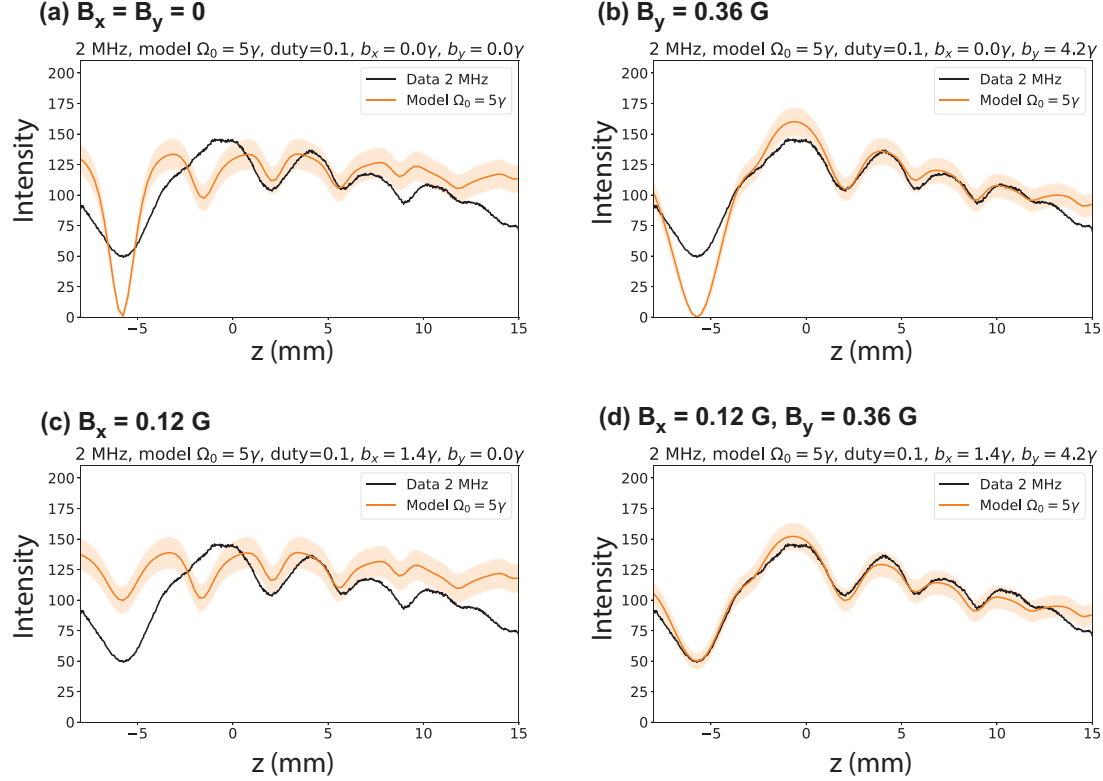


Figure 8.5: Intensity cross-section from 2 MHz data (black curve) vs fluorescence calculated by the model (orange curve) assuming (a) $B_x = B_y = 0$, (b) $B_x = 0$, $B_y = 0.36$ G, (c) $B_x = 0.12$ G, $B_y = 0$, and (d) $B_x = 0.12$ G, $B_y = 0.36$ G. (d) seems to agree best with the data.

B_y are reasonable and consistent with the Earth's field in our laboratory with nearby magnetically permeable materials including an optical table, a Zeeman slower shield, and ion pumps.

Including B_x and B_y in the model immensely improves the fit between the theoretically calculated fluorescence and the experimental data with reasonable assumptions: B_z gradient along the z -direction and constant B_x, B_y over this $\Delta z \approx 20$ mm range. A striking and somewhat surprising aspect of this result is that at least for this type of magnetic field configuration (B_z gradient along z and constant B_x and B_y), it is possible to determine the magnitudes of all three vector components: $|B_z(z)|, |B_x|, |B_y|$ using a single laser field and a single polarization direction along the y -axis (vertical).

8.5 Laser power dependence

The dark lines are subject to power broadening as well as Doppler broadening. To investigate the laser power dependence, Hongquan took more fluorescence images using the modulation frequency of $\delta_{mod} = 2$ MHz and the same magnetic field settings as the previous dataset shown in Fig. 8.3 while varying the average laser power from 1 to 17 mW in 1 mW increments. With 10% duty cycle, this means the peak laser power was ranging from 10 mW to 170 mW. The intensity cross-sections taken across four dark stripes are plotted in Fig. 8.6a. As power increases, the fluorescence intensity and the contrast of the dark lines (dips) increase.

With the model and the B-field map computed earlier (incorporating also the B_x and B_y estimates), we numerically calculated the fluorescence at different laser power and plotted the results in Fig. 8.6b. In the model, total laser power is distributed among the 7 sidebands (carrier + 3 pairs of harmonics) according to the squares of the Fourier amplitudes shown earlier in Sec. 8.4.1.

Currently, the fluorescence calculated from our model saturates at lower laser power compared to the experimentally measured fluorescence. As Fig. 8.6b shows, with laser power of 0.5-8.5 mW as the model input, the calculated fluorescence curves look a lot like the experimental data taken at twice the laser power. To inspect this discrepancy more carefully, we also plot power saturation curves in Fig. 8.7 using the intensity of the second peak from the left.

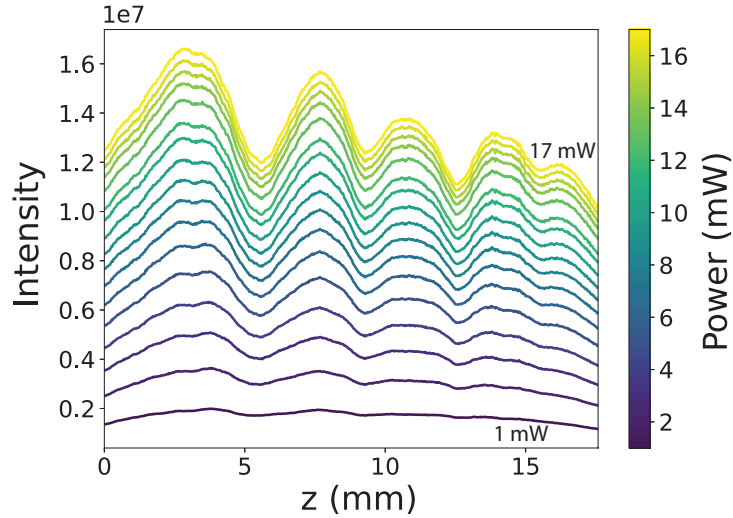
From each intensity-power plot in Fig. 8.7, we fit a power saturation curve to estimate the saturation power P_{sat} from the experimental data and the model. The curve follows this expression

$$I = I_0 \frac{P/P_{sat}}{1 + P/P_{sat}} \quad (8.4)$$

where I is the fluorescence intensity, P is the laser power, I_0 is the maximum intensity reached once it saturates. From least square fitting, $P_{sat} = 16.1 \pm 0.4$ mW for the experimental data, almost 4 times the saturation power estimated from the model ($P_{sat} = 4.07 \pm 0.06$ mW). These saturation curves can be useful for more careful quantitative comparisons between the experimental data and the model. One can, for example, after adjusting for the difference in laser power, carefully fit the theoretical

curves on the data, assess how well the model fits the data, and identify any systematic sources of discrepancy between the two. The reasons for this discrepancy are currently unknown.

(a) Experiment



(b) Model (intensity along y)

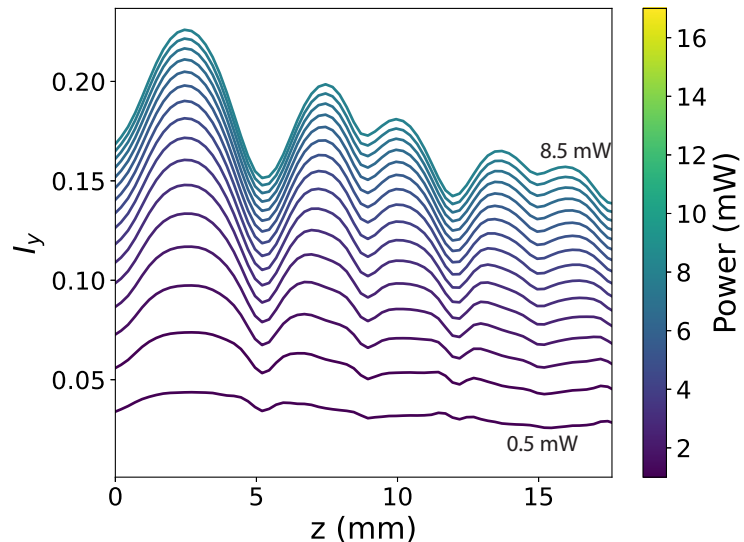


Figure 8.6: Power dependence - fluorescence curves at different laser power from (a) experimental data ($\delta_{mod} = 2$ MHz) and (b) numerical model.

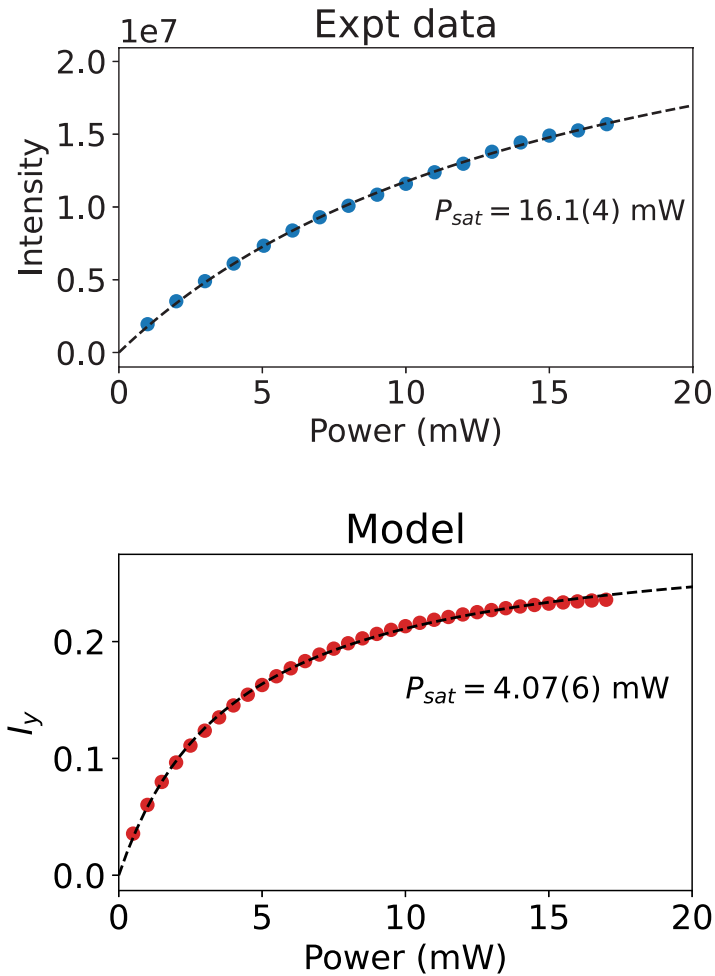


Figure 8.7: Peak intensity (extracted from the second peak from the left on Fig. 8.6) as a function of laser power from (a) experimental data and (b) model with fitted power saturation curves.

8.6 Performance estimates

Here is a brief summary table of the preliminary estimated performance of this Yb optical atomic magnetometer. I explain briefly below how we estimate some of these numbers.

B-field uncertainty	$\approx 1 \text{ mG (} 100 \text{ nT)}$
Sensitivity	$\approx 10 \mu\text{G (} 1 \text{ nT})$, with the present camera: 3 ms frame rate provides 15,000 spatially-resolved B-field measurements
Dynamic range	0 to $> 10 \text{ T}$
Response time	camera-limited but can be down to $10 \mu\text{s}$ (atom's lifetime $\approx 1 \mu\text{s}$)
Spatial resolution	$\Delta z \approx 100 \mu\text{m}$, $\Delta x = 15 \mu\text{m}$, $\Delta y = 3 \text{ mm}$ (set by spot size)

Table 8.2: Current performance estimates for our Yb magnetometer.

8.6.1 B-field uncertainty

From the calculated fluorescence, the typical FWHM of a dark-resonance dip is $\approx 5\gamma$ (for Rabi frequency of $\Omega \approx 10\gamma$), which is equivalent to the magnetic field strength of 0.43 G. Assuming that we can determine where the minimum of a dip is with 1/1000 precision, we obtain the B-field uncertainty of $0.43/1000 \text{ G} = 0.43 \text{ mG} \approx 1 \text{ mG}$ range.

Alternatively, we tried estimating this from the experimental data (3 frames) as we computed the magnetic field map (see Sec. 8.3). Given the uncertainty in extracting the dip positions $\Delta z = 0.05 \text{ mm}$, estimated from using two peak detection methods in Scipy, and the gradient $\Delta B/\Delta z \approx 0.14 \text{ G/mm}$, the B-field uncertainty is $\Delta B \approx 7 \text{ mG}$. Using more frames and better lineshape fitting is likely to reduce this uncertainty much further.

8.6.2 Sensitivity

We begin by estimating the photon flux S_{ph} from atoms undergoing spontaneous decays. The atomic flux is given by the atom density ρ_{Yb} (number of atoms per cm^3) times measurement volume V times the excited-state fraction ρ_e and multiplied with the % isotopic abundance of ^{174}Yb (the most abundant isotope, which accounts for 31.8%). We need to multiply this atomic density with the fluorescence rate $\gamma = 2\pi \times 182 \text{ kHz}$, the ratio of the homogeneous width $\Delta\nu_{homo}$ over the transverse Doppler

width $\Delta\nu_{Doppler}$, and the photon detection efficiency K .

$$S_{ph} = \rho_{Yb} V \rho_e (\%^{174}\text{Yb}) \times 2\pi\gamma \frac{\Delta\nu_{homo}}{\Delta\nu_{Doppler}} K. \quad (8.5)$$

This expression gives us a photon flux in the units of photons/s. Hence, the total number of photons we detect N_{ph} is S_{ph} multiplied by the measurement time T , and the photon shot noise is

$$\Delta N_{ph} = \sqrt{N_{ph}} = \sqrt{S_{ph}T} \quad (8.6)$$

The homogeneous linewidth $\Delta\nu_{homo}$ from Autler-Townes splitting depends on Rabi frequency Ω as does ρ_e . This linewidth $\Delta\nu_{homo}$ may be different from the FWHM of the dark lines that we observe from the collective fluorescence $\Delta\nu_{obs}$, but for the purpose of estimating the magnetic field sensitivity, we can use $\Delta\nu_{obs}$ as a proxy, where

$$\Delta\nu_{homo} \approx \frac{\Delta\nu_{obs}}{2}. \quad (8.7)$$

We can convert this frequency width $\Delta\nu_{obs}$ to the corresponding magnetic field range as

$$\Delta B_{AT} = \frac{h\Delta\nu_{obs}}{\Delta m_J g \mu_B} = \frac{2h\Delta\nu_{homo}}{\Delta m_J g \mu_B}, \quad (8.8)$$

where $\Delta m_J = 2$ for when we use the $m_J = \pm 1$ states and $\Delta m_J = 1$ for when one of the two states is $m_J = 0$. Note that the width of the dark lines $\Delta\nu_{obs}$ depends on the laser power. At $I/I_{sat} = 20$, $\Delta\nu_{obs} \approx 5\gamma$ from our model estimate.

Now we consider how the signal changes with the magnetic field, taking into account the dark-line contrast $C = \text{depth}/(\text{total fluorescence})$ of the dark line. From our model and experiment, best-case $C \rightarrow 0.3$ when laser intensity $I \gg I_{sat}$ at non-zero magnetic fields.

$$\frac{dS_{ph}}{dB} \approx \frac{dS_{ph}}{d\Delta\nu_{homo}} \times \frac{\Delta\nu_{homo}}{\Delta B_{AT}} \times C \quad (8.9)$$

$$= \frac{S_{ph}}{\Delta\nu_{homo}} \times \frac{\Delta m_J g \mu_B}{2h} \times C \quad (8.10)$$

$$= \frac{S_{ph} \Delta m_J g \mu_B C}{h \Delta\nu_{obs}} \quad (8.11)$$

Hence, the estimated magnetic field sensitivity is

$$\Delta B \approx \frac{(\Delta S_{ph})h\Delta\nu_{obs}}{S_{ph}\Delta m_Jg\mu_B C} = \frac{(\Delta N_{ph})h\Delta\nu_{obs}}{N_{ph}\Delta m_Jg\mu_B C} \quad (8.12)$$

$$= \frac{\sqrt{S_{ph}T}h\Delta\nu_{obs}}{S_{ph}T\Delta m_Jg\mu_B C} \quad (8.13)$$

$$= \frac{h\Delta\nu_{obs}}{\Delta m_Jg\mu_B C \sqrt{S_{ph}T}} \quad (8.14)$$

$$= \frac{\Delta\nu_{obs}}{(2.1 \text{ MHz/G})\Delta m_J C \sqrt{S_{ph}T}} \quad (8.15)$$

, for the measurement time of T and for optical shot-noise limited detection.

8.6.3 Dynamic range

The 3P_1 state is ≈ 20 THz away from the 3P_0 state, which does not have any magnetic sub-structure ($J = 0$). From the Zeeman splitting of the 3P_1 state of 2.1 MHz/G, 20 THz is equivalent to $B \approx kT$, so we would enter the strong-field regime of the Zeeman effect before running into the neighboring fine-structure state. The 3P_2 state, which is the second closest fine-structure level, is ≈ 50 THz away, so even with the $J = 2, m_J = -2$ sublevel, it would also require very large fields $\sim kT$ for it to be a problem.

I could not find the calculated or measured value of the threshold external magnetic field for the strong-field Zeeman effect to kick in for Yb in the 3P_1 state. A conservative B-field limit of 1500 G (0.15 T) is given in Loftus's thesis [64], but the author did not provide a reference nor explain in detail how it was calculated.

It would be interesting to try measuring large fields with our system and investigate this upper limit experimentally, but we would need a modulator that enables amplitude modulation at higher δ_{mod} . Reaching the modulation frequency in the GHz range would be straightforward. 10s of GHz range is feasible with electro-optic modulators, and arbitrarily higher frequencies are possible with two lasers.

8.6.4 B_x, B_y uncertainty from forward simulation

In the case where we have a B_z gradient in z and assume constant B_x, B_y , we currently estimate B_x and B_y and their uncertainties from forward simulation. We do that by varying the magnetic fields in the model and inspecting visually when the theoretical curves no longer show good agreement with the intensity cross-sections from the data. With the data shown in Fig. 8.5, we estimate the error bars of B_x and B_y to be $\approx 0.02 - 0.03$ G (20-30 mG). This can be more carefully done by finely tuning B_x and B_y and carefully evaluating the mean squared difference between the theoretical curve and the experimental fluorescence curve. Plotting the mean squared error as a function of both B_x and B_y would allow us to estimate not only the variance but the covariance of the two magnetic field components.

Chapter 9

Conclusion

This thesis presented two novel applications of the narrow 556 nm $^1\text{S}_0$ - $^3\text{P}_1$ transition in Yb, in stimulated slowing and magnetometry. Much of this work is the development of theoretical and computational models in Python to simulate and analyze interactions between Yb atoms and strong optical fields at 556 nm.

The first half of this thesis investigated the stimulated slowing approaches with bichromatic and polychromatic forces where stimulated emission enables fast coherent momentum exchange between atoms and photons, and hence produces large slowing forces on atoms despite the small spontaneous decay rate from the narrow transition ($\gamma = 2\pi \times 182$ kHz).

Based on previous work on bichromatic slowing, which has been demonstrated in alkali atoms and molecules, our model extended this approach to investigate different types of amplitude and phase modulation to improve the force in both the velocity and time domains. We found that introducing odd-harmonic frequency sidebands via a square-wave modulation broadened the velocity range of the force and reduced the time the atoms spent in the excited state, making the slowing more efficient. The model has also allowed us to optimize design parameters for the slowing experiment. Monte Carlo simulations revealed that both of the stimulated slowing methods, which require only the 556 nm laser, can replace a traditional 399 nm Zeeman slower to produce a comparable MOT loading rate on the order of 10^8 atoms/s. The stimulated slowing approaches show promise in eliminating the 399 nm laser and repumping

lasers from cold Yb experiments and making the experimental design more compact for complicated systems such as ultrastable Yb lattice clocks or Yb tweezer arrays for quantum computing applications.

While the first half of this thesis offered an alternative solution to improve and support existing cutting-edge cold Yb experiments, the second half of this thesis presented an exciting, brand-new discovery in quantum sensing. Based on fluorescence imaging of thermal Yb atoms on the 1S_0 - 3P_1 transition, we have developed an atomic magnetometer with unique spatial imaging and vector capabilities. In our system, the combination of Zeeman-shifted V systems in the 1S_0 - 3P_1 transition, strong-field Autler-Townes splitting, and the spatial Hanle effect produces a dark-striped pattern in the atomic fluorescence that is visible by the eye and on the camera. These dark resonances provide a fast, powerful method for magnetic field imaging and mapping of the field's contours and gradients.

The theoretical model that I developed helped us understand the origin of the dark lines and investigate the underlying strong-field effect in this multilevel atom driven by multiple optical fields from the frequency sidebands of amplitude-modulated light at 556 nm. Both Autler-Townes and Hanle effects are sensitive to the vector direction of the magnetic fields, enabling vector measurements. With the model that calculates the fluorescence as a function of arbitrary magnetic fields, we were able to estimate all three vector components of the magnetic fields from experimental data taken with different laser polarization directions.

The present camera enables our magnetometer to take 15,000 spatially resolved measurements at the video frame rate ≈ 3 ms at the field sensitivity of $\approx 10\mu\text{G}$ (1nT). Further investigation and improvement of the response time and sensitivity are underway for this already powerful imaging and vector magnetometer that has much potential to advance magnetic field imaging and quantum sensing.

Appendix A

Code: Stimulated Slowing

Python codes and documentation for the stimulated slowing project are posted to
<https://github.com/tinatn29/Yb-slowing>.

A.1 Instructions

- Clone the git repository to your local directory.
- Upload everything to your Sherlock directory `$SCRATCH/some_folder/$`, preserving the folder structure for convenience. To make sure everything runs smoothly on Sherlock, use the checklist below.
 - Class files `SSMCSolver_BCF.py` and `SSMCSolver_square.py`
 - Random number generator functions `RandomInitialize.py` (the class files need this)
 - Main script for the simulation you want to run `RunMC_.py`
 - If `RunMC_.py` requires loading numpy arrays for atoms' velocities, positions, and starting times, make sure those files are in the correct directory. By default, they should be in the folder `input_files/`. See A.3.5 on how to generate new input files.

- Sherlock job submission script that specifies computing resources (number of computing nodes, number of CPU cores, memory, runtime) requested. Modify one of the existing Python `submit_.py` files or create a new Bash `submit_.sh` files. See A.3.3 for more details.
- On Terminal, `ssh` into Sherlock and navigate to the directory where the files live. Load the Python module with the command `ml python/3.6.1` (this will depend on which version of Python you installed on Sherlock).
- Submit job(s). `cd` into the correct directory on Sherlock. For a Python submission script use `python3 submit_.py` followed by any required arguments (depending on how you set up the script). For a Bash script use `sbatch submit_.sh`. See [Sherlock documentation](#) for more details.
- To see jobs in the queue use `squeue -u <SUnetID>`
- To cancel a job use `scancel <jobID>`. To cancel all jobs in the queue use `scancel -u <SUnetID>`

A.2 Python libraries used

Make sure you have the following libraries up and running on both your local computer and Sherlock.

- Numpy
- Scipy
- [QuTiP: Quantum Toolbox in Python \[115, 116\]](#)
- Multiprocessing

To process, analyze, and visualize the data, I also use Matplotlib, Pandas, and Jupyter Notebook.

A.3 Descriptions and pseudocodes

For readability and to save space, pseudocodes of the important code files are given in this appendix instead of the full scripts.

A.3.1 Main class file (BCF) SSMCSolver_BCF.py

This file defines the class `MCSolver`, the functions and parameters within, and helper functions (at the top of the file before the class definition) used for numerical calculations of the bichromatic force and Monte Carlo simulations of the Yb atoms. The first part of the code sets up the parameters and helper functions.

```
import relevant libraries
import GreenLaser, Atom classes from SSParameters.py
import custom functions from RandomInitialize.py

def chirped_detuning(time, chirp_parameters):
    Calculate the laser frequency detuning during chirp

def H_12_four, H21_four(time, args):
    Calculate the off-diagonal elements of the Hamiltonian: H_12 &
    H_21

def H12_derivative_z_4(time, args):
    Calculate the z-derivative of H12

class MCSolver():
    def __init__():
        Initialize attributes & parameters used in calculations

    def SetChirping():
        Set chirp parameters: period, max velocity detuning, min
        velocity detuning

    def Omega_Gaussian():
        Calculate Rabi frequency in a Gaussian beam
```

```
def UpdateArgs():
    # Update arguments before the next simulation iteration
    Update detuning if laser frequency chirp is used
    Update the atom's velocity & position
    Update time elapsed
    Update the Rabi frequency since the atom has moved
```

The second part of the code defines functions that carry out numerical calculations of the bichromatic force and then integrate the force to update both the atom's velocity and position over a $10\text{-}\mu\text{s}$ duration.

```
def SolveStimulatedForce():
    # Solve for force F(t) in a 10-microsecond window
    self.UpdateArgs()

    # Solve Linblad Master equation with QuTiP mesolve
    Set no. of solver iterations
    Solve the equation for density matrix rho(t)

    Calculate force from the z-derivative of H_12
    Calculate average excitation probability

def IntegrateForce_1D():
    # Update atom's velocity v_3D = [vx, vy, vz]
    # Update vz since it is affected by the bichromatic force F(t)
    Integrate F(t) to compute the change in velocity in z-direction
    Here the parameter v_array = vz(t)
    dt = 10 us (total time elapsed)

    # Update atom's position r_3D = [x, y, z]
    x -> x + (vx * dt)
    y -> y + (vy * dt) - (0.5 * g * dt**2) # gravity

    # Update vy
    vy -> vy - g * dt
```

```

# Update z, v_z and move the clock forward
z -> z + integrate(vz * dt)
vz -> vz from v_array
t_elapsed -> t_elapsed + dt

def MoveAtom_NoForce(dt):
    """
    If atom's outside the laser beam: atom moves without being
    slowed
    Update atom's position and time but not velocity
    """
    x -> x + (vx * dt)
    y -> y + (vy * dt) - (0.5 * g * dt**2) # gravity
    z -> z + (vz * dt)
    t_elapsed -> t_elapsed + dt

```

The next part of the code (lines 242-267) defines helper functions that check the status of the atom whether it has passed the MOT region, been trapped by the MOT, moved outside laser beam (in case of a flat-top beam), or become too far detuned to feel any force.

Simulating a single atom

Putting all the pieces together, the function below calculates an atom's trajectory from start to finish. The function outputs an array [starting velocity, starting position, starting time, final velocity, final position, final time, atom's status, runtime in secs].

```

def SolveMC_single_GaussianBeam_InputAll(v_initial, r_initial,
t_initial):
    Gaussian_beam = True # to make sure Rabi freq depends on
position
    Set initial velocity, position, & time
    Set chirp parameters v_max, loading time

    Start the runtime clock

    if the atom is too far-detuned (v_z > v_max + Delta/k):
        # Atom will pass the MOT region without being trapped.

```

```

        End the simulation ("PASSED")

    if the atom can be trapped (slow, close enough to the MOT):
        # Atom will be TRAPPED
        End the simulation ("TRAPPED")

    # Continue to run the simulation as long as the atom hasn't
    passed the MOT region (z < 34 cm)
    while z < 0.34:
        if the atom can be trapped (slow, close enough to the
        MOT):
            End the simulation ("TRAPPED")

        if the atom starts moving backwards:
            End the simulation ("FAILED")

        if self.Check_If_InsideBeam() and self.
        Check_If_InsideVRange():
            # For atoms in z >= 0 (laser present) and |v_z -
            v_detuning| <= 1.5 Delta/k
            # Calculate force and integrate
            self.SolveStimulatedForce()
            self.IntegrateForce_1D()
            self.UpdateArgs()
        else:
            # OR atom continues to move without being slowed
            self.MoveAtom_NoForce()
            self.UpdateArgs()

    return outputs once the simulation is complete

```

The function above assumes the Gaussian beam profile. For a flat-top beam, use the function `SolveMC_single_FlatTop_InputAll()` instead. Another similar function `SolveMC_single_FixedDetuning_InputAll()` should be used if the laser detuning is fixed (without chirp).

Simulating lots of atoms with parallel computing

The function `SolveMC_parallel_InputAll()` implements the above function with parallel computing. The function arguments correspond to initial velocities, positions, and starting times of N atoms. The parameter `n_cores` is set to the number of CPU cores detected by the command `mp.cpu_count()` or `max_cores`, whichever smaller. This is necessary because when we would want to utilize all the cores available on our local computer, but we are allowed to use only a fixed (up to 32) number of cores on Sherlock, depending on what we request when submitting the job. We usually request only one computing node at a time on Sherlock so the maximum number of cores is 32. Similar to previously, there are also corresponding parallel functions for flat-top beams and fixed detunings.

```

def SolveMC_parallel_InputAll(self, v_input, z_input, t_input,
max_cores=32):
    """
    Solve MC for N atoms using multiprocessing
    """

    import multiprocessing as mp

    start_time = time.time()
    n_cores = np.amin([mp.cpu_count(), max_cores])
    pool = mp.Pool(processes=n_cores)

    args = list(zip(v_input, z_input, t_input))
    # merge the inputs into args = [[[v1], [z1], [t1]], [[v2], [z2], [t2]], ...]

    # then use pool.starmap instead of map
    outputs = pool.starmap(self.
SolveMC_single_GaussianBeam_InputAll, args)
    print('Time elapsed: {:.2f} sec'.format(time.time() -
start_time))

    return outputs

```

A.3.2 Square wave version: `SSMCSolver_square.py`

The square-wave version of `MCSolver` is defined in a separate file `SSMCSolver_square.py`. The major difference is how the Hamiltonian is constructed. Instead of overlapping bichromatic (CW) beams at frequencies $\omega \pm \delta$, the square-wave version of `MCSolver` allows sinusoidal and square-wave modulations of both amplitude and phase.

Amplitude modulation

The parameter `self.args['Rabi_shape']` defines the amplitude modulation function as follows: For most simulations I have run, I set `self.args['Rabi_shape'] =`

Rabi_shape	AM function
-1	No modulation (constant amplitude)
0	Near-ideal square-wave AM (<code>scipy.signal.square</code>)
1	Sinusoidal AM
$n \geq 2$ (integer)	Non-ideal square wave with a truncated Fourier series that consists of n odd harmonics. For example, $n = 2$ means the square-wave function consists of only the first and the third harmonics of the modulation frequency δ_{sq} .

Table A.1: Options for the parameter `self.args['Rabi_shape']` to set up near-ideal or truncated square-wave modulation shape.

2 or 3.

Phase modulation

The variables `self.args['phasemod_right']` and `self.args['phasemod_left']` are set to zero by default (no phase modulation). To modulate the phase of one beam or both, simply set their values to 1 (or -1 to introduce an opposite sign). Similar to AM, the modulation function is set by another parameter `self.args['PM_shape']` as follows:

PM_shape	AM function
0	Near-ideal square-wave AM (<code>scipy.signal.square</code>)
1	Sinusoidal AM
$n \geq 2$ (integer)	Non-ideal square wave with a truncated Fourier series that consists of n odd harmonics. For example, $n = 2$ means the square-wave function consists of only the first and the third harmonics of the modulation frequency δ_{sq} .

Table A.2: Options for the parameter `self.args['PM_shape']` to set up near-ideal or truncated square-wave modulation shape.

A.3.3 Simulation script and parameters (BCF)

Use the script `RunMC_local_BCF.py` for test runs on your local computer before submitting jobs on Sherlock. A different file `RunMC_allinput_BCF_chirp.py` is designed to run simulations on a batch of atoms with pre-set velocities, positions, and departure times from the oven. These initial parameters are set by the `.npy` files in the `input_files` folder on the repository. To generate new input files, check out the script `GenerateBatchAtoms.py`, described in Appendix A.3.5 below.

`RunMC_allinput_BCF_chirp.py` takes the following arguments: Note that $\Omega =$

sys.argv	Argument	Description	Example
1	δ	Bichromatic detuning (in γ)	100
2	filename	.csv output filename	<code>test.csv</code>
3	v_max	chirp upper limit in velocity detuning (in m/s)	150
4	v_min	chirp lower limit in velocity detuning (in m/s)	10
5	chirp_period	period of the sawtooth frequency chirp (in s)	0.002
6	beam_radius	1/e radius of the Gaussian laser beam (in m)	0.004

Table A.3: Simulation parameters for a Monte Carlo simulation of bichromatic slowing with laser frequency chirp.

$\sqrt{3/2}\delta$ and $\phi = -\pi/4$ by default for optimal bichromatic force, so I did not include

these two important parameters in the arguments.

Good practice

- Test run the `RunMC_local_BCF.py` simulation code on your local computer first! You only need to run 1-2 atoms.
- Before submitting a job on Sherlock with full inputs (5000+ atoms), test run on a developer node on Sherlock (1 or few atoms) to make sure QuTiP code and everything runs smoothly. To switch from an interactive node (the default node that you use for job submission) to a developer node, use the command `sdev`. You can use `RunMC_allinput_BCF_chirp.py` but with only one atom as input so you can see right away if something does not work.
- If everything looks good, log out of your developer node, and then you can try submitting 1-2 jobs on Sherlock (on your login node). Experiment with how many atoms, runtime, number of CPU cores, etc.
- If your jobs run smoothly, you are ready to submit more jobs, possibly multiple jobs at once!

Job submission guide

To run a simulation with the example parameters set by the table above, a bash script (.sh) for Sherlock job submission must contain the following line:

```
python3 RunMC_allinput_BCF_chirp.py 100 test.csv 150 10 0.002 0.004
```

Instead of writing a new bash file for every single set of simulation parameters, I find it much easier to automate this process with a Python wrapper. A compatible example script is `submission_files/submit_single_BCF_chirp.py`. I first create three empty folders called `jobs`, `out`, and `err` in my `$SCRATCH/some_folder/$` directory so the newly created files from this Python script can directly go there.

When you have the new folders ready on Sherlock, run the following line to load the Python module (with the version you have)

```
m1 python/3.6.1
```

followed by

```
python3 submit_single_BCF_chirp.py 100 150 10 0.002 0.004
```

This script `submission_files/submit_single_BCF_chirp.py` does the following:

- Create a new bash script (`.sh`) file in the folder `jobs/` using the arguments
- Create an empty text file (`.txt`) in the folder `out/` to store any printed inputs that you can view later
- Create an empty text file (`.txt`) in the folder `err/` to store any error messages that you can view later. This is very useful to see why your code did not run. One of the most frequent error messages I get is a timeout error (code did not finish running within allocated time).
- Automate output file (`.csv`) naming using the parameters. The output will be stored in the file called `100_4mm_150_10_2ms.csv`.
- Submit this job on Sherlock, requesting the resources specified on the script: $c = 32$ CPU cores, $N = 1$ computing node, $\text{time}=0\text{-}04:00$ (4 hours), $\text{mem}=64000$ (memory of 64 GB). I use `p hns` (School of H&S partition) because the wait time is usually shorter than the normal, university-wide partition.

To loop over a set of parameters, see `submit_batch_BCF_chirp.py` for inspiration.

With this script, you can submit up to 100 jobs (daily limit on Sherlock, I think) with only one line of code!

Output file format

A successfully run simulation produces a `.csv` output file with each line representing one atom. Each output line consists of 16 columns as follows.

v_initial(3)	r_initial(3)	t_initial	v_final(3)	r_final(3)	t_final	status	runtime
--------------	--------------	-----------	------------	------------	---------	--------	---------

The status of each atom is given by one of the following strings, ‘PASSED’, ‘TRAPPED’ or ‘FAILED’, which are defined below.

Status	Definition
'PASSED'	The atom moved passed the trap (MOT) region without being trapped.
'TRAPPED'	The atom is successfully slowed and trapped in the MOT.
'FAILED'	The atom ended up moving backwards, away from the trap region.

Table A.4: Simulation statuses for each atom and their definitions.

A.3.4 Simulation script and parameters (Square)

The square-wave version `RunMC_allinput_square_chirp.py` is very similar but with `Rabi_shape` as an additional parameter and slightly different ordering.

sys.argv	Argument	Description	Example
1	δ_{sq}	Modulation frequency (in γ)	110
2	Rabi_shape	Amplitude modulation function (see A.3.2 for options)	2
3	v_max	chirp upper limit in velocity detuning (in m/s)	160
4	v_min	chirp lower limit in velocity detuning (in m/s)	10
5	chirp_period	period of the sawtooth frequency chirp (in s)	0.003
6	beam_radius	1/e radius of the Gaussian laser beam (in m)	0.002
7	filename	.csv output filename	<code>test.csv</code>

Table A.5: Simulation parameters for a Monte Carlo simulation of stimulated slowing with the square-wave force with laser frequency chirp.

Note that $\Omega = \pi\delta_{sq}/4$ and $\phi = 0.36\pi$ by default for optimal square-wave polychromatic force, so I did not include these two important parameters in the arguments.

The script `submission_files/submit_single_squareAM_chirp.py` is a compatible submission script that you can use to submit jobs on Sherlock, similar to how you use the BCF version `submit_single_BCF_chirp.py`.

A.3.5 Generate atom samples `GenerateBatchAtoms.py`

As described in Sec. 3.2.2, atoms in our Monte Carlo simulations are either already moving in the beam region when the slowing laser is turned on, or are leaving the oven at a later time. The script `GenerateBatchAtoms.py` generates 3 output files required for a simulation run:

- `v_input.npy` initial velocities
- `r_input.npy` initial positions
- `t_input.npy` starting times ($t_0 = 0$ means atoms are already in the beam region, $t_0 > 0$ means atoms leave the oven later, after the laser beams are turned on.)

The parameter `flux` is set to 5000 by default. `flux=5000` generates roughly 20,000 atoms total. In the folder The oven radius was set to 2 mm by default even though the actual radius was 4 mm in the experiment. Given our laser power limit, we considered shrinking the oven aperture to reduce the laser beam area required to compensate for the atomic beam divergence. Hence, we used the target oven size of 2 mm in radius for all the simulations.

The three files generated with this script are required for a simulation run. Using the same samples of atoms allow us to compare the loading rates when using different laser intensities, chirp parameters, and other tunable experimental parameters.

Appendix B

Code: Magnetometer

Python codes and documentation for the magnetometer are posted to <https://github.com/tinatn29/Yb-magnetometer>.

B.1 Instructions

- Clone the git repository to your local directory.
- Upload everything to your Sherlock directory `$SCRATCH/some_folder/$`, preserving the folder structure for convenience. To make sure everything runs smoothly on Sherlock, use the checklist below.
 - Class file `ATSolver.py`
 - Main script for the simulation you want to run `RunMC_.py`
 - If `RunMC_.py` requires loading numpy arrays for atoms' velocity and B-field values, make sure those files are in the correct directory. By default, they should be in the folder `configs/`.
 - Sherlock job submission script that specifies computing resources (number of computing nodes, number of CPU cores, memory, runtime) requested. Modify one of the existing Python `submit_.py` files in the folder `submission_files/` or create a new Bash (.sh) file. See A.3.3 for more details.

- On Terminal, `ssh` into Sherlock and navigate to the directory where the files live. Load the Python module with the command `m1 python/3.6.1` (this will depend on which version of Python you installed on Sherlock).
- Submit job(s). `cd` into the correct directory on Sherlock. For a Python submission script use `python3 submit_.py` followed by any required arguments (depending on how you set up the script). For a Bash script use `sbatch submit_.sh`. See [Sherlock documentation](#) for more details.
- To see jobs in the queue use `squeue -u <SUnetID>`
- To cancel a job use `scancel <jobID>`. To cancel all jobs in the queue use `scancel -u <SUnetID>`

B.2 Python libraries used

Make sure you have the following libraries up and running on both your local computer and Sherlock.

- Numpy
- Scipy
- [QuTiP: Quantum Toolbox in Python \[115, 116\]](#)
- Multiprocessing

To process, analyze, and visualize the data, I also use Matplotlib, Pandas, and Jupyter Notebook.

B.3 Descriptions and pseudocodes

For readability and to save space, pseudocodes of the important code files are given in this appendix instead of the full scripts.

B.3.1 Main class file ATSolver.py

This file defines the class `ATSolver`, the functions and parameters within, and helper functions (at the top of the file before the class definition) used for numerical calculations of the fluorescence for a single atom or a batch of atoms (Doppler average). The first part of the code sets up the parameters and helper functions.

```
import relevant libraries

def H0_4fields(args):
    # time-independent part of the 4x4 Hamiltonian (4-level atom)

# functions to define time-dependent portions (t, args)

class ATSolver():
    def __init__():
        # Initialize attributes and parameters used in the
        calculations

    def SolveME_single():
        # Solve the Master's Equation numerically for a single atom
        Set up the Hamiltonian H0, H
        Extract steady-state density matrix elements (average the
        solutions at t > 10*tau)

        # The following parameters are updated (steady-state
        solutions)
        self.rho11: population in the m=1 state
        self.rho22 = population in the m=0 state
        self.rho33 = population in the m=-1 state
        self.rho13_Re = Real part of the coherence between the m=-1
        and 1 states

    def SolveME_single_b_array(vx):
        # This function calculates the density matrix (steady-state)
        for a range (array) of B-field values
        # self.b_array must be set (1D or 2D array) for this
        function to work properly
```

```

    self.args['vx'] = vx # set atom's velocity

    # result array [rho11, rho22, rho33, Re(rho13)] each row (
    each value of b_array)
    result = np.zeros((len(self.b_array), 4))

    for i in range(len(self.b_array)):
        Check the dimensions of b_array -> update self.args['b']
        self.SolveME_single() # solve for the density matrix
        Store results in the result array

    return result # return 2D output array [rho11, rho22, rho33,
Re(rho13)]

def SolveME_parallel_b_array(vx_input, max_cores=32):
    # Calculate Doppler averaged rho from lots of atoms using
parallel computing
    # vx_input corresponds to atoms' velocities we are using

import multiprocessing as mp

    start_time = time.time() # start the runtime clock
n_cores = np.amin([mp.cpu_count(), max_cores])
# Use no. of CPUs available (locally) or 32 cores maximum (
Sherlock cluster)
pool = mp.Pool(processes=n_cores)

results = pool.map(self.SolveME_single_b_array, vx_input) # return
images
print('Time elapsed: {:.2f} sec'.format(time.time() - start_time)
)

    # return the output array from self.SolveME_single_b_array
    for all vx_input
return results

```

B.3.2 Simulation script and parameters

Initialize the ATSolver class

Most RunMC files start by setting the values of `delta_mod` (modulation frequency δ_{mod} in the units of γ), `theta_pol` (polarization angle in degrees), and `light_fields`. Very often these quantities are taken from the arguments, but you can hard code them, too. Typical settings look like

```
delta_mod = 20 # modulation freq = 20*gamma
theta_pol = 90 # theta = 90 degrees (y-polarized light), 0 is for z-
    polarized light
light_fields = [(10, -1), (10, 0), (10, 1)] # This list of tuples
    represents 3 optical fields with all equal Rabi frequencies = 10*
    gamma, at detunings -1*delta_mod, 0 (carrier), and 1*delta_mod
```

Some RunMC_duty scripts incorporate 7 optical fields from the 10% duty square wave (`duty = 0.1`) or 50% duty square wave (`duty = 0.5`), so the light fields are hard coded and look more complicated. Currently, the code only runs if `duty = 0.1` or `duty = 0.5`.

```
light_fields = []
# Set light fields
if duty == 0.1:
    Omega1, Omega2, Omega3 = Omega0 * np.array([0.107, 0.101, 0.091])
    / 0.109 # Fourier amps
    light_fields = [(Omega3, -3), (Omega2, -2), (Omega1, -1), (Omega0,
        0), \
        (Omega1, 1), (Omega2, 2), (Omega3, 3)]
elif duty == 0.5:
    Omega1, Omega3 = Omega0 * np.array([0.318, 0.106]) / 0.5 # Fourier
        amps
    light_fields = [(Omega3, -3), (Omega1, -1), (Omega0, 0), \
        (Omega1, 1), (Omega3, 3)]
else:
    print("ERROR: Duty cycle must be either 0.1 or 0.5")
    sys.exit() # exit program
```

Once you have these parameters ready, the following line will initialize the `ATSolver` class and we are almost ready to solve some equations.

```
from ATSolver import ATSolver # make sure to import this at the
                             header
AT = ATSolver(light_fields, delta_mod, theta_pol)
```

Magnetic fields

Before doing any calculations, another key parameter to set is the magnetic fields. I often use a linear B-field gradient in the z -direction. There are two ways to set `self.b_array`. The first method is to define a 1D Numpy array and pick a direction. For example, a linear B_z field can be set by

```
AT.b_array = np.linspace(-75, 75, 121)
AT.b_direction = 2 # Axis index 0:x, 1:y, 2:z
```

Another compatible format for `self.b_array` is a 2D Numpy array, with each row corresponding to $[b_x, b_y, b_z]$ (in γ). For example,

```
AT.b_array = np.array([0, 0, -75], [0, 0, 75])
# or load from an existing file
AT.b_array = np.load("./configs/b_3D.npy")
```

In my notation, $b = g\mu_B B$, so technically the b parameter we are setting is the Zeeman splitting in the units of γ . I use this notation to make the matrices (and the code) cleaner and we won't have to multiply everything by constants g, μ_B every time. The conversion between frequency $\leftrightarrow B$ is ≈ 2.1 MHz/G. $b = 11.5$ (units of γ) is equivalent to $B = 1$ G.

Atoms' velocities

All `RunMC*.py` files are for calculating Doppler-averaged density matrix ρ for a batch of atoms with velocities given by the array `vx_input`, which can be hard coded in the script (as in `RunMC_test_local.py` to limit the number of atoms) or more often, `vx_input` is loaded from a Numpy array in the `/configs/` folder. For example,

```
vx_input = np.array([0, 0.01]) # test input (2 atoms)
```

```
vx_input = np.load('./configs/vx_input_1000.npy') # load transverse
vx from file (1000 atoms)
```

Note that you can always re-sample the velocities v_x from the Gaussian distribution, but I like the loading method for speed and for comparing results from different polarization angles, so I know that the different results are exclusively caused by different θ (or other parameters) and not from random sampling statistics.

Main step: calculation

After defining all the parameters, the following lines in RunMC files execute the Doppler-averaged density matrix calculations.

```
results = AT.SolveME_parallel_b_array(vx_input)
result = np.mean(results, axis=0) # Taking Doppler average (average
                                results over all atoms' velocities present)
```

Note that the array `results` is a stack of the density matrix elements from all velocities. We calculate the mean down the 0th axis to average the results over all the velocities present, so the final `result` array is what we want and save (as csv).

```
# Filename from argument
np.savetxt('filename.csv', result, delimiter=',') # save result as
                                                csv
```

The final `result` has 4 columns and the same number of rows as `b_array`.

ρ_{11}	ρ_{22}	ρ_{33}	$\text{Re}(\rho_{13})$
-------------	-------------	-------------	------------------------

The total fluorescence and intensity of light emitted along y are calculated later when analyzing and plotting the data. Recall that

$$\text{Total fluorescence} \propto \rho_{11} + \rho_{22} + \rho_{33} \quad (\text{B.1})$$

$$I_y(\text{with Hanle effect}) \propto \rho_{22} + \frac{1}{2}(\rho_{11} + \rho_{33} - 2\text{Re}(\rho_{13})) \quad (\text{B.2})$$

Parameters as arguments

For convenience and scalability, most RunMC files created to run on the Sherlock cluster take parameters as arguments. For example, `RunMC_configs_N_bxby.py` takes

sys.argv	Argument	Description	Example
1	δ_{mod}	Modulation frequency (in γ)	20
2	θ	Polarization angle (in degrees)	90
3	light_fields	laser fields as a list of tuples $[(\Omega_1/\gamma, \Delta_1/\delta_{mod}), (\Omega_2/\gamma, \Delta_2/\delta_{mod}), \dots]$. $[(10,-1), (10,1)]$ is for two driving fields at Rabi frequency 10γ and detunings $\pm\delta_{mod}$	$"[(10,-1), (10,1)]"$
4	b_z array file	1D Numpy array file (.npy) containing b_z values (in γ) from the /configs/ folder	<code>bz_linear_75.npy</code>
5	b_x	x -component $b_x = g\mu_B B_x$ (in γ)	1.5
6	b_y	y -component $b_y = g\mu_B B_y$ (in γ)	4.3
7	N	number of atoms (500 or 1000)	1000
8	filename	.csv output filename	<code>test.csv</code>

Table B.1: Simulation parameters for Doppler-averaged fluorescence calculations.

the following arguments

Good practice

- Test run the `RunMC_test_local.py` code on your local computer first! You only need to run 1-2 atoms.
- Before submitting a job on Sherlock with full inputs (1000+ atoms), test run on a developer node on Sherlock (1 or few atoms) to make sure QuTiP code and everything runs smoothly. To switch from an interactive node (the default node that you use for job submission) to a developer node, use the command `sdev`.
- If everything looks good, log out of your developer node, and then you can try submitting 1-2 jobs on Sherlock (on your login node). Experiment with how many atoms, runtime, number of CPU cores, etc.
- If your jobs run smoothly, you are ready to submit more jobs, possibly multiple

jobs at once!

B.3.3 Job submission guide

To run a simulation with the example parameters set by the table on the previous page, a bash script (.sh) for Sherlock job submission must contain the following line:

```
python3 RunMC_configs_N_bxby.py 20 90 "[(-10,-1),(10,1)]"  
bz_linear_75.npy 1.5 4.3 1000 test.csv
```

When I need to loop over many experiment parameters, for example, to create a 2D contour map of fluorescence, I find it much easier to automate the job submission script generation with a Python wrapper. The python wrapper script will create as many .sh bash files as the number of jobs I want to submit. A compatible example script is `submission_files/submit_2Dmap_bxbz.py`. I used this to calculate all linescans needed to plot a 2D (b_x, b_z) contour. Before running anything, I first create three empty folders called `jobs`, `out`, and `err` in my `$SCRATCH/some_folder/$` directory so the newly created files (.sh bash files, .out files, and .err error messages) from this Python script can directly go there. When you have these new folders ready on Sherlock, run the following line to load the Python module (with the version you have)

```
ml python/3.6.1
```

followed by

```
python3 submit_2Dmap_bxbz.py 20 90 "[(-10,-1),(10,0),(10,1)]"
```

This script `submission_files/submit_2Dmap_bxbz.py` submits 51 jobs to Sherlock, corresponding to 51 linescans, each with a linear b_z gradient ($-25\gamma \leq b_z \leq 25\gamma$) and a constant b_x . The script loops over the values of $-25\gamma \leq b_y \leq 25\gamma$ to submit one job per value of b_x . I later combine 51 line plots from these jobs to produce a 2D contour map. For each job, the script does the following.

- Create a new bash script (.sh) file in the folder `jobs/` using the arguments
- Create an empty text file (.txt) in the folder `out/` to store any printed inputs that you can view later

- Create an empty text file (.txt) in the folder err/ to store any error messages that you can view later. This is very useful to see why your code did not run. One of the most frequent error messages I get is a timeout error (code did not finish running within allocated time).
- Automate output file (.csv) naming using the parameters. The output will be stored in the file called `2Dmap_bxby_delta_mod_thetadeg_bxbx_byby.csv`.
- Submit this job on Sherlock, requesting the resources specified on the script: $c = 32$ CPU cores, $N = 1$ computing node, `time=0-03:00` (3 hours), `mem=64000` (memory of 64 GB). I use `p hns` (School of H&S partition) because the wait time is usually shorter than the normal, university-wide partition.

Modification: duty cycle

Instead of specifying the individual Rabi frequencies and detunings via the `light_fields` argument, some submission scripts take `Omega0` and `duty` to generate light fields that correspond to the carrier and the first 3 harmonics of a square wave. As stated previously `duty` can be either 0.1 or 0.5, but most of our experimental data were taken with `duty = 0.1` (10% duty cycle).

The parameter `Omega0` refers to Ω_0 , the Rabi frequency of the carrier field in units of γ . As described in Sec. 8.4.1, given the carrier $\Omega_0 = 10\gamma$, the first, second, and third harmonic sidebands will automatically have the Rabi frequencies of $\approx 9.8\gamma$, 9.3γ , and 8.3γ , respectively. These relative magnitudes of the Rabi frequencies are hard coded in all `RunMC_duty*.py` scripts. Typically I set $5\gamma \leq \Omega_0 \leq 10\gamma$.

Bibliography

- [1] N. Poli, C. Oates, P. Gill, and G. Tino, “Optical atomic clocks,” *La Rivista del Nuovo Cimento*, vol. 36, no. 12, pp. 55–624, 2013.
- [2] A. Jenkins, J. W. Lis, A. Senoo, W. F. McGrew, and A. M. Kaufman, “Ytterbium nuclear-spin qubits in an optical tweezer array,” *Physical Review X*, vol. 12, no. 2, p. 021027, 2022.
- [3] A. Derevianko, K. Gibble, L. Hollberg, N. R. Newbury, C. Oates, M. S. Safronova, L. C. Sinclair, and N. Yu, “Fundamental physics with a state-of-the-art optical clock in space,” *Quantum Science and Technology*, vol. 7, no. 4, p. 044002, 2022.
- [4] W. McGrew, X. Zhang, R. Fasano, S. Schäffer, K. Beloy, D. Nicolodi, R. Brown, N. Hinkley, G. Milani, M. Schioppo, *et al.*, “Atomic clock performance enabling geodesy below the centimetre level,” *Nature*, vol. 564, no. 7734, pp. 87–90, 2018.
- [5] T. N. Narong, T. Liu, N. Raghuram, and L. Hollberg, “Stimulated slowing of yb atoms on the narrow $1\text{ s }0 \rightarrow 3\text{ p }1$ transition,” *Physical Review A*, vol. 104, no. 5, p. 053117, 2021.
- [6] H. Metcalf, “Colloquium: Strong optical forces on atoms in multifrequency light,” *Reviews of Modern Physics*, vol. 89, p. 041001, Oct. 2017.
- [7] A. Goepfert, I. Bloch, D. Haubrich, F. Lison, R. Schütze, R. Wynands, and D. Meschede, “Stimulated focusing and deflection of an atomic beam using picosecond laser pulses,” *Physical Review A*, vol. 56, pp. R3354–R3357, Nov. 1997.

- [8] V. Voitsekhovich, M. Danielko, A. Negriiko, V. Romanenko, and L. Yatsenko, “Stimulated light pressure on atoms in counter-propagating amplitude modulated waves,” *Sov. Phys. JETP*, vol. 72, pp. 219–227, 1991.
- [9] R. Grimm, Y. B. Ovchinnikov, A. Sidorov, and V. Letokhov, “Observation of a strong rectified dipole force in a bichromatic standing light wave,” *Physical review letters*, vol. 65, no. 12, p. 1415, 1990.
- [10] J. Söding, R. Grimm, Y. B. Ovchinnikov, P. Bouyer, and C. Salomon, “Short-Distance Atomic Beam Deceleration with a Stimulated Light Force,” *Physical Review Letters*, vol. 78, pp. 1420–1423, Feb. 1997.
- [11] T. Lu, X. Miao, and H. Metcalf, “Bloch theorem on the Bloch sphere,” *Physical Review A*, vol. 71, p. 061405, June 2005.
- [12] T. Lu, X. Miao, and H. Metcalf, “Nonadiabatic transitions in finite-time adiabatic rapid passage,” *Physical Review A*, vol. 75, no. 6, p. 063422, 2007.
- [13] X. Miao, E. Wertz, M. G. Cohen, and H. Metcalf, “Strong optical forces from adiabatic rapid passage,” *Physical Review A*, vol. 75, p. 011402, Jan. 2007.
- [14] D. Stack, J. Elgin, P. M. Anisimov, and H. Metcalf, “Numerical studies of optical forces from adiabatic rapid passage,” *Physical Review A*, vol. 84, no. 1, p. 013420, 2011.
- [15] M. R. Williams, F. Chi, M. T. Cashen, and H. Metcalf, “Measurement of the bichromatic optical force on Rb atoms,” *Physical Review A*, vol. 60, pp. R1763–R1766, Sept. 1999.
- [16] M. R. Williams, F. Chi, M. T. Cashen, and H. Metcalf, “Bichromatic force measurements using atomic beam deflections,” *Physical Review A*, vol. 61, p. 023408, Jan. 2000.
- [17] T. C. Liebisch, E. Blanshan, E. A. Donley, and J. Kitching, “Atom-number amplification in a magneto-optical trap via stimulated light forces,” *Physical Review A*, vol. 85, p. 013407, Jan. 2012.

- [18] I. Kozyryev, L. Baum, L. Aldridge, P. Yu, E. E. Eyler, and J. M. Doyle, “Coherent bichromatic force deflection of molecules,” *Physical review letters*, vol. 120, no. 6, p. 063205, 2018.
- [19] S. Galica, L. Aldridge, D. McCarron, E. Eyler, and P. Gould, “Deflection of a molecular beam using the bichromatic stimulated force,” *Physical Review A*, vol. 98, no. 2, p. 023408, 2018.
- [20] A. Guttridge, S. A. Hopkins, S. L. Kemp, D. Boddy, R. Freytag, M. P. A. Jones, M. R. Tarbutt, E. A. Hinds, and S. L. Cornish, “Direct loading of a large Yb MOT on the $^1\text{s}_0 \rightarrow ^3\text{p}_1$ transition,” *Journal of Physics B: Atomic, Molecular and Optical Physics*, vol. 49, p. 145006, June 2016.
- [21] S. E. Galica, L. Aldridge, and E. E. Eyler, “Four-color stimulated optical forces for atomic and molecular slowing,” *Physical Review A*, vol. 88, p. 043418, Oct. 2013.
- [22] F. Primdahl, “The fluxgate magnetometer,” *Journal of Physics E: Scientific Instruments*, vol. 12, p. 241, Apr. 1979.
- [23] P. Ripka, “Advances in fluxgate sensors,” *Sensors and Actuators A: Physical*, vol. 106, pp. 8–14, Sept. 2003.
- [24] R. S. Popovic, *Hall effect devices*. CRC Press, 2003.
- [25] R. L. Fagaly, “Superconducting quantum interference device instruments and applications,” *Review of Scientific Instruments*, vol. 77, p. 101101, Oct. 2006.
- [26] J. Clarke and A. I. Braginski, *The SQUID Handbook*. John Wiley & Sons, Ltd, 1 ed., 2004.
- [27] K. Jensen, P. Kehayias, and D. Budker, “Magnetometry with Nitrogen-Vacancy Centers in Diamond,” in *High Sensitivity Magnetometers* (A. Grosz, M. J. Haji-Sheikh, and S. C. Mukhopadhyay, eds.), Smart Sensors, Measurement and Instrumentation, pp. 553–576, Cham: Springer International Publishing, 2017.

- [28] D. Budker, W. Gawlik, D. F. Kimball, S. M. Rochester, V. V. Yashchuk, and A. Weis, “Resonant nonlinear magneto-optical effects in atoms,” *Reviews of Modern Physics*, vol. 74, pp. 1153–1201, Nov. 2002.
- [29] E. B. Alexandrov, M. Auzinsh, D. Budker, D. F. Kimball, S. M. Rochester, and V. V. Yashchuk, “Dynamic effects in nonlinear magneto-optics of atoms and molecules,” *JOSA B*, vol. 22, no. 1, pp. 7–20, 2005.
- [30] D. Budker and M. Romalis, “Optical magnetometry,” *Nature Physics*, vol. 3, pp. 227–234, Apr. 2007.
- [31] P. D. Schwindt, S. Knappe, V. Shah, L. Hollberg, J. Kitching, L.-A. Liew, and J. Moreland, “Chip-scale atomic magnetometer,” *Applied Physics Letters*, vol. 85, no. 26, pp. 6409–6411, 2004.
- [32] D. Budker and D. F. J. Kimball, *Optical magnetometry*. Cambridge University Press, 2013.
- [33] A. Fabricant, I. Novikova, and G. Bison, “How to build a magnetometer with thermal atomic vapor: A tutorial,” *New Journal of Physics*, vol. 25, p. 025001, Feb. 2023.
- [34] S. H. Autler and C. H. Townes, “Stark Effect in Rapidly Varying Fields,” *Physical Review*, vol. 100, pp. 703–722, Oct. 1955.
- [35] W. Hanle, “Über magnetische beeinflussung der polarisation der resonanzfluoreszenz,” *Zeitschrift für Physik*, vol. 30, no. 1, pp. 93–105, 1924.
- [36] W. Hanle and H. Kleinpoppen, eds., *Progress in Atomic Spectroscopy: Part A*. Boston, MA: Springer US, 1978.
- [37] M. Fleischhauer, A. Imamoglu, and J. P. Marangos, “Electromagnetically induced transparency: Optics in coherent media,” *Reviews of Modern Physics*, vol. 77, pp. 633–673, July 2005.

- [38] E. Arimondo, “V Coherent Population Trapping in Laser Spectroscopy,” in *Progress in Optics* (E. Wolf, ed.), vol. 35, pp. 257–354, Elsevier, Jan. 1996.
- [39] H. Lee, M. Fleischhauer, and M. O. Scully, “Sensitive detection of magnetic fields including their orientation with a magnetometer based on atomic phase coherence,” *Physical Review A*, vol. 58, pp. 2587–2595, Sept. 1998.
- [40] K. Cox, V. I. Yudin, A. V. Taichenachev, I. Novikova, and E. E. Mikhailov, “Measurements of the magnetic field vector using multiple electromagnetically induced transparency resonances in Rb vapor,” *Physical Review A*, vol. 83, p. 015801, Jan. 2011.
- [41] B. C. Das, B. C. Das, A. Das, D. Bhattacharyya, and S. De, “Effects of vector magnetic field on electromagnetically induced transparency with $\text{lin} \perp \text{lin}$ polarization,” *JOSA B*, vol. 38, pp. 584–594, Feb. 2021.
- [42] S. Qiu, J. Wang, J. Wang, F. Castellucci, M. Cao, M. Cao, S. Zhang, T. W. Clark, S. Franke-Arnold, H. Gao, and F. Li, “Visualization of magnetic fields with cylindrical vector beams in a warm atomic vapor,” *Photonics Research*, vol. 9, pp. 2325–2331, Dec. 2021.
- [43] C. Affolderbach, M. Stähler, S. Knappe, and R. Wynands, “An all-optical, high-sensitivity magnetic gradiometer,” *Applied Physics B*, vol. 75, pp. 605–612, 2002.
- [44] S. Pradhan, R. Behera, and A. K. Das, “Polarization rotation under two-photon Raman resonance for magnetometry,” *Applied Physics Letters*, vol. 100, p. 173502, Apr. 2012.
- [45] K. A. Barantsev, S. V. Bozhokin, A. S. Kuraptsev, A. N. Litvinov, and I. M. Sokolov, “Coherent population trapping in optically thin ^{133}Cs atomic vapor in a finite-size cell,” *JOSA B*, vol. 38, pp. 1613–1624, May 2021.
- [46] G. S. Pati, R. Tripathi, R. S. Grewal, M. Pulido, and R. A. Depto, “Synchronous coherent population trapping and its magnetic spectral response in rubidium vapor,” *Physical Review A*, vol. 104, p. 033116, Sept. 2021.

- [47] J. Belfi, G. Bevilacqua, V. Biancalana, Y. Dancheva, and L. Moi, “All optical sensor for automated magnetometry based on coherent population trapping,” *JOSA B*, vol. 24, no. 7, pp. 1482–1489, 2007.
- [48] G. Bison, V. Bondar, P. Schmidt-Wellenburg, A. Schnabel, and J. Voigt, “Sensitive and stable vector magnetometer for operation in zero and finite fields,” *Optics Express*, vol. 26, pp. 17350–17359, June 2018.
- [49] J. S. Jackson and D. S. Durfee, “Magneto-Optical Trap Field Characterization with the Directional Hanle Effect,” *Scientific Reports*, vol. 9, p. 8896, June 2019.
- [50] F. Castellucci, T. W. Clark, A. Selyem, J. Wang, and S. Franke-Arnold, “Atomic Compass: Detecting 3D Magnetic Field Alignment with Vector Vortex Light,” *Physical Review Letters*, vol. 127, p. 233202, Nov. 2021.
- [51] M. Vengalattore, J. M. Higbie, S. R. Leslie, J. Guzman, L. E. Sadler, and D. M. Stamper-Kurn, “High-Resolution Magnetometry with a Spinor Bose-Einstein Condensate,” *Physical Review Letters*, vol. 98, p. 200801, May 2007.
- [52] F. Yang, A. J. Kollár, S. F. Taylor, R. W. Turner, and B. L. Lev, “Scanning Quantum Cryogenic Atom Microscope,” *Physical Review Applied*, vol. 7, p. 034026, Mar. 2017.
- [53] S. H. Autler and C. H. Townes, “Stark effect in rapidly varying fields,” *Physical Review*, vol. 100, no. 2, p. 703, 1955.
- [54] L. Novikov, G. Skrotskiĭ, and G. I. Solomakho, “The hanle effect,” *Soviet Physics Uspekhi*, vol. 17, no. 4, p. 542, 1975.
- [55] C. J. Foot, *Atomic physics*, vol. 7. OUP Oxford, 2004.
- [56] H. J. Metcalf and P. V. d. Straten, *Laser cooling and trapping*. Springer, 2002.
- [57] J. Emsley, *The elements*. Oxford University Press, 2000.

- [58] A. Jenkins, J. W. Lis, A. Senoo, W. F. McGrew, and A. M. Kaufman, “Ytterbium nuclear-spin qubits in an optical tweezer array,” *Physical Review X*, vol. 12, no. 2, p. 021027, 2022.
- [59] S. Ma, A. P. Burgers, G. Liu, J. Wilson, B. Zhang, and J. D. Thompson, “Universal gate operations on nuclear spin qubits in an optical tweezer array of ^{171}Yb atoms,” *Phys. Rev. X*, vol. 12, p. 021028, May 2022.
- [60] S. Sugawa, R. Yamazaki, S. Taie, and Y. Takahashi, “Bose-einstein condensate in gases of rare atomic species,” *Physical Review A*, vol. 84, no. 1, p. 011610, 2011.
- [61] H. Hara, Y. Takasu, Y. Yamaoka, J. M. Doyle, and Y. Takahashi, “Quantum degenerate mixtures of alkali and alkaline-earth-like atoms,” *Physical review letters*, vol. 106, no. 20, p. 205304, 2011.
- [62] J. P. Covey, A. Sipahigil, S. Szoke, N. Sinclair, M. Endres, and O. Painter, “Telecom-band quantum optics with ytterbium atoms and silicon nanophotonics,” *Physical Review Applied*, vol. 11, no. 3, p. 034044, 2019.
- [63] J. Hartwig, S. Abend, C. Schubert, D. Schlippert, H. Ahlers, K. Posso-Trujillo, N. Gaaloul, W. Ertmer, and E. M. Rasel, “Testing the universality of free fall with rubidium and ytterbium in a very large baseline atom interferometer,” *New Journal of Physics*, vol. 17, no. 3, p. 035011, 2015.
- [64] T. H. Loftus, “Laser cooling and trapping of atomic ytterbium,” *Ph.D. Thesis, University of Oregon*, 2001.
- [65] W. D. Phillips and H. Metcalf, “Laser deceleration of an atomic beam,” *Physical Review Letters*, vol. 48, no. 9, p. 596, 1982.
- [66] T. H. Loftus, A. Vitouchkine, and L. Hollberg, “Permanent magnet axial field zeeman slower,” *Patent No. US8710428B1*, 2014.

- [67] E. Wodey, R. Rengelink, C. Meiners, E. Rasel, and D. Schlippert, “A robust, high-flux source of laser-cooled ytterbium atoms,” *Journal of Physics B: Atomic, Molecular and Optical Physics*, vol. 54, no. 3, p. 035301, 2021.
- [68] P. D. Lett, W. D. Phillips, S. Rolston, C. E. Tanner, R. Watts, and C. Westbrook, “Optical molasses,” *JOSA B*, vol. 6, no. 11, pp. 2084–2107, 1989.
- [69] R. Maruyama, R. Wynar, M. Romalis, A. Andalkar, M. Swallows, C. Pearson, and E. Fortson, “Investigation of sub-doppler cooling in an ytterbium magneto-optical trap,” *Physical Review A*, vol. 68, no. 1, p. 011403, 2003.
- [70] N. Poli, Z. W. Barber, N. D. Lemke, C. W. Oates, L. Ma, J. E. Stalnaker, T. Fortier, S. Diddams, L. Hollberg, J. Bergquist, *et al.*, “Frequency evaluation of the doubly forbidden $s\ 0\ 1 \rightarrow p\ 0\ 3$ transition in bosonic $yb\ 174$,” *Physical Review A*, vol. 77, no. 5, p. 050501, 2008.
- [71] T. Kohno, M. Yasuda, K. Hosaka, H. Inaba, Y. Nakajima, and F.-L. Hong, “One-dimensional optical lattice clock with a fermionic $171yb$ isotope,” *Applied Physics Express*, vol. 2, no. 7, p. 072501, 2009.
- [72] K. Pandey, K. D. Rathod, A. K. Singh, and V. Natarajan, “Atomic fountain of laser-cooled Yb atoms for precision measurements,” *Physical Review A*, vol. 82, p. 043429, Oct. 2010.
- [73] C. Y. Park, D.-H. Yu, W.-K. Lee, S. E. Park, E. B. Kim, S. K. Lee, J. W. Cho, T. H. Yoon, J. Mun, S. J. Park, *et al.*, “Absolute frequency measurement of $1s0$ ($f=1/2$)– $3p0$ ($f=1/2$) transition of $171yb$ atoms in a one-dimensional optical lattice at kriss,” *Metrologia*, vol. 50, no. 2, p. 119, 2013.
- [74] A. Kawasaki, B. Braverman, Q. Yu, and V. Vuletic, “Two-color magneto-optical trap with small magnetic field for ytterbium,” *Journal of Physics B: Atomic, Molecular and Optical Physics*, vol. 48, p. 155302, June 2015.
- [75] J. Lee, J. H. Lee, J. Noh, and J. Mun, “Core-shell magneto-optical trap for alkaline-earth-metal-like atoms,” *Physical Review A*, vol. 91, no. 5, p. 053405, 2015.

- [76] Z. Peng-Yii, X. Zhuan-Xian, L. Yun, H. Ling-Xiang, and L. Bao-Long, “Realization of Green MOT for Ytterbium Atoms,” *Chinese Physics Letters*, vol. 26, p. 083702, Aug. 2009.
- [77] V. V. Ivanov, A. Khramov, A. H. Hansen, W. H. Dowd, F. Münchow, A. O. Jamison, and S. Gupta, “Sympathetic Cooling in an Optically Trapped Mixture of Alkali and Spin-Singlet Atoms,” *Physical Review Letters*, vol. 106, p. 153201, Apr. 2011.
- [78] S. Dörscher, A. Thobe, B. Hundt, A. Kochanke, R. Le Targat, P. Windpassinger, C. Becker, and K. Sengstock, “Creation of quantum-degenerate gases of ytterbium in a compact 2d-/3d-magneto-optical trap setup,” *Review of Scientific Instruments*, vol. 84, no. 4, p. 043109, 2013.
- [79] Y. Takasu, K. Honda, K. Komori, T. Kuwamoto, M. Kumakura, Y. Takahashi, and T. Yabuzaki, “High-density trapping of cold ytterbium atoms by an optical dipole force,” *Physical review letters*, vol. 90, no. 2, p. 023003, 2003.
- [80] C. Grain, T. Nazarova, C. Degenhardt, F. Vogt, C. Lisdat, E. Tiemann, U. Sterr, and F. Riehle, “Feasibility of narrow-line cooling in optical dipole traps,” *The European Physical Journal D*, vol. 42, no. 2, pp. 317–324, 2007.
- [81] C.-C. Chen, S. Bennetts, R. G. Escudero, F. Schreck, B. Pasquiou, *et al.*, “Sisyphus optical lattice decelerator,” *Physical Review A*, vol. 100, no. 2, p. 023401, 2019.
- [82] V. Voitsekhovich, M. Danileiko, A. Negriiko, V. Romanenko, and L. Yatsenko, “Observation of a stimulated radiation pressure of amplitude-modulated light on atoms,” *JETP Lett*, vol. 49, p. 161, 1989.
- [83] A. Kazantsev and I. Krasnov, “Rectification effect of a radiation force,” *JOSA B*, vol. 6, no. 11, pp. 2140–2148, 1989.
- [84] J. McGuirk, M. Snadden, and M. Kasevich, “Large area light-pulse atom interferometry,” *Physical review letters*, vol. 85, no. 21, p. 4498, 2000.

- [85] H. Müller, S.-w. Chiow, Q. Long, S. Herrmann, and S. Chu, “Atom interferometry with up to 24-photon-momentum-transfer beam splitters,” *Physical review letters*, vol. 100, no. 18, p. 180405, 2008.
- [86] S.-w. Chiow, T. Kovachy, H.-C. Chien, and M. A. Kasevich, “102 $\hbar k$ large area atom interferometers,” *Physical review letters*, vol. 107, no. 13, p. 130403, 2011.
- [87] T. Wilkason, M. Nantel, J. Rudolph, Y. Jiang, B. E. Garber, H. Swan, S. P. Carman, M. Abe, J. M. Hogan, *et al.*, “Atom interferometry with floquet atom optics,” *Physical Review Letters*, vol. 129, no. 18, p. 183202, 2022.
- [88] E. Ilinova, M. Ahmad, and A. Derevianko, “Doppler cooling with coherent trains of laser pulses and a tunable velocity comb,” *Physical Review A*, vol. 84, p. 033421, Sept. 2011.
- [89] E. Ilinova and A. Derevianko, “Doppler cooling of three-level Λ systems by coherent pulse trains,” *Physical Review A*, vol. 86, p. 023417, Aug. 2012.
- [90] L. Yatsenko and H. Metcalf, “Dressed-atom description of the bichromatic force,” *Physical Review A*, vol. 70, p. 063402, Dec. 2004.
- [91] R. Grimm, J. Söding, and Y. B. Ovchinnikov, “Coherent beam splitter for atoms based on a bichromatic standing light wave,” *Optics letters*, vol. 19, no. 9, pp. 658–660, 1994.
- [92] L. Landau, “On the theory of transfer of energy at collisions ii,” *Phys. Z. Sowjetunion*, vol. 2, no. 46, p. 118, 1932.
- [93] C. Zener, “Non-adiabatic crossing of energy levels,” *Proceedings of the Royal Society of London. Series A, Containing Papers of a Mathematical and Physical Character*, vol. 137, no. 833, pp. 696–702, 1932.
- [94] X. Hua, C. Corder, and H. Metcalf, “Simulation of laser cooling by the bichromatic force,” *Physical Review A*, vol. 93, p. 063410, June 2016.

- [95] M. Cashen, O. Rivoire, V. Romanenko, L. Yatsenko, and H. Metcalf, "Strong optical forces in frequency-modulated light," *Physical Review A*, vol. 64, p. 063411, Nov. 2001.
- [96] M. Partlow, X. Miao, J. Bochmann, M. Cashen, and H. Metcalf, "Bichromatic slowing and collimation to make an intense helium beam," *Physical review letters*, vol. 93, no. 21, p. 213004, 2004.
- [97] M. A. Chieda and E. E. Eyler, "Bichromatic Slowing of Metastable Helium," *Physical Review A*, vol. 86, p. 053415, Nov. 2012.
- [98] Z. Feng, S. Ebser, L. Ringena, F. Ritterbusch, and M. K. Oberthaler, "Bichromatic force on metastable argon for atom-trap trace analysis," *Physical Review A*, vol. 96, no. 1, p. 013424, 2017.
- [99] M. A. Chieda and E. E. Eyler, "Prospects for rapid deceleration of small molecules by optical bichromatic forces," *Physical Review A*, vol. 84, p. 063401, Dec. 2011.
- [100] D. Dai, Y. Xia, Y. Fang, L. Xu, Y. Yin, X. Li, X. Yang, and J. Yin, "Efficient stimulated slowing and cooling of the magnesium fluoride molecular beam," *Journal of Physics B: Atomic, Molecular and Optical Physics*, vol. 48, no. 8, p. 085302, 2015.
- [101] E. Ilinova, J. Weinstein, and A. Derevianko, "Stimulated deceleration of diatomic molecules on multiple rovibrational transitions with coherent pulse trains," *New Journal of Physics*, vol. 17, no. 5, p. 055003, 2015.
- [102] L. Aldridge, S. E. Galica, and E. E. Eyler, "Simulations of the bichromatic force in multilevel systems," *Physical Review A*, vol. 93, p. 013419, Jan. 2016.
- [103] Y. Yin, S. Xu, M. Xia, Y. Xia, and J. Yin, "Optically stimulated slowing of polar heavy-atom molecules with a constant beat phase," *Physical Review A*, vol. 97, no. 4, p. 043403, 2018.

- [104] K. Wenz, I. Kozyryev, R. L. McNally, L. Aldridge, and T. Zelevinsky, “Large molasses-like cooling forces for molecules using polychromatic optical fields: A theoretical description,” *Physical Review Research*, vol. 2, p. 043377, Dec. 2020.
- [105] M. A. Norcia, J. R. Cline, J. P. Bartolotta, M. J. Holland, and J. K. Thompson, “Narrow-line laser cooling by adiabatic transfer,” *New Journal of Physics*, vol. 20, no. 2, p. 023021, 2018.
- [106] N. Petersen, F. Mühlbauer, L. Bougas, A. Sharma, D. Budker, and P. Windpassinger, “Sawtooth-wave adiabatic-passage slowing of dysprosium,” *Physical Review A*, vol. 99, no. 6, p. 063414, 2019.
- [107] S. Malinovskaya, “Laser cooling using adiabatic rapid passage,” *Frontiers of Physics*, vol. 16, no. 5, pp. 1–1, 2021.
- [108] J. P. Bartolotta, M. A. Norcia, J. R. Cline, J. K. Thompson, and M. J. Holland, “Laser cooling by sawtooth-wave adiabatic passage,” *Physical Review A*, vol. 98, no. 2, p. 023404, 2018.
- [109] J. P. Bartolotta and M. J. Holland, “Sawtooth-wave adiabatic passage in a magneto-optical trap,” *Physical Review A*, vol. 101, no. 5, p. 053434, 2020.
- [110] W. C. Magno, R. L. Cavasso Filho, and F. C. Cruz, “Two-photon doppler cooling of alkaline-earth-metal and ytterbium atoms,” *Physical Review A*, vol. 67, no. 4, p. 043407, 2003.
- [111] B. Plotkin-Swing, A. Wirth, D. Gochnauer, T. Rahman, K. E. McAlpine, and S. Gupta, “Crossed-beam slowing to enhance narrow-line ytterbium magneto-optic traps,” *Review of Scientific Instruments*, vol. 91, no. 9, p. 093201, 2020.
- [112] E. Curtis, C. W. Oates, and L. Hollberg, “Quenched narrow-line laser cooling of 40 ca to near the photon recoil limit,” *Physical Review A*, vol. 64, no. 3, p. 031403, 2001.

- [113] O. Prudnikov, R. Y. Il'Enkov, A. Taichenachev, and V. Yudin, “Scaling law in laser cooling on narrow-line optical transitions,” *Physical Review A*, vol. 99, no. 2, p. 023427, 2019.
- [114] C.-C. Chen, S. Bennetts, R. G. Escudero, B. Pasquiou, F. Schreck, *et al.*, “Continuous guided strontium beam with high phase-space density,” *Physical Review Applied*, vol. 12, no. 4, p. 044014, 2019.
- [115] J. R. Johansson, P. D. Nation, and F. Nori, “QuTiP: An open-source Python framework for the dynamics of open quantum systems,” *Computer Physics Communications*, vol. 183, pp. 1760–1772, Aug. 2012.
- [116] J. R. Johansson, P. D. Nation, and F. Nori, “QuTiP 2: A Python framework for the dynamics of open quantum systems,” *Computer Physics Communications*, vol. 184, pp. 1234–1240, Apr. 2013.
- [117] V. Minogin and O. Serimaa, “Resonant light pressure forces in a strong standing laser wave,” *Optics Communications*, vol. 30, no. 3, pp. 373–379, 1979.
- [118] B. D. Flury, “Acceptance–rejection sampling made easy,” *Siam Review*, vol. 32, no. 3, pp. 474–476, 1990.
- [119] S. Glen, “Wald ci,” Feb 2022.
- [120] J. Hoffnagle, “Proposal for continuous white-light cooling of an atomic beam,” *Optics letters*, vol. 13, no. 2, pp. 102–104, 1988.
- [121] H. Wallis and W. Ertmer, “Broadband laser cooling on narrow transitions,” *JOSA B*, vol. 6, no. 11, pp. 2211–2219, 1989.
- [122] M. Zhu, C. W. Oates, and J. L. Hall, “Continuous high-flux monovelocity atomic beam based on a broadband laser-cooling technique,” *Physical review letters*, vol. 67, no. 1, p. 46, 1991.
- [123] M. Watanabe, R. Ohmukai, U. Tanaka, K. Hayasaka, H. Imajo, and S. Urabe, “Velocity control of an yb beam by a frequency-doubled mode-locked laser,” *JOSA B*, vol. 13, no. 11, pp. 2377–2381, 1996.

- [124] T. H. Loftus, T. Ido, M. M. Boyd, A. D. Ludlow, and J. Ye, “Narrow line cooling and momentum-space crystals,” *Physical Review A*, vol. 70, no. 6, p. 063413, 2004.
- [125] W. D. Phillips, J. V. Prodan, and H. J. Metcalf, “Laser cooling and electro-magnetic trapping of neutral atoms,” *JOSA B*, vol. 2, no. 11, pp. 1751–1767, 1985.
- [126] L. Moi, “Application of a very long cavity laser to atom slowing down and optical pumping,” *Optics communications*, vol. 50, no. 6, pp. 349–352, 1984.
- [127] V. G. Minogin and V. S. Letokhov, *Laser light pressure on atoms*, p. 131. CRC Press, 1987.
- [128] J. Lenz, “A review of magnetic sensors,” *Proceedings of the IEEE*, vol. 78, pp. 973–989, June 1990.
- [129] J. Lenz and S. Edelstein, “Magnetic sensors and their applications,” *IEEE Sensors Journal*, vol. 6, pp. 631–649, June 2006.
- [130] P. W. Courteille, S. R. Muniz, K. Magalhães, R. Kaiser, L. G. Marcassa, and V. S. Bagnato, “Magnetic field tomography,” *The European Physical Journal D-Atomic, Molecular, Optical and Plasma Physics*, vol. 15, pp. 173–180, 2001.
- [131] C. V. Nielsen, J. Lyngsø, A. Thorseth, M. Galouzis, K. Therkildsen, E. van Ooijen, and J. Thomsen, “Characterization of a magnetic trap by polarization dependent zeeman spectroscopy,” *The European Physical Journal D*, vol. 48, pp. 111–119, 2008.
- [132] N. Behbood, F. Martin Ciurana, G. Colangelo, M. Napolitano, M. W. Mitchell, and R. J. Sewell, “Real-time vector field tracking with a cold-atom magnetometer,” *Applied Physics Letters*, vol. 102, p. 173504, Apr. 2013.
- [133] B. Patton, E. Zhivun, D. C. Hovde, and D. Budker, “All-Optical Vector Atomic Magnetometer,” *Physical Review Letters*, vol. 113, p. 013001, July 2014.

- [134] L. Lenci, A. Auyuanet, S. Barreiro, P. Valente, A. Lezama, and H. Failache, “Vectorial atomic magnetometer based on coherent transients of laser absorption in Rb vapor,” *Physical Review A*, vol. 89, p. 043836, Apr. 2014.
- [135] R. J. Cooper, D. W. Prescott, P. Matz, K. L. Sauer, N. Dural, M. V. Romalis, E. L. Foley, T. W. Kornack, M. Monti, and J. Okamitsu, “Atomic Magnetometer Multisensor Array for rf Interference Mitigation and Unshielded Detection of Nuclear Quadrupole Resonance,” *Physical Review Applied*, vol. 6, p. 064014, Dec. 2016.
- [136] T. Thiele, Y. Lin, M. O. Brown, and C. A. Regal, “Self-Calibrating Vector Atomic Magnetometry through Microwave Polarization Reconstruction,” *Physical Review Letters*, vol. 121, p. 153202, Oct. 2018.
- [137] S. J. Ingleby, C. O’Dwyer, P. F. Griffin, A. S. Arnold, and E. Riis, “Vector Magnetometry Exploiting Phase-Geometry Effects in a Double-Resonance Alignment Magnetometer,” *Physical Review Applied*, vol. 10, p. 034035, Sept. 2018.
- [138] T. Pyragius, H. M. Florez, and T. Fernholz, “Voigt-effect-based three-dimensional vector magnetometer,” *Physical Review A*, vol. 100, p. 023416, Aug. 2019.
- [139] B. Cai, C.-P. Hao, Z.-R. Qiu, Q.-Q. Yu, W. Xiao, and D. Sheng, “Herriott-cavity-assisted all-optical atomic vector magnetometer,” *Physical Review A*, vol. 101, p. 053436, May 2020.
- [140] X. Qiu, Z. Xu, X. Peng, L. Li, Y. Zhou, M. Wei, M. Zhou, and X. Xu, “Three-axis atomic magnetometer for nuclear magnetic resonance gyroscopes,” *Applied Physics Letters*, vol. 116, p. 034001, Jan. 2020.
- [141] W. Xiao, Y. Wu, X. Zhang, Y. Feng, C. Sun, T. Wu, J. Chen, X. Peng, and H. Guo, “Single-beam three-axis optically pumped magnetometers with sub-100 femtotesla sensitivity,” *Applied Physics Express*, vol. 14, p. 066002, May 2021.

- [142] K. Namita, Y. Ito, and T. Kobayashi, “Vector measurement of pico tesla magnetic fields using an optically pumped magnetometer by varying pump beam direction,” *Japanese Journal of Applied Physics*, vol. 60, p. 076507, June 2021.
- [143] R. Zhang, R. Mhaskar, K. Smith, E. Balasubramaniam, and M. Prouty, “Vector measurements using all optical scalar atomic magnetometers,” *Journal of Applied Physics*, vol. 129, p. 044502, Jan. 2021.
- [144] F. Bertrand, T. Jager, A. Boness, W. Fourcault, G. Le Gal, A. Palacios-Laloy, J. Paulet, and J. M. Léger, “A 4He vector zero-field optically pumped magnetometer operated in the Earth-field,” *Review of Scientific Instruments*, vol. 92, p. 105005, Oct. 2021.
- [145] A. Grosz, M. J. Haji-Sheikh, and S. C. Mukhopadhyay, *High sensitivity magnetometers*. SPRINGER, 2018.
- [146] J. Allred, R. Lyman, T. Kornack, and M. V. Romalis, “High-sensitivity atomic magnetometer unaffected by spin-exchange relaxation,” *Physical review letters*, vol. 89, no. 13, p. 130801, 2002.
- [147] H. Dang, A. C. Maloof, and M. V. Romalis, “Ultrahigh sensitivity magnetic field and magnetization measurements with an atomic magnetometer,” *Applied Physics Letters*, vol. 97, no. 15, 2010.
- [148] D. Sheng, S. Li, N. Dural, and M. V. Romalis, “Subfemtotesla scalar atomic magnetometry using multipass cells,” *Physical review letters*, vol. 110, no. 16, p. 160802, 2013.
- [149] J. Li, W. Quan, B. Zhou, Z. Wang, J. Lu, Z. Hu, G. Liu, and J. Fang, “Serf atomic magnetometer—recent advances and applications: A review,” *IEEE Sensors Journal*, vol. 18, no. 20, pp. 8198–8207, 2018.
- [150] K. Sternickel and A. I. Braginski, “Biomagnetism using squids: status and perspectives,” *Superconductor science and technology*, vol. 19, no. 3, p. S160, 2006.

- [151] M. Rosner, D. Beck, P. Fierlinger, H. Filter, C. Klau, F. Kuchler, P. Rößner, M. Sturm, D. Wurm, and Z. Sun, “A highly drift-stable atomic magnetometer for fundamental physics experiments,” *Applied Physics Letters*, vol. 120, no. 16, 2022.
- [152] K. D. Rathod and V. Natarajan, “Magnetometry using Ramsey interferometry in a Yb atomic beam,” *CURRENT SCIENCE*, vol. 109, no. 3, p. 4, 2015.
- [153] B. Maddox, C. Deans, H. Yao, Y. Cohen, and F. Renzoni, “Rapid Electromagnetic Induction Imaging With an Optically Raster-Scanned Atomic Magnetometer,” *IEEE Transactions on Instrumentation and Measurement*, vol. 72, pp. 1–5, 2023.
- [154] S. Hong, M. S. Grinolds, L. M. Pham, D. Le Sage, L. Luan, R. L. Walsworth, and A. Yacoby, “Nanoscale magnetometry with nv centers in diamond,” *MRS bulletin*, vol. 38, no. 2, pp. 155–161, 2013.
- [155] E. B. Alexandrov and V. A. Bonch-Bruevich, “Optically pumped atomic magnetometers after three decades,” *Optical Engineering*, vol. 31, no. 4, pp. 711–717, 1992.
- [156] V. Yudin, A. Taichenachev, Y. Dudin, V. Velichansky, A. Zibrov, and S. Zibrov, “Vector magnetometry based on electromagnetically induced transparency in linearly polarized light,” *Physical Review A*, vol. 82, no. 3, p. 033807, 2010.
- [157] J. McKelvy, I. Novikova, E. E. Mikhailov, M. Gonzalez, I. Fan, Y. Li, Y.-J. Wang, J. Kitching, and A. Matsko, “Application of Kernel Principal Component Analysis for Optical Vector Atomic Magnetometry,” Apr. 2023. Preprint on webpage at https://www.techrxiv.org/articles/preprint/Application_of_Kernel_Principal_Component_Analysis_for_Optical_Vector_Atomic_Magnetometry/22357057.
- [158] C. Cohen-Tannoudji and S. Reynaud, “Dressed-atom description of resonance fluorescence and absorption spectra of a multi-level atom in an intense laser

- beam,” *Journal of Physics B: Atomic and Molecular Physics*, vol. 10, pp. 345–363, Feb. 1977.
- [159] C. N. Cohen-Tannoudji, “The Autler-Townes Effect Revisited,” in *Amazing Light: A Volume Dedicated To Charles Hard Townes On His 80th Birthday* (R. Y. Chiao, ed.), pp. 109–123, New York, NY: Springer, 1996.
- [160] J. Picque and J. Pinard, “Direct observation of the autler-townes effect in the optical range,” *Journal of Physics B: Atomic and Molecular Physics*, vol. 9, no. 5, p. L77, 1976.
- [161] B. Mollow, “Power spectrum of light scattered by two-level systems,” *Physical Review*, vol. 188, no. 5, 1969.
- [162] B. Suri, Z. Keane, R. Ruskov, L. S. Bishop, C. Tahan, S. Novikov, J. Robinson, F. Wellstood, and B. Palmer, “Observation of autler–townes effect in a dispersively dressed jaynes–cummings system,” *New Journal of Physics*, vol. 15, no. 12, p. 125007, 2013.
- [163] E. T. Jaynes and F. W. Cummings, “Comparison of quantum and semiclassical radiation theories with application to the beam maser,” *Proceedings of the IEEE*, vol. 51, no. 1, pp. 89–109, 1963.
- [164] T. Y. Abi-Salloum, “Electromagnetically induced transparency and Autler-Townes splitting: Two similar but distinct phenomena in two categories of three-level atomic systems,” *Physical Review A*, vol. 81, p. 053836, May 2010.
- [165] T. Abi-Salloum, “Interference between competing pathways in the interaction of three-level ladder atoms and radiation,” *Journal of Modern Optics*, vol. 57, pp. 1366–1376, Aug. 2010.
- [166] P. M. Anisimov, J. P. Dowling, and B. C. Sanders, “Objectively Discerning Autler-Townes Splitting from Electromagnetically Induced Transparency,” *Physical Review Letters*, vol. 107, p. 163604, Oct. 2011.

- [167] S. E. Harris, “Electromagnetically induced transparency,” *Physics today*, vol. 50, no. 7, pp. 36–42, 1997.
- [168] B. Peng, Ş. K. Özdemir, W. Chen, F. Nori, and L. Yang, “What is and what is not electromagnetically induced transparency in whispering-gallery microcavities,” *Nature Communications*, vol. 5, p. 5082, Oct. 2014.
- [169] P. Avan and C. Cohen-Tannoudji, “Hanle effect for monochromatic excitation. non perturbative calculation for a $j=0$ to $j=1$ transition,” *Journal de Physique Lettres*, vol. 36, no. 4, pp. 85–88, 1975.
- [170] W. Martin, R. Zalubas, and L. Hagan, “Atomic energy levels-the rare earth elements.(the spectra of lanthanum, cerium, praseodymium, neodymium, promethium, samarium, europium, gadolinium, terbium, dysprosium, holmium, erbium, thulium, ytterbium, and lutetium).[66 atoms and ions],” tech. rep., Manchester Coll. of Science and Technology (UK). Dept. of Chemistry, 1978.
- [171] S. Rochester, “Atomicdensitymatrix.” Mathematica package accessed at <https://rochesterscientific.com/ADM/>.
- [172] J. S. Jackson and D. S. Durfee, “Magneto-optical trap field characterization with the directional hanle effect,” *Scientific Reports*, vol. 9, no. 1, p. 8896, 2019.